Measurement of W and Z boson production cross sections in proton-proton collisions at $\sqrt{s} = 5.02\,\text{TeV}$ and $\sqrt{s} = 13\,\text{TeV}$

by

Stephanie Akemi Brandt

B.S., University of Illinois (2012)

Submitted to the Department of Physics
in partial fulfillment of the requirements for the degree of

Doctor of Philosophy

at the

MASSACHUSETTS INSTITUTE OF TECHNOLOGY

June 2020

Author .....
Department of Physics
May 1, 2020

Certified by .....
Philip Coleman Harris
Assistant Professor of Physics
Thesis Supervisor

Accepted by .....
Nergis Mavalvala
Associate Department Head of Physics

Measurement of W and Z boson production cross sections in proton-proton collisions at $\sqrt{s} = 5.02\,\text{TeV}$ and $\sqrt{s} = 13\,\text{TeV}$

by

Stephanie Akemi Brandt

Submitted to the Department of Physics
on May 1, 2020, in partial fulfillment of the
requirements for the degree of
Doctor of Philosophy

Abstract

Measurements of W and Z boson production cross sections in pp collisions at $\sqrt{s} = 5.02\,\text{TeV}$ and $\sqrt{s} = 13\,\text{TeV}$ are presented. Data was collected by the CMS experiment at the LHC during low-pileup data taking periods in 2017. The corresponding integrated luminosity for the data is $299.1 \pm 5\,\text{pb}^{-1}$ ($\sqrt{s} = 5.02\,\text{TeV}$) and $199.3 \pm 4\,\text{pb}^{-1}$ ($\sqrt{s} = 13\,\text{TeV}$), with an average number of pile-up interactions $\mu = 3$ ($\mu = 2$). Cross sections and cross section ratios are reported, with final states in electron and muon channels.

Thesis Supervisor: Philip Coleman Harris
Title: Assistant Professor of Physics

Acknowledgments

No man is an island, and the work undertaken for this thesis could not be possible without the support and guidance of others. Being mentored by someone with an strong interest in education and a deep knowledge of the field has been an invaluable aspect of my time as a graduate student, and the continuous guidance I have received from Aram Apyan throughout the entirety of my time at MIT has been the primary source of mentorship in this field. Furthermore, I would like to thank Phil Harris for recently taking on the role of being my thesis adviser—in two months I have received more supervision, been engaged in more physics discussion, and got more insight into the field than I had thought possible for an thesis adviser to provide.

Thanks to Andrew Ian Chen for his constant support and encouragement throughout my PhD. I would not be where I am without you.

My friends and fellow graduate students, whether we were located at MIT or at CERN, were a constant source of entertainment, camaraderie, and commiseration.

I would also like to thank Guillelmo Gomez-Ceballos and thesis committee members Bolek Wyslouch and Will Detmold for taking the time to read and provide feedback on this thesis.

Funding for the first three years of my graduate studies were partially provided by the National Science Foundation Graduate Research Fellowship Program under grant number 1122374.

Lastly, I would like to thank Markus Klute for, among many things, organizing great summer barbecues.

Contents

Chapter 1

Introduction

The diversity of physics programs at the Large Hadron Collider (LHC) has made the analysis in this thesis possible. Two consecutive datasets taken in late 2017—at $\sqrt{s} = 5.02\,\text{TeV}$ and $\sqrt{s} = 13\,\text{TeV}$ respectively—provides the opportunity to produce a set of measurements with high precision at two center-of-mass energies.

This chapter provides a general overview of the physics and motivations for this measurement, as well as a brief description of the analysis strategy and what types of results will be produced, and the following chapter provides a detailed physics background. Operations of the LHC and Compact Muon Solenoid (CMS) experiment are described. Subsequent chapters detail the data sets, event selection, important components, and signal fitting method. Finally, the results are summarized and a comparison with common models is provided.

1.1 A Brief Physics Background

Producing W and Z bosons in pp collisions

Protons are composite particles consisting of quarks and gluons. The composition of protons can be described by the valence quarks, sea quarks, and gluons. The valence quarks of p are two up quarks and one down quark (uud), which combine to make the color-neutral proton with $+1$ electric charge. The momentum distributions of the

constituent quarks and gluons are described by parton distribution function, which are determined from experimental data. At the high energies attained at the LHC, this internal structure within the protons being collided becomes extremely important to understanding the interactions occurring within the pp collisions. W and Z bosons are produced through the Drell–Yan process, with the predominant production interactions: $u\bar{u}, d\bar{d} \to Z$, $u\bar{d} \to W^+$, and $d\bar{u} \to W^-$. In pp collisions, these interactions therefore necessitate the participation of the sea quarks and predictions are sensitive to the sea quark PDFs.

Electroweak Measurements

Since the discovery of the W and Z bosons at UA1 and UA2 at CERN's Super Proton Synchrotron (SPS) [1–4], their properties have been studied extensively at both hadron colliders and e^+e^- colliders. The masses, branching fractions, decay widths, and cross sections have been measured by multiple experiments, and some of these are known to high precision [5]. Measurements of the Z boson decay width at the Large Electron-Position collider provide constraints on the number of neutrino flavors [6]. Past measurements of the W and Z boson cross sections at hadron colliders (Figure 1-1) have been performed in $p\bar{p}$ collisions at the UA1 & UA2 experiments at the SPS, DØ and CDF experiments at Fermilab's Tevatron, and in pp collisions by experiments at the LHC. Cross sections of $W^{\pm}$ and Z boson production at the LHC has been studied at $\sqrt{s} = 2.76$, 5.02, 7, 8, and 13 TeV by the CMS, ATLAS, and LHCb experiments [7–18].

This Measurement

This analysis will provide additional measurements with data collected by the CMS experiment at $\sqrt{s} = 5.02\,\text{TeV}$ and $\sqrt{s} = 13\,\text{TeV}$. Figure 1-1 summarizes prior measurements performed by the experiments at the UA1, UA2, DØ, CDF, and CMS experiments as well as indicating the center-of-mass energies for the measurements in this thesis. These measurements will contain the largest datasets utilized for inclusive W and Z boson cross sections at $\sqrt{s} = 5.02\,\text{TeV}$ and $\sqrt{s} = 13\,\text{TeV}$ to-date [7–9, 18].

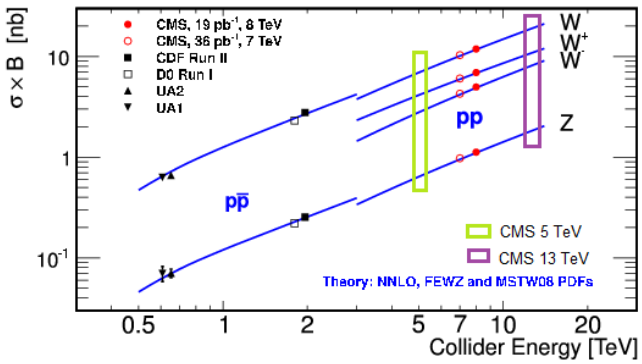

Figure 1-1: Summary of previous measurements of the W and Z boson production cross section at hadron colliders. Not shown are the results from $\sqrt{s} = 13\,\text{TeV}$ LHC measurements. Measurements presented in this thesis are also indicated. Adapted from [19].

1.2 Measuring the cross sections

W and Z decays

W and Z bosons can decay both hadronically and leptonically. Branching fractions of the W boson decay are $\sim$ 67% hadronic and $\sim$ 33% leptonic, and branching fractions of the Z boson are $\sim$ 70% hadronic and $\sim$ 10% leptonic with the remaining $\sim$ 20% being invisible decay channels [5]. Lepton universality implies the leptonic decays are expected to occur at equal rates for each of the lepton flavors, l = electrons (e), muons (μ), and tau leptons (τ). The W and Z boson leptonic decay channels are $Z \to \ell^+ + \ell^-$ and $W^{+(-)} \to \ell^{+(-)} + \overset{(-)}{\nu}_\ell$, with $\ell = e,\ \mu,\ \tau$. These will henceforth be written as $Z \to \ell\ell$ and $W \to \ell\nu$ (or with $\ell = e,\ \mu,\ \tau$), with charge and lepton number conservation laws implied. Leptonic decay channels are utilized because electrons and muons can be reconstructed and identified well by CMS. A fairly clean sample and accurately modeled observables are important components of this measurement. The leptonic decays $Z \to ee$ and $Z \to \mu\mu$ provide extremely clean signatures marked by the presence of a pair of oppositely charged same-flavor leptons. Similarly, the decay channels $W \to e\nu$ and $W \to \mu\nu$ can be identified by the presence of a high-momentum electron or muon.

Cross section

The cross section times branching ratio for a given channel is measured experimentally by determining the number of signal events observed and accounting for the acceptance of the measurement, as shown in Equation 1.1. The acceptance of the fiducial volume (the sensitive detector region used in the analysis) is determined from simulation, and the efficiency scale factor is determined by measuring selection efficiency in both simulation and data. The following chapters of this thesis describe the derivation of these quantities in detail.

$$\sigma \times Br = \frac{N_{sig}}{A\epsilon \int \mathcal{L}dt} \tag{1.1}$$

- N_{sig}: Number of signal events observed in a given channel
- A: The acceptance is the number of W or Z bosons producing a final state with leptons inside the fiducial measurement volume, divided by the total number of W or Z bosons produced. Determined from simulation.
- ϵ: The efficiency scale factor, to account for the differences in rates of lepton identification and selection between simulation and data
- $\int \mathcal{L}dt$: integrated luminosity. The integrated luminosity provides the number of pp collisions measured in a given dataset.

Z boson cross section

Measuring the cross section of the Z boson is fairly straightforward, as the dilepton decay of a Z boson is an extremely clean signature with minimal background. Two well-identified leptons, required to be of the same flavor be oppositely charged, within the invariant mass range $60\,\text{GeV} \leq \text{M}_{ll} \leq 120\,\text{GeV}$ are taken to be candidates for $Z \to \ell\ell$ decays. Small background contributions primarily from diboson and $t\bar{t}$ events are simulated, and the total contribution of the background processes is subtracted from the observed Z boson yield.

W boson cross section

The W boson decay channels used in this measurement include the production of a neutrino, which is not measured by CMS. Therefore, the final state cannot be fully reconstructed, and additionally has a fairly large background. Instead of a fully reconstructed final state, an observable, transverse missing energy, E_{T}^{miss}, is used to infer the momentum of the neutrino. Transverse mass, m_{T}, is constructed from the lepton momentum and E_{T}^{miss} as a proxy for the neutrino. The simulated m_{T} distribution for the $W \to \ell\nu$ signal process, as well as several background processes, are used in a fit to data to determine the cross section. Measuring the W boson production cross section relies on the Z boson—there are multiple corrections that need to be derived for the W boson simulations that cannot be done without the Z boson. In addition to the lepton efficiency and momentum corrections, the fit to m_{T} requires an accurate modeling of E_{T}^{miss} and therefore the hadronic recoil in an event. Hadronic recoil corrections account for differences between simulation and data, and are derived in a data-driven approach which relies on the Z boson, and are described in Chapter 9.

Measurements

The results presented in this thesis are derived from datasets at $\sqrt{s} = 5.02$ TeV and $\sqrt{s} = 13$ TeV. This provides the opportunity to produce results with high precision for two center-of-mass energies. The measurements are presented as the cross sections for W^+, W^-, W, Z, as well as the ratios of the cross sections W^+/W^-, W^+/Z, W^-/Z, W/Z. Evaluating the ratios allows for the subtraction of any correlated systematic uncertainties, and increases the precision of the measurement. Notably, the uncertainty from the luminosity calibration is one of the largest uncertainties, and it completely cancels for these ratios.

1.3 Impact of the Measurement

W and Z boson production is an important measurement at any hadron collider. The precision measurement of the W and Z boson production provides a precision test of the Standard Model (SM), as well as a benchmark for the state-of-the-art calculations and models that are used to describe the proton and simulate physical interactions at the LHC and other experiments. The inclusive cross section measurements are the foundation of differential cross section measurements which provide greater constraints on different aspects of the models. W and Z boson production is also significant background to many other electroweak measurements and searches for new physics.

Additionally, W and Z bosons are a significant source of isolated, high-p_{T} leptons. The clean signature of $Z \to \ell\ell$ is used for detector calibration and luminosity monitoring [20].

Chapter 2

Physics Background

The Standard Model of particle physics is a $SU(3) \otimes SU(2) \otimes U(1)$ gauge theory that describes the interactions of fundamental particles. It is generally described in two parts, electroweak theory and quantum chromodynamics, presented in the following section. In later sections, the production of W and Z bosons in pp collisions and the modeling of these processes is described.

2.1 The Standard Model

Introduction

The SM has been a remarkably successful theory describing fundamental particles and their interactions. The fundamental constituents of matter—leptons and quarks—interact through the strong and electroweak interactions. Depicted in Figure 2-1, the SM consists of three families of quarks (purple), three families of leptons (green), the force carriers (red), and the Higgs boson (yellow).

Familiar building blocks of matter—protons and neutrons—are not the most basic particles, they are composed of constituent quarks and gluons. There are three families of quarks, with six total flavors. Up-type quarks up (u), charm (c), and top (t) have electric charge $+\frac{2}{3}e$, and down-type quarks down (d), strange (s), and bottom (b) have electric charge $-\frac{1}{3}e$. Protons are uud, with an electric charge of $+1e$. The

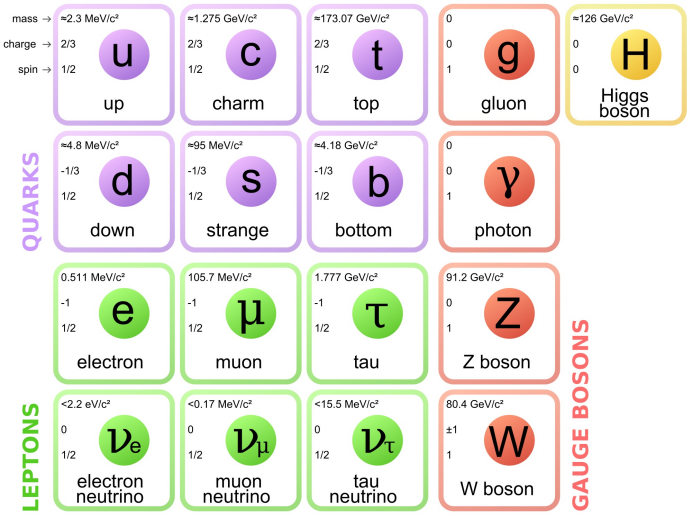

Figure 2-1: Fundamental particles of the Standard Model [21].

strong interaction, mediated by the gluon, binds quarks together into hadrons. The strength of the strong coupling is scale-dependent, with coupling strength decreasing with shorter distance (higher energy) scales. Therefore, bare quarks have never been observed, as it is favored for them to quickly ($\mathcal{O}(10^{-24})$ seconds) form bound states. The lepton families are the electron and its more massive analogs, the muon and tau leptons, along with their corresponding neutrinos.

The weak interaction is propagated by the W and Z bosons. Both the charged leptons, neutrinos, and quarks can couple to W and Z bosons. At low energies, the weak interaction is commonly know for its role in beta decay, with uses such as radioluminescent tritium illumination sources and medical imaging positron emission tomography (PET scan). At energies achieved by the LHC, the W and Z bosons can be produced in pp collisions and the properties of the production can be studied. As described in below, this provides important information on several fronts, including event modeling and detector performance.

2.1.1 Electroweak Theory

In the SM [22–24], electroweak interactions belong to the gauge group $SU(2) \otimes U(1)$, with the gauge bosons W^i_μ $(i = 1, 2, 3)$ for $SU(2)$ and B_μ for $U(1)$. The left-handed fermions transform as $SU(2)$ doublets, where the leptons are given in Equation 2.1

and quarks are shown in Equation 2.2. The q_i' (d', s', b') are given by $q_i' = \sum_j V_{ij} q_i$, where q_i are $d,\ s,\ b$ and V_{ij} are the elements of the Cabibbo-Kobayashi-Maskawa (CKM) matrix [25, 26] which describes the mixing between the quark generations.

$$\Psi = \begin{pmatrix} v_e \\ l_e \end{pmatrix},\ \begin{pmatrix} v_\mu \\ l_\mu \end{pmatrix},\ \begin{pmatrix} v_\tau \\ l_\tau \end{pmatrix} \tag{2.1}$$

$$\Psi = \begin{pmatrix} u \\ d' \end{pmatrix},\ \begin{pmatrix} c \\ s' \end{pmatrix},\ \begin{pmatrix} t \\ b' \end{pmatrix} \tag{2.2}$$

Vector fields corresponding to particles with spin 1 and mass are the $W_\mu^\pm$, Z_μ, and photon A_μ, which are given in terms of the gauge fields as:

$$\begin{aligned} A_\mu &= B_\mu cos\theta + W_\mu^3 sin\theta \\ Z_\mu &= -B_\mu sin\theta + W_\mu^3 sin\theta \\ W_\mu^\pm &= W_\mu^1 \mp i W_\mu^2 \end{aligned} \tag{2.3}$$

Mass generation is achieved through spontaneous symmetry breaking of $SU(2) \otimes U(1)$ to $U(1)_{em}$ with the addition of a complex scalar doublet $\phi = \frac{1}{\sqrt{2}} \begin{pmatrix} \sqrt{2}\phi^+ \\ \phi^0 + i a^0 \end{pmatrix}$, known as the Brout-Englert-Higgs mechanism [27–29]. The potential is given by $V(\phi) = \mu^2 \phi^\dagger \phi + \lambda^2 (\phi^\dagger \phi)^2$, with the full Lagrangian being given in Equation 2.4. With $\mu^2 < 0$, the vacuum expectation value of ϕ is $< \phi >= v/\sqrt{2} = \mu/\lambda$ with $v \approx 246$ GeV.

$$\mathcal{L}_{Higgs} = (D_\mu \Phi)^\dagger (D^\mu \Phi) - \mu^2 \Phi^\dagger \Phi - \lambda (\Phi^\dagger \Phi)^2 \tag{2.4}$$

The covariant derivatives of Equation 2.4, $D_\mu \Phi$, provide the couplings between the Higgs fields and the W_μ and B_μ gauge fields, shown in Equation 2.5

$$D_\mu \Phi = (\partial_\mu + i g \sigma^a W_\mu^a / 2 + i g' Y B_\mu / 2) \Phi \tag{2.5}$$

Three of the four degrees of freedom introduced by the Higgs doublet are absorbed into the W_μ^i and B_μ fields of the $SU(2) \otimes U(1)$ and become the longitudinal components of the W and Z bosons. The physical W and Z bosons also acquire mass. The generator of the unbroken $U(1)_{em}$ gauge symmetry, the photon, remains massless.

The remaining degree of freedom manifests as the new neutral scalar particle, the Higgs boson. The masses of the physical bosons are given in Equation 2.6.

$$\begin{aligned} m_H &= \lambda v \\ m_W &= \frac{1}{2} g v = cos\theta_W m_Z \\ m_z &= \frac{1}{2}\sqrt{g^2 + g'^2} v = \frac{M_W}{\cos\theta_W} \\ m_\gamma &= 0 \end{aligned} \tag{2.6}$$

Fermion masses are likewise given through a Yukawa coupling to the Higgs field, shown in Equation 2.7. Fermion masses become $m_{f_i} = h_{f_i} v/\sqrt{2}$ after rotation into a basis where the Higgs-fermion interaction is diagonalized. The fermion coupling to the Higgs boson is $\frac{m_f}{v} \bar{f} f H$, proportional to its mass.

$$\mathcal{L}_{yukawa} = -\hat{h}_{d_{i,j}} \bar{q}_{L_i} \Phi d_{R_j} - \hat{h}_{u_{i,j}} \bar{q}_{L_i} \bar{\Phi} u_{R_j} - \hat{h}_{l_{i,j}} \bar{l}_{L_i} \Phi e_{R_j} + h.c. \tag{2.7}$$

In Equation 2.7, q_L and u_R, d_R are the quark doubles and singlets, and l_L and e_R are the lepton doublets and singlets. As the Higgs boson is electromagnetically neutral and also transforms as a singlet in $SU(3)$, there are no tree-level couplings of the Higgs to either photons or gluons.

2.1.2 Quantum Chromodynamics

The strong interaction between quarks and gluons is described by quantum chromodynamics (QCD), the $SU(3)$ part of the SM. Interactions between quarks and gluons is described by the Dirac Lagrangian density given in Equation 2.8. Quarks and gluons carry color charges (red, green, or blue: $N_C = 3$), and there are eight color-combinations of gluons as mediators of the strong force (gluon fields represented by: A^C_μ,with $C = [1...8]$). Quarks are represented by the $\bar{\psi}_{f,\alpha}$ spinors, with the six flavors of quarks (u, c, t, d, s, b) represented by f, the three colors by α, and the quark masses by m_f. The γ^μ are Dirac matrices.

$$\mathcal{L} = \bar{\psi}_{f,\alpha}(i\gamma^{\mu}\partial_{\mu}\delta_{\alpha\beta} - g_s\gamma^{\mu}t^C_{\alpha\beta}\mathcal{A}^C_{\mu} - m_f\delta_{\alpha\beta})\gamma_{f,\beta} - \frac{1}{4}F^b_{\mu\nu}F^{b,\mu\nu} \tag{2.8}$$

The eight generators of the $SU(3)$ color group are 3×3 matrices $t^C_{\alpha\beta}$. The strong coupling constant is g_s ($\sqrt{4\pi\alpha_s}$), where α_s varies with energy scale. The gluon field tensors $F_{\mu\nu}$ are shown in Equation 2.9, where the f_{ABC} are the structure constants of $SU(3)$.

$$F^A_{\mu\nu} = \delta_{\mu}\mathcal{A}^A_{\nu} - \delta_{\nu}\mathcal{A}^A_{\mu} - g_s f_{ABC}\mathcal{A}^B_{\mu}\mathcal{A}^C_{\nu}, \quad [t^A, t^B] = if_{ABC}t^C \tag{2.9}$$

There is an additional term in the QCD Lagrangian which contains a parameter θ, and allows for CP violation in QCD. Experimental limits on the neutron electric dipole moment constrain this term to be $\theta < 10^{-10}$ [30].

Computational methods for QCD predictions include lattice gauge theory and perturbative expansion methods. Feynman rules for QCD allow diagrams with $q\bar{q}g$ and ggg vertices and a $gggg$ vertex [31]. Perturbative QCD (pQCD) expresses predictions for observables as an expansion in terms of the coupling $\alpha_s(\mu_R^2)$ i.e. $f = f_0 + f_1\alpha_s + f_2\alpha_s^2 + f_3\alpha_s^3 + ...$ The coupling $\alpha_s(\mu_R^2)$ is a function of the renormalization scale μ_R, and the effective strength of the interaction with momentum transfer Q^2 is $\alpha_s(\mu_R^2 \sim Q^2)$. Calculations are done with Feynman diagrams and are generally performed to only a few terms—leading order (LO, first term), next-to-leading order (NLO, first two terms), and so forth. The scale dependence of QCD is expressed in the renormalization group equation:

$$\mu_R^2\frac{d\alpha_s}{d\mu_R^2} = \beta(\alpha_s) = -(b_0\alpha_s^2 + b_1\alpha_s^3 + b_2\alpha_s^4 + \cdots) \tag{2.10}$$

The minus sign indicates that the coupling becomes weak for interactions with high momentum transfer and is strongly interacting for low energy scales, the source of asymptotic freedom [32,33]. Values of α_s range from $\alpha_s \sim 0.1$ for Q in the $100\,\text{GeV} -$ TeV range to over $\alpha_s \sim 0.3$ for processes with momentum transfer $Q \sim 1\,\text{GeV}$, as depicted in Figure 2-2. Free quarks have not been observed—they quickly hadronize into mesons or baryons on the time scale $\sim 1/\Lambda_{QCD}$, while the top quark decays before

hadronization. This is understood as a result of the strong coupling increasing at low energies (large distance scales), and only the color-singlet hadrons are observed.

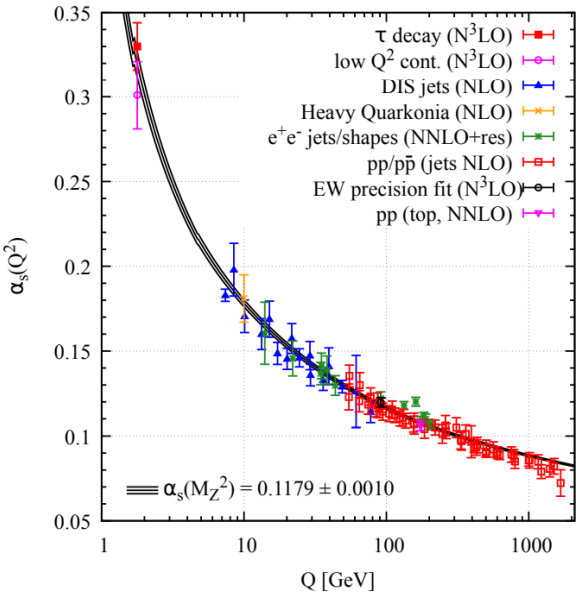

Figure 2-2: Measurements of α_s demonstrating the scale-dependence [5].

2.2 Modeling *pp* collisions

Theoretical predictions of *pp* collisions are an important tool for understanding physical processes and modeling observables studied at the LHC. These predictions are based on an underlying proton model and calculations are performed from approximations at different energy scales. Precision measurements such as the one in this thesis provide important information to further refine these models and calculations. This chapter describes the general methods for modeling proton-proton collisions as well as details about W and Z boson production at the LHC.

2.2.1 Simulating *pp* interactions

In collisions at very low energies, protons can be approximated as electrically charged objects. At higher energies, such as those at the LHC, the structure within protons begins to have an important role for the scattering process. W and Z bosons are

produced from the interaction of quarks and gluons (both also referred to as partons) within the proton [34,35]. The contributions of the partons to the proton's structure are described by parton distribution functions (PDFs). The PDFs, $f_i(x, Q^2)$, give the probability of finding a parton of carrying a fraction x of the proton's longitudinal momentum. Current PDFs are determined by global fits to experimental data sets [36] (recent advances in lattice QCD may). Valence quarks, sea quarks, and gluons within the proton are described by the PDFs.

For hard scattering processes such as W and Z boson production, the momentum transfer, Q is high. Due to the asymptotic freedom of QCD, the coupling constant $\alpha_S(Q^2)$ is small, and perturbative calculations are effective. The highest order calculation currently available for the W and Z production is next-to-next-to-leading order (NNLO) [37].

In the perturbative expansions, initial-state radiation of soft and collinear gluons produces logarithmic terms which cause singularities and divergences in the calculations. To accommodate this effect, the calculation can be split into perturbative and non-perturbative regimes. This is described by the factorization theorem, which ensures that the hard process is independent of the intial-state radiation, and separates the QCD calculations at a factorization scale, μ_F. This allows the singularities due to the soft gluon emissions to be factored out and contained within the PDFs [38]. The PDF dependence on the factorization scale is determined by the Dokshitzer–Gribov–Lipatov–Altarelli–Parisi (DGLAP) equations. The DGLAP equations introduce a μ_F dependence to the scale-independent PDFs by including initial-state soft radiation, and provide an evolution of the PDFs over different factorization scales [39,40]. Equation 2.11 shows the factorized cross section calculation. The first section includes the PDFs, f_a and f_b, evaluated at the factorization scale μ_F, for partons a and b, each carrying fractions x_a and x_b of the proton momentum. The second half describes the hard scattering between the two partons, where the cross section, $\hat{\sigma}$, is expanded

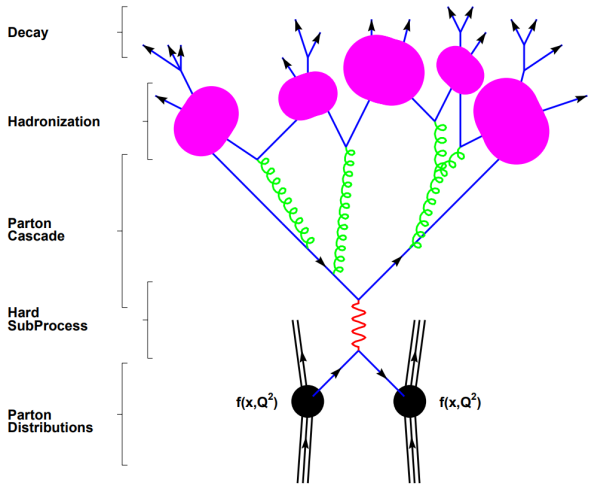

Figure 2-3: Illustration of a hard-scatter process. Time progresses from bottom to top, starting with individual parton interaction and hard scatter, progressing through parton shower, hadronization, and decays of individual hadrons. [41]

perturbatively.

$$\sigma_{p_a p_b \to n} = \sum_{a,b} \int dx_a dx_b f_a(x_a, \mu_F^2) f_b(x_b, \mu_F^2) \times [\hat{\sigma}_{LO}(x_a x_b s, \mu_R^2, \mu_F^2) + \alpha_S \hat{\sigma}_{NLO}(x_a x_b s, \mu_R^2, \mu_F^2) + \cdots] \tag{2.11}$$

Matrix element calculation breaks down for soft and collinear final states. Instead, parton shower models are used to produce the final-states at non-perturbative scales. Showering is modeled as series of radiative steps, with partons branching into consecutively lower energy state: $q \to gq$, $g \to gg$, and $g \to q\bar{q}$ for QCD. Branching probability at a scale Q^2 is determined by evolving the splitting functions using the DGLAP equations. Additionally, QED interactions ($q \to q\gamma$ and $l \to l\gamma$) are included in the shower modeling. Parton showering continues to the scale $\Lambda \sim 200$ MeV, where bare partons are hadronized into color-neutral hadrons. Then the unstable hadrons are decayed according to branching ratios. Factorization and a hard scatter process, along with subsequent parton showering and hadronization is illustrated in Figure 2-3.

2.2.2 W and Z production at the LHC

In the pp collisions, the bosons are produced through the interaction of quarks and gluons within the protons. The primary production modes for the W and Z bosons is through the Drell-Yann process, predominantly $u\bar{u}, d\bar{d} \to Z$, $u\bar{d} \to W^+$, and $d\bar{u} \to W^-$. In proton-proton collisions, these processes require the participation of at least one sea quark [42].

The kinematic variables describing the partons participating in the interaction are listed in Equations 2.12. The mass of the boson is represented by M, the rapidity of the boson is represented by y, and $\sqrt{s}$ is the center-of-mass energy of the collision. The relative fraction of the proton's longitudinal momentum held by each of the initial partons is represented by x_1 and x_2.

$$\begin{aligned} M &= \sqrt{x_1 x_2 s} \\ y &= \frac{1}{2}\ln\left(\frac{E+p_z}{E-p_z}\right) = \frac{1}{2}\ln\left(\frac{x_1}{x_2}\right) \\ x_1 &= \frac{M}{\sqrt{s}}e^{y},\ x_2 = \frac{M}{\sqrt{s}}e^{-y} \end{aligned} \tag{2.12}$$

W and Z boson production occupies a phase space near $Q \sim 100\,\text{GeV}$ (approximately the W or Z boson mass). Given a measurement acceptance of $|y| < 2.4$, this allows us to study x approximately within the range $10^{-4} < x < 0.1$ at the LHC.

When simulating the proton-proton interactions, the PDFs describing the relative fraction x of the proton's momentum contained by the individual partons is important. As previously described, the PDFs are dependent on the energy scale of the interaction, and in the case of the W and Z boson production this scale is around the mass of the bosons $Q \sim 100\,\text{GeV}$. There are many collaborations dedicated to providing PDF sets for use in these predictions, with many of the PDFs constructed from global fits to experimental data. Each collaboration uses a different approach and often different sets of experimental data in the fits, resulting in different PDF predictions and uncertainties. An example illustrating the PDFs involved in W and Z boson production is given in Figure 2-5 [43–47]. An illustration of the involve-

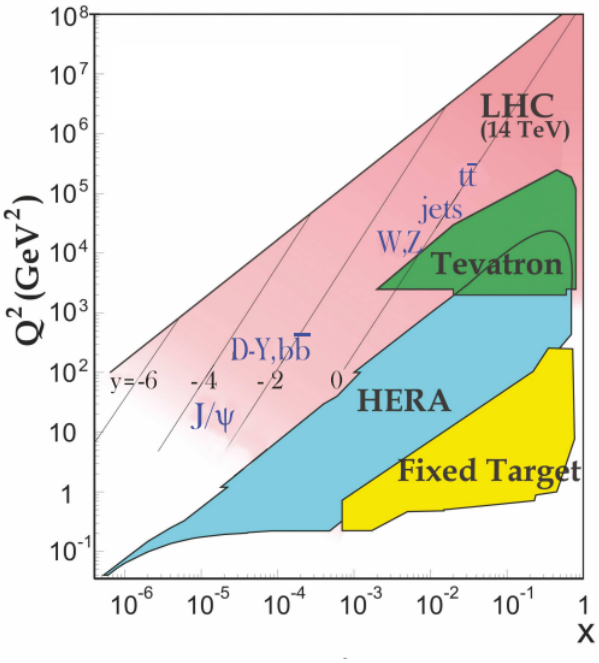

Figure 2-4: Phase space of Bjorken-x and Q^2 available at the LHC and other experiments. Proton-proton collisions at the LHC can probe very high Q^2. With an acceptance of $|y| < 2.4$, W and Z boson cross section measurements can probe approximately $10^-4 < x < 0.1$ [5]

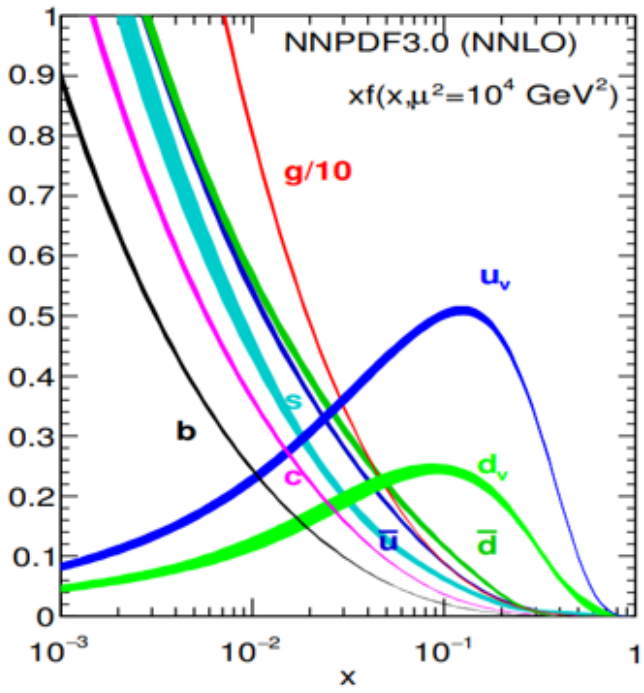

Figure 2-5: An example of a PDF illustrating the relative contribution of partons to the proton's longitudinal momentum at $Q \sim 100\,\text{GeV}$, provided by the NNPDF collaboration [43]. The valence quarks u and d are shown in bright blue and green, while the other quark flavors are sea quarks.

ment of the various quark flavors in the production of W and Z bosons at a range of rapidities is shown in Figure 2-6. Measurement of W production in proton-proton collisions allows for separation of quark flavors, and ratios of W and Z cross sections can provide constraint to the strange content of the proton.

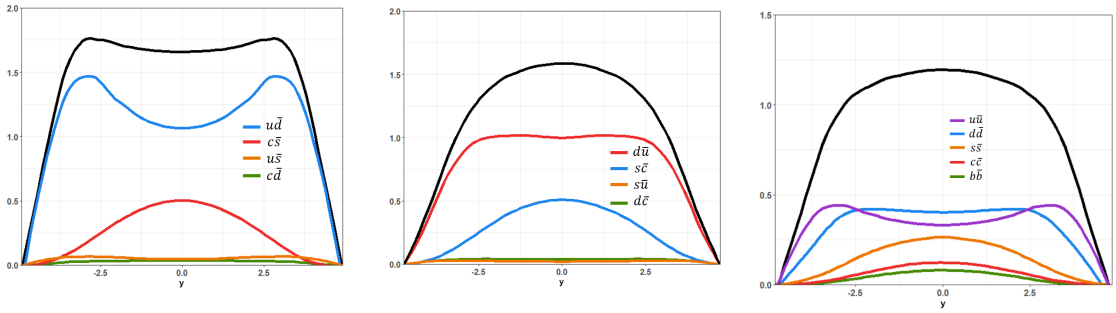

Figure 2-6: Contribution of different quark flavors to the W^+, W^-, and Z boson production over a range of boson rapidities. W^+ (W^-) boson production is predominantly $u\bar{d}$ ($\bar{u}d$), while Z boson production includes larger contributions from heavier flavors. Adapted from [48].

Chapter 3

The CMS Experiment at the LHC

This measurement was performed using data collected by the CMS Experiment, one of the multipurpose detector experiments at the LHC. This chapter details the technical design and operation of the LHC and CMS.

3.1 The Large Hadron Collider

The Large Hadron Collider is an 26.7 km-circumference accelerator designed to circulate protons or heavy nuclei in opposing directions to facilitate the study of fundamental physical interactions. It is housed in an underground tunnel, crossing the French-Swiss border, at a depth between 40m to 170m. This tunnel was previously home to the electron-positron collider, LEP. The LHC and accelerator complex at CERN are shown in Figure 3-1.

LHC Pre-Accelerators

Protons are produced by ionizing hydrogen gas, which are accelerated to 50 MeV by LINAC2, and injected into the Proton Synchroton Booster. The PSB then brings the protons to 1.6 GeV for injection into the Proton Synchrotron (PS). The PS takes six proton bunches, splits each into three prior to acceleration to 25 GeV, then subsequently splits each bunch into four prior to injection into the Super Proton Synchroton (SPS), resulting in 72 bunches injected into the SPS. The SPS can receive

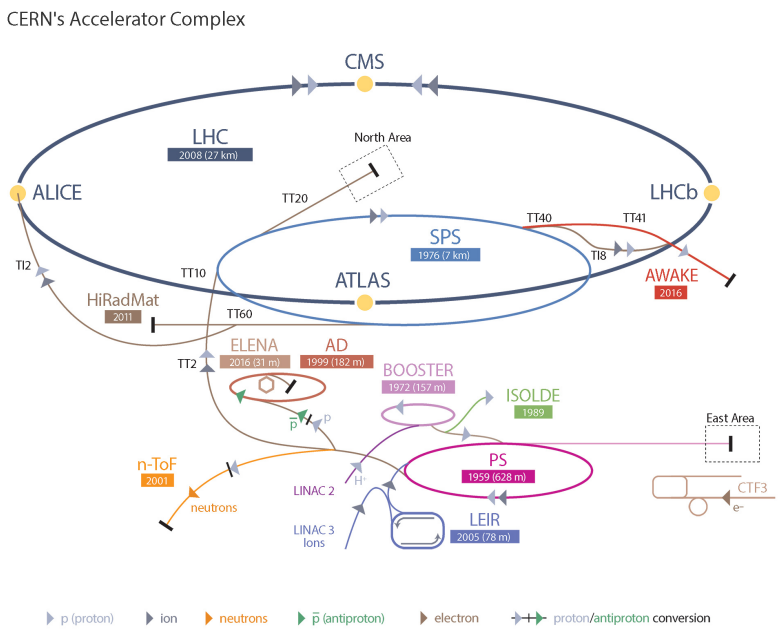

Figure 3-1: Illustration of the full accelerator complex at CERN, including the pre-accelerators, the LHC, and the major collision halls at the LHC. [49]

up to 4 sets of 72 bunches from the PS, accelerating them to 450 GeV per proton for injection into the LHC where they are further accelerated to a maximum of 6.5 TeV per proton. Bunches from SPS can be injected into the LHC up to 24 times, for a minimum spacing of 25 ns between bunch crossings [50].

The Large Hadron Collider

After injection into the LHC, protons are accelerated by radio-frequency (RF) cavities to an energy of 6.5 TeV. The trajectory of the protons around the ring is controlled by 1232 niobium-titanium wire superconducting dipole magnets, 15m in length, which are cooled by liquid Helium to a temperature of 1.9 K and have a magnetic field strength of 8.33 T. These dipole magnets are responsible for bending the proton beams in the appropriate direction around the LHC. Superconducting quadrupole magnets, 5-7 m in length, are used to focus the proton bunches. The focusing quadrupoles are located near the collision points, to produce a more focused beam in preparation for collisions. Higher-order multipole magnets are also used for beam focusing and control. The beams circulated in the LHC are proton-proton, so the same beampipe

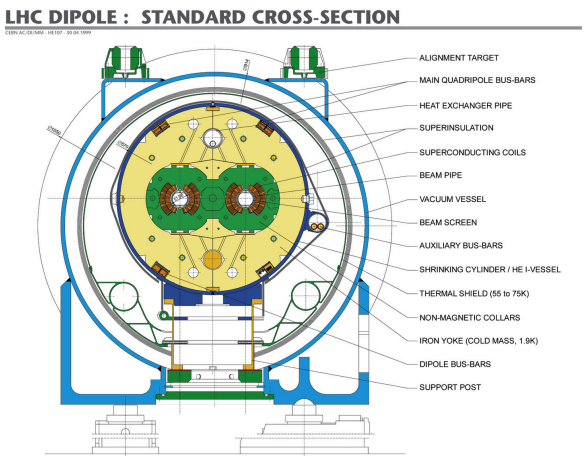

Figure 3-2: Cross-section of an LHC dipole magnet, showing the twin-bore design to accomodate the beampipes. [52]

cannot be used for both beams. Therefore a twin-bore magnet design is employed, where both beampipes are situated on the interior of the same magnet. A cross section of an LHC dipole is shown in Figure 3-2 [51].

Collisions occur where the beams intersect each other, located at multiple points around the LHC: Point 1 (ATLAS), Point 2 (ALICE), Point 5 (CMS), and Point 8 (LHCb).

3.2 The Compact Muon Solenoid

Data used in this thesis were collected by the CMS experiment. CMS is situated at LHC collision Point 5 near Cessy, France, and is depicted in Figure 3-3. CMS was designed for highly performant reconstruction of muons over a wide momentum range, high resolution tracking of charged particles, high energy resolution for electromagnetic processes, and high jet and E_{T}^{miss} resolution [53, 54]. This is achieved by the four primary sub-detector systems—from innermost to outermost—the silicon tracking system, electromagnetic calorimeter, hadronic calorimeter, and the muon system. A detailed cross sectional view of the detector and constituent subsystems is presented in Figure 3-4.

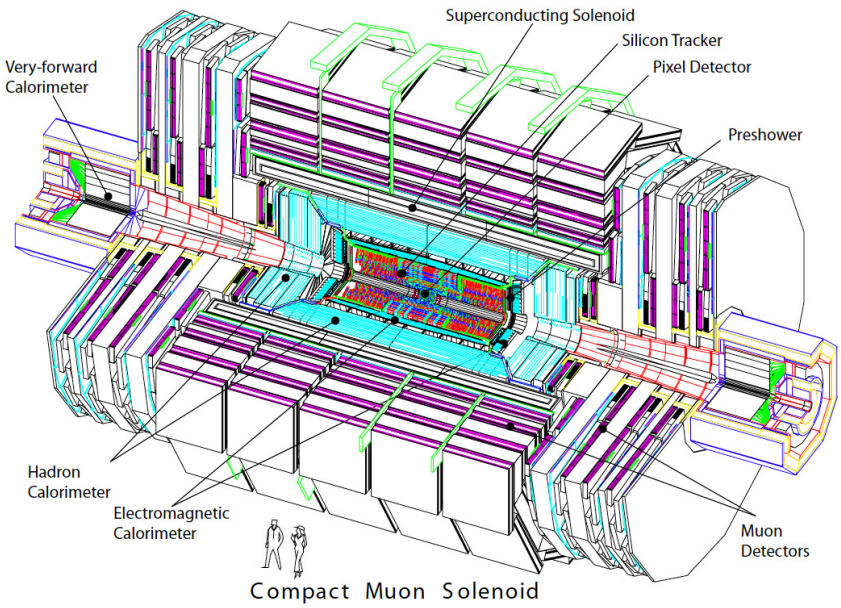

Figure 3-3: A 3-d cut-away view of the CMS detector, showing the relative position and size of the subdetectors as well as the orientation of the experiment with repsect to the beamline.

3.2.1 Magnet

The namesake superconducting magnet provides a uniform $|\vec{B}| = 3.8\,\mathrm{T}$ field at inner radii and a field of $|\vec{B}| = 2\,\mathrm{T}$ at radii outside of the magnet. This is achieved using a liquid helium-cooled niobium-titanium superconductor mechanically supported by a high-purity aluminum chassis. The operational temperature of the magnet is $T = 4.6\,\mathrm{K}$, which maintains the current and temperature below the critical values so that $|\vec{B}| = 3.8\,\mathrm{T}$ field [55].

With an inner radius of 6 meters, the solenoid bore houses the silicon tracker, electromagnetic calorimeter, and the hadronic calorimeter. The solenoid ensures a uniform inner magnetic field of $|\vec{B}| = 3.8\,\mathrm{T}$ along the z-axis for these sub-systems. On the outer radius of the solenoid, muon chambers are interspersed with the steel return yoke. The role of the return yoke is two-fold—extend uniformity and strength of the magnetic field outside of the solenoid and to act as an absorber layer for the muon chambers.

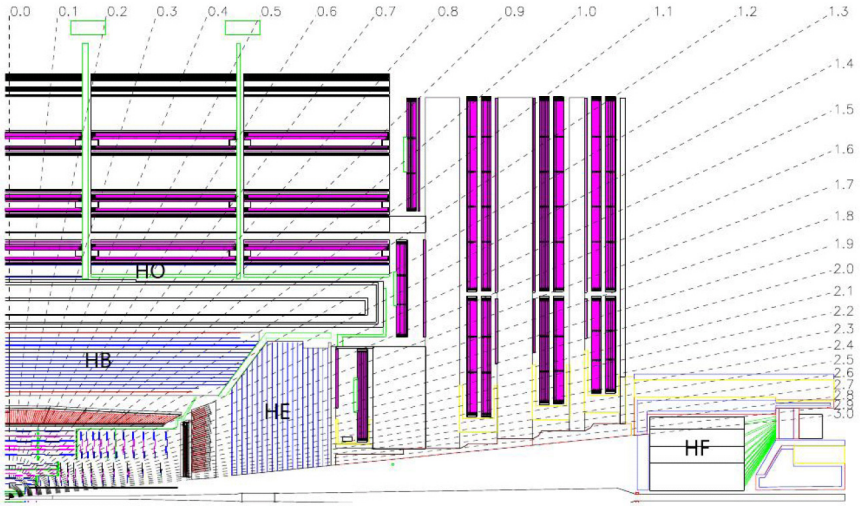

Figure 3-4: Quarter-view schematic of the CMS detector showing the arrangement of the subsystems. Radially arranged dotted lines indicate the pseudorapidity (η) coverage.

3.2.2 Trackers

The innermost detector system is the silicon tracker. The tracker measures the trajectory of charged particles from the collision point, and is designed to provide efficient and high-precision position reconstruction of charged particle trajectories through the tracker volume. In addition to providing high-resolution momentum information, the tracker should be able to identify isolated electromagnetic clusters, as in the $W \to e\nu$ and $Z \to ee$ channels, and to separate them from non-isolated electrons [57].

Other design considerations are the proximity of the inner tracker to the collision point and the material budget. Due to its close proximity to the beamline, the tracker is subjected to a high particle flux, with thousands of particles per bunch crossing every 25 ns. This necessitates a radiation-hard detector with fast readout and high granularity to reduce multiple-occupancy per channel. However, the amount of material in the detector—including the supporting electronics, cabling, and cooling systems—increases the amount of bremsstrahlung, which degrades the resolution of isolated electron measurements. Therefore the amount of detector material also needs to be minimized.

Given these design and operational considerations, the tracker uses silicon tech-

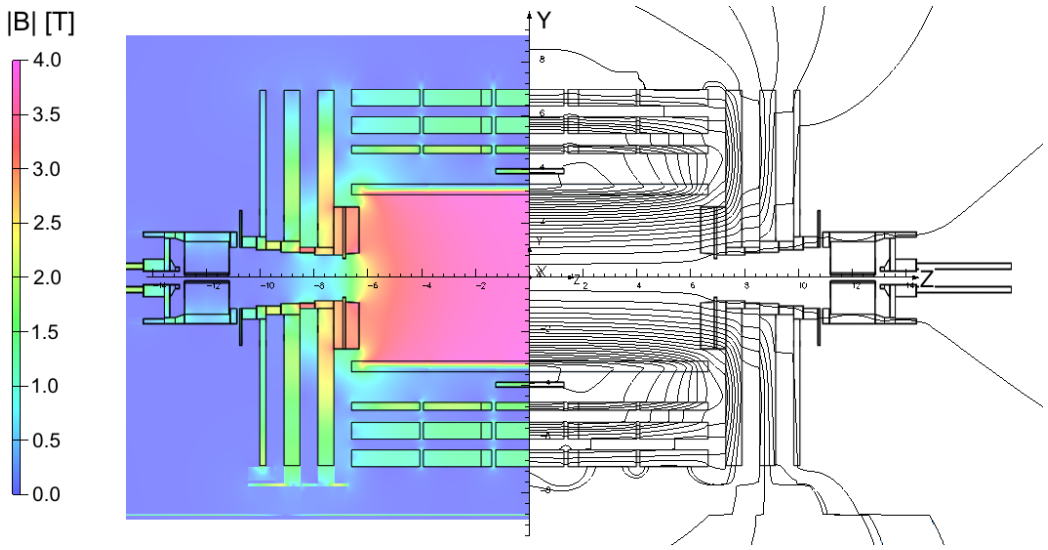

Figure 3-5: Diagram depicting the magnetic field strength and field lines from the CMS superconducting solenoid [56].

nology in the form of pixel and strip detectors. The silicon pixels are a p-n junction operated under a reverse-bias voltage. Charged particles traversing the depletion zone create electron-hole pairs, which drift under the reverse-bias and are collected by readout electronics.

The inner tracking system is composed of a silicon pixel detector, with 3 layers of pixels in the barrel ($r = 4.4\,\text{cm}$, $7.3\,\text{cm}$, and $10.2\,\text{cm}$, length $= 53\,\text{cm}$) and 2 layers of pixels in the end-cap region (inner radius of 6 cm, outer radius 15 cm, located at $|z| = 34.5\,\text{cm}$ and $|z| = 46.5\,\text{cm}$). The individual pixels are 150×100 μm, with 60 million pixels, where the fine segmentation is intended to minimize track occupancy per channel. A schematic depicting the geometry of the inner and outer tracking systems is shown in Figure 3-6.

Surrounding the inner tracker, the outer tracker is a series of silicon strip detectors. The tracker inner barrel (TIB) covers $20\,\text{cm} < r < 55\,\text{cm}$, and an additional six-layer outer barrel (TOB) extending to $r < 116\,\text{cm}$. The TIB spans $\pm$ 80 cm and TOB spans $\pm$ 118 cm in z. Tracker disk segments with strips arranged in rings are located within the inner radius of the TOB at z position just outside of the TIB. Depending on the position, each layer contains between 2 and 7 rings of detector with inner radius $21.8\,\text{cm}$- $39\,\text{cm}$ and outer radius $60.8\,\text{cm}$. An endcap (TEC) silicon strip tracking

detector is constructed from two sets of 9 disks, with the strips arranged in rings on each disk. The pitch of the strips ranges from 80 μm at the most forward regions to 205 μm in more central regions. TEC spans $z = \pm 95.2$ cm and $\pm$ 264 cm and provides coverage up to $|\eta| < 2.5$.

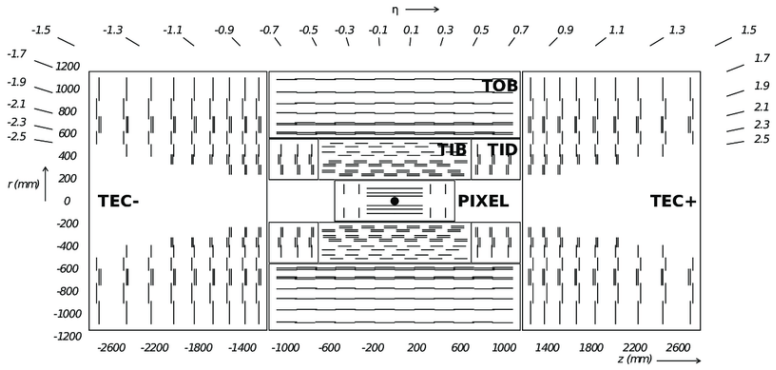

Figure 3-6: Schematic of the CMS tracking system. The silicon pixel detector is surrounded by the inner (TIB) and outer (TOB) barrel strip detectors. The endcap (TEC) strip detectors provide forward coverage up to $|\eta|<2.5$. [58]

3.2.3 Electromagnetic Calorimetry

The energy carried by electrons and photons is measured by the electromagnetic calorimeter (ECAL). The ECAL is a homogenous and hermetic calorimeter situated just outside of the silicon tracker, which measures the energy carried by electrons and photons. Driving factors determining the design of the ECAL is the need for a fast response time sufficient for collisions occuring every 25 ns as well as a high-resolution measurement necessary for the $H \to \gamma\gamma$ measurement. To this end, the active material is a scintillating lead tungstate ($PbWO_4$) crystal. Incident electrons and photons create an electromagnetic shower within the crystal. As the shower propagates, scintillation light is produced by excitations in the crystal lattice caused by the particles in the shower. The scintillation light, proportional to the energy deposited by the incident particle, is collected and read out by a photodiode [59].

In the barrel region, the wedge-shaped crystals (approximately $2.2 \times 2.2 \times 23$ cm, corresponding to 26 radiation lengths in depth) are arranged radially, covering up to

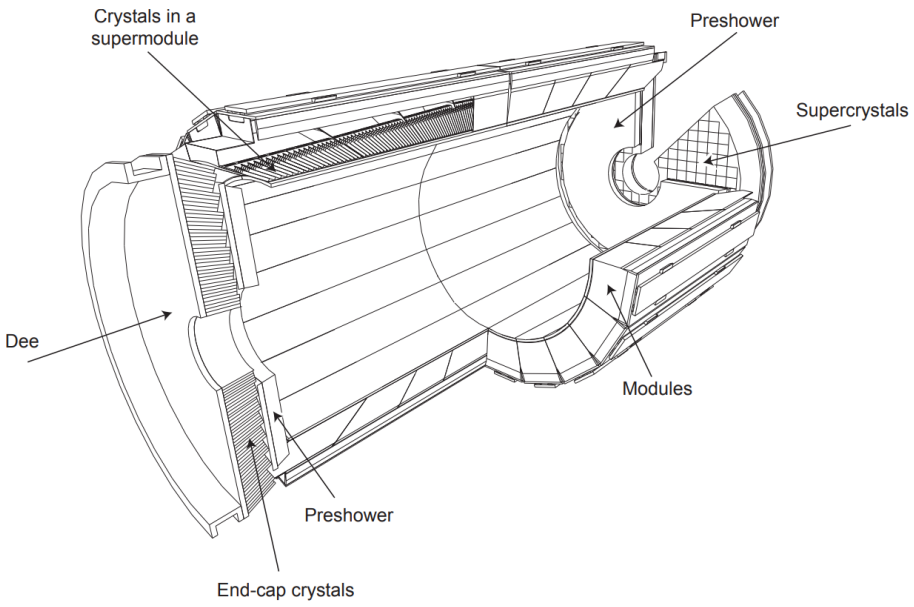

Figure 3-7: Schematic of the ECAL demonstrating the location and orientation of the crystals in the barrel and endcap. The radial pointing of the crystals is visible. [60]

$|\eta| < 1.49$. The endcap provides coverage from $1.47 < |\eta| < 3.0$, with the $3 \times 3 \times 22\,\text{cm}$ (approximately 25 radiation lengths) crystals arranged approximately parallel to the beamline. Crystal dimensions are compatible with electromagnetic shower sizes in $PbWO_4$. The orientation of the crystals depends on their $|\eta|$ position, as they are angled towards 3 deg of the collision point, as shown in Figure 3-8. The $PbWO_4$ crystals are radiation hard, but exposure to radiation damages the crystals, producing color centers which reduce the transparency of the crystal volume. Transparency loss and the associated change in energy response is most prominent in regions of high $|\eta|$ which were subjected to the highest levels of radiation [61]. These defects can anneal during times without collisions. The ECAL is equipped with a laser system which monitors the transparency of the crystals. Calorimeter performance can be maintained by accounting for the transparency loss experienced by indivdiual crystals [59].

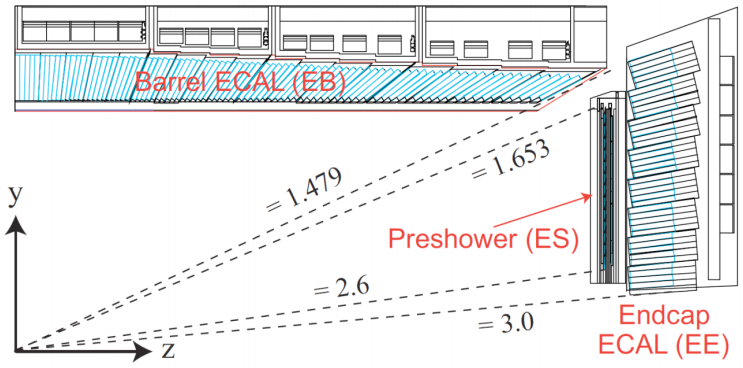

Figure 3-8: Quarter-view of the ECAL showing the position and orientation of the crystals. [60]

The ECAL energy resolution is described in Equation 3.1.

$$\frac{\sigma(E)}{E} = \frac{2.8\%\sqrt{\text{GeV}}}{\sqrt{E}} \oplus \frac{120\,\text{GeV}}{E} \oplus 0.3\% \tag{3.1}$$

The contributions to the energy resolution are, respectively, the stochastic term, electronics noise term, and the constant term. Stochastic term, $2.8\%\sqrt{\text{GeV}}/\sqrt{E}$, accounts for statistical fluctuations in shower detection, and it is small due to ECAL being a homogenous calorimeter. The constant noise term, 0.3%, includes detector calibration and instability [62].

3.2.4 Hadronic Calorimeter

The Hadronic Calorimeter (HCAL) measures the energy of charged hadrons.

The HCAL has four subsystems—Barrel (HB), Endcap (HE), Outer (HO), and Forward (HF)—with a quarter slice of the detector shown in Figure 3-9. HB, HE, and HO are sampling calorimeters using plastic scintillator and steel and brass absorbers. HB extends from the outside of the ECAL to the inner radius of the solenoid coil: $r = 1.77\,\text{m}$ - $r = 2.95\,\text{m}$ and covers $|\eta| < 1.3$ with an $\eta - \phi$ segmentation of 0.87×0.87. The interior absorber is a 40 mm thick steel plate, followed by eight layers of 50.5 mm thick brass plates interleaved with 3.7 mm thick plastic scintillator tiles, and final steel plate absorber 75mm thick, providing a total interaction length of $5.8\,\lambda_I$. The

layers of HO are situated at the outer radius of the solenoid, designed to catch showers for high energy hadrons that are not contained within the other HCAL subsystems. There is an extra HO layer near $|\eta| \approx 0$ where the interaction depth of the HB is shortest. The construction of HB and HE are cylindrically nested alternating layers of brass absorber and scintillator, with the first absorber layer made of steel. The HE extends coverage to $|\eta| < 3$, and consists of 10 layers of alternating scintillator and brass absorber, with a steel first absorber layer.

HF is a sampling calorimeter using quartz fibers embedded in steel. It is situated in the far forward region of the detector, with coverage up to $|\eta| < 5.2$. Due to its position, the HF experiences significantly higher particle flux than the other HCAL subsystems and the HF needed to have extremely fast response and radiation hardness [63].

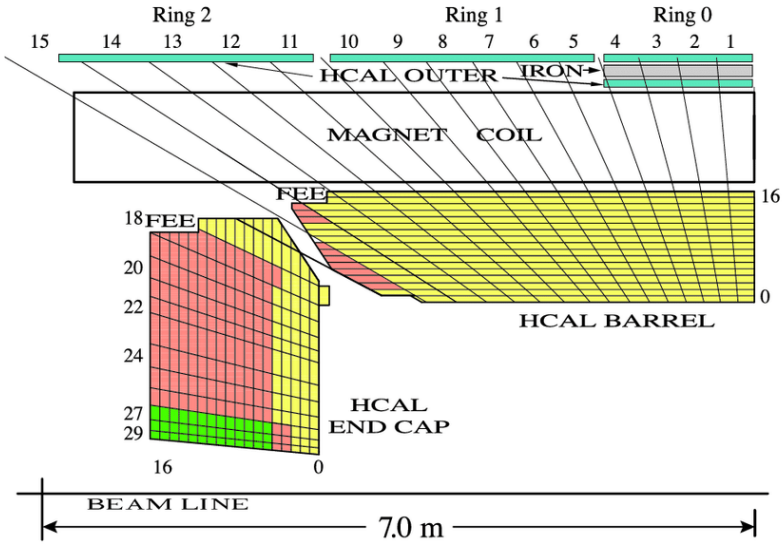

Figure 3-9: Quarter-view of the HCAL showing the positioning and segmentation of the barrel, endcap, and outer subsystems. [64]

The HCAL is a sampling calorimeter. Incident charged hadrons undergo multiple scattering within the absorber material, producing hadronic showers that propagate in the direction of the particles intial trajectory. As the showers develop, they pass through the absorber layer and traverse the scintillator layer, where the particles in the shower induce excitations resulting in scintillation light. The light is wavelength

shifted and carried by optical fibers to a photodiode where it is read out and digitized. In the HF, quartz fibers produce Cherenkov light.

The energy resolution of the HCAL, described in Equation 3.2 is representative of a sampling calorimeter. Resolution is affected by the limited detector volume available to the HCAL [65].

$$\frac{\sigma(E)}{E} = \frac{110\%\sqrt{\text{GeV}}}{\sqrt{E}} \oplus 7.3\% \tag{3.2}$$

The stochastic term ($110\%/\sqrt{E}$) accounts for the statistical fluctuations in shower detection, which is relatively large for the HCAL due to its design as a non-compensating sampling calorimeter. The constant 7.3% term is due to detector calibration limitations.

HCAL Reconstruction Algorithms

In HB and HE, the total pulse width from light collection and electronic readout is larger than the 25 ns separation between LHC bunch crossings. Output from the HPD is digitized and integrated in 25 ns-wide bins. Approximately 60% of the pulse width is contained within the first 25 ns and and 90% of the pulse is contained within the first 50 ns. LHC Run II conditions with 25 ns separation between bunch crossings potentially produces readout with substantial overlap between pulses generated by interactions from consecutive bunch crossings. An algorithm to perform hit reconstruction in each calorimeter tower was developed for Run II in order to mitigate the effect of out-of-time pileup events on the energy resolution of the HB and HE readout channels. This was achieved by assuming the presence of out-of-time pileup interactions from the immediately precedent and antecedent bunch crossings. A fitting template is constructed out of 3 HCAL pulse shape templates, where the free parameters are the arrival times and normalizations of each pulse as well as a floating baseline to accommodate noise. The resulting normalization of the in-time pulse determines the energy for the reconstructed hit in each channel. In addition to providing the offline HCAL hit reconstruction, the algorithm is used in HCAL opera-

tions and data validation. In addition to hit energy, the fitting procedure determines the arrival time with a resolution of 1 ns. This provides the ability to monitor and calibrate the relative timing of the channels in HB and HE.

3.2.5 Muon System

The outermost detector system is the muon chambers. Situated around the return yoke, the muon detectors are used for muon triggering, muon identification, and muon momentum measurement. Particles that make it through CMS and reach the muon systems are almost exclusively muons. Muon detector information is combined with tracking information to enhance muon reconstruction. The muon system uses three detector technologies: resistive plate chambers (RPC), drift tubes (DT), and cathode strip chambers (CSC) [66].

The barrel region technology is drift tubes, with coverage up to $|\eta| < 1.2$. These are suitable due to the fairly uniform magnetic field and low particle flux. The barrel region is constructed of four cylindrically nested sets of rectangular drift tube components, with 12 segments in ϕ, and panels at each radius grouped to form a muon station. The stations are located in alternating layers with the magnetic field return yoke. Each station consists of 8 layers of drift tubes. The arrangement of the barrel muon stations can be seen in Figure 3-10. The drift chambers containing a CO_2/Argon gas mixture, which has a drift velocity of 55 μm/ ns (about 400 ns maximum drift time) [67].

The endcap muon detectors use a cathode strip chamber (CSC). CSC are multi-wire proportional chambers with a cathode strip as the readout and can provide a precise location of ionization. The endcap stations are grouped by z position, covering $1.2 < |\eta| < 2.4$. CSCs are used in the endcap regions because their high granularity and short drift distance makes them more suitable for the higher event rate and non-uniform magnetic field in this region. The CSC strips are arranged radially, and contain 6 layers which each provide a 2-coordinate hit position in the $r - \phi$ plane. Additional readout is taken from the anode wires, which provide a rough position meaurement in r. In addition to the CSC and DT which provide full η coverage up

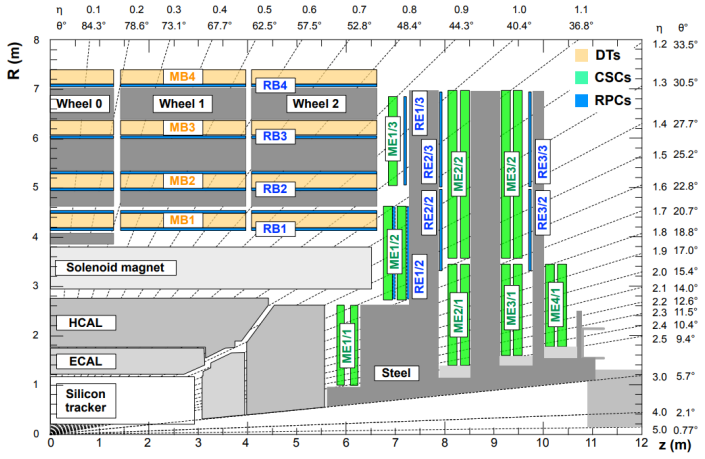

Figure 3-10: Quarter-view of the CMS muon system illustrating the position of the DT, CSC, and RPC detectors within the magnetic field return apparatus [67].

to $|\eta| < 2.4$, the muon system also utilizes a set of resistive plate chambers as an independent trigger system. The RPCs cover $|\eta| < 1.6$, and are a double-gap system operated in avalanche mode. The RPCs have poor position resolution, but have a response time of 1 ns and can be used to measure correct bunch crossing time at the highest LHC luminosities.

3.3 Data Acquisition and Trigger

The LHC provides pp collisions with a bunch spacing of 25 ns, which corresponds to a rate of 40 MHz. With multiple collisions occurring per bunch crossing, the event rate incident upon CMS is much higher than 40 MHz. The maximum final event rate needs to average on the order of 1 kHz, limited by the storage and data acquisition. In order to reduce the event rate while maintaining a high efficiency of selecting interesting physics processes, CMS uses a trigger system to make quick calculations and decisions about which events to keep or discard.

3.3.1 Trigger

The trigger systems are a two-stage decision-making tool, which reduce the event rate based on trigger primitives at varying levels of complexity. The stages of the trigger system are the Level One (L1) trigger and the and the High-Level Trigger (HLT) [68].

The L1 trigger resides on custom boards with field-programmable gate arrays (FPGAs). These contain pattern recognition algorithms that are able perform rough calculations to create candidate track segments and calorimeter clusters used for classification. The L1 operates with a latency of 3.8 μs per event, and full detector readout is held in a buffer while the L1 decision is made. L1 objects are energy clusters from ECAL and HCAL and muon track segments. Decisions are based on rough reconstrution of objects such as electrons, photons, muons, jets, and E_{T}^{miss}. Information flow in the L1 trigger is shown in Figure 3-11. The output rate of the L1 is limited to 100 kHz. Events which pass the L1 trigger are used to seed the more robust HLT analysis [68].

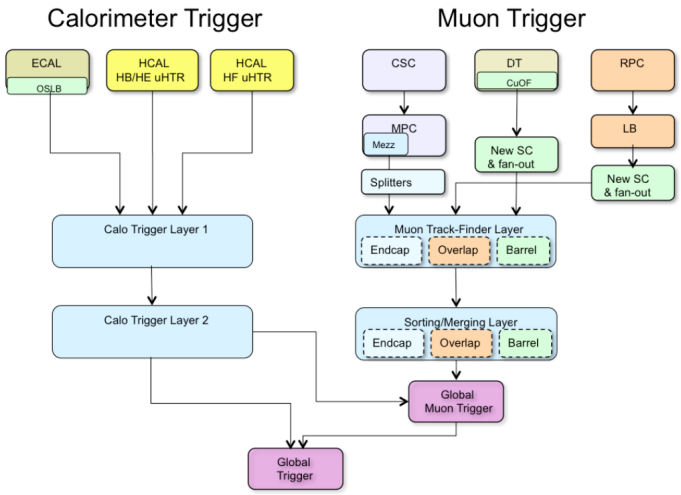

Figure 3-11: Schematic workflow of the L1 trigger. Information is first processed by the calorimeter and muon triggers, then combined at a global trigger [69].

The HLT system is a processor farm containing $O(10,000)$ CPU cores [70]. Here, fragments of events are combined to form complete events. The algorithms used to perform event reconstruction at the HLT level produce a similar quality as those

used in the offline reconstruction, and the HLT has access to the full event readout. HLT reconstruction is seeded by the L1 trigger decision. HLT paths allow for quick reconstruction by selectively filtering events as the reconstruction steps proceed—decisions are based on easily reconstructable calorimeter clusters or muon tracks, while computationally expensive track finding is only performed on events which pass the other criteria. Events passing selection by the HLT are saved to be fully reconstructed and stored for analysis use. The average event selection rate by the HLT is 1000 Hz [68].

3.3.2 Data Storage and Processing

Those events which pass the HLT filtering are stored on disk and eventually transferred to a Tier-0 computing center for full offline reconstruction and permanent storage. Data is stored and processed in part of a global computing grid, with multiple copies of datasets stored at computing centers around the world.

3.4 Detector Simulation

Physical processes originating at the pp collision point are simulated by a series of event generators, which are described in a later chapter. In addition to generating the pp collision products, the simulated event sets must also incorporate effects due to the full chain of particle interactions and detector readout in CMS.

Particle propagation through the detector volume is modeled by GEANT4 [71]. This toolkit allows a full geometric reconstruction of the detector, and handles the particle transport through the materials. Particle decays, bremsstrahlung, electromagnetic interactions, and hadronic interactions with the materials are modeled, as well as the effect of the magnetic field [72]. GEANT4 also handles detector response simulation, i.e. the simulation of optical photon production in a scintillator. Readout electronics, including associated noise, are also simulated.

Following the simulation of detector readout electrons, the simulated information is in the same format as data collected by the detector. At this stage, the full CMS

reconstruction is applied to the simulation in the same way it is applied to data.

3.5 Luminosity Calibration

An accurate luminosity measurement is necessary to provide an estimate of the correct production yield for the W and Z bosons. Luminosity calibration at CMS is calculated by readout from dedicated luminosity monitors, rates of reconstructed objects in CMS, and dedicated LHC configurations to perform Van der Meer scans.

During LHC operation, measurement of the instantaneous luminosity is based on the event rate recorded by several detectors. Online luminosity information is provided by dedicated luminometers—the Pixel Luminosity Telescope (PLT), Fast Beam Conditions Monitor, and the HCAL Forward calorimeter (HF)—which are operated on a separate readout from CMS physics data. Offline luminosity monitoring is based on data collected by CMS: rates of reconstructed pixel cluster counts and rates of tracks in the muon drift tubes [73].

Absolute calibration is determined by a Van der Meer (VdM) scan [74] [75], which utilizes a dedicated LHC configuration to scan the opposing proton beams transversely across each other. Data collected by CMS during these scans is used to reconstruct a beam profile and to determine the relationship of the instantaneous luminosity to the rates measured by the various luminosity monitoring systems.

Uncertainties in the luminosity measurement come from two primary categories. Normalization uncertainties, treated as uncorrelated, come from uncertainties of length scales and correlations when performing VdM scans. Integration uncertainties are related to detector operation and nonlinear detector response corrections [76].

Chapter 4

Event Reconstruction

Particles from collisions pass through CMS, producing signals in the various subdetectors. Events are reconstructed from the information delivered by the subsystems. This section outlines the method for reconstructing and identifying various components of events.

4.1 Tracks

Track reconstruction combines hits in the pixel and strip detectors, which are fit to construct tracks. Zero-suppressed signals in the pixel and strip detectors are clustered into hits, which provides hit position and uncertainty information. The track finding algorithm is an interative process which uses an implementation of the combinatorial Kalman Filter. The combinatorial Kalman Filter provides a combintation of pattern recognition and track fitting. The 6-pass iterative procedure initially finds the tracks that are easiest to identify, removes the hits associated with these tracks, and reiterates over the remaining collection of tracker hits. [77]

Electron tracks are seeded using three hits in the inner pixel detector which correspond approximately to a track from the beam spot. The innermost tracker layers are used because electrons undergo significant energy and trajectory loss due to bremsstrahlung and many charged pions undergo inelastic collisions as they traverse the inner tracking layers. The highly granular pixel detector has lower occupancy

than the outer strip detectors. These seed hits combined with the beam spot location provide enough information to derive parameters describing a helical trajectory as the particle moves through the magnetic field. The tracks are propagated outwards to subsequent tracker layers, incorporating additional hits if a χ^2 is below a target threshold. Track parameters are updated using a Gaussian Sum Filter (GSF) which incorporates multiple scattering models when reconstructing track hits [78].

Effects of tracker and support material on the energy loss and trajectory of particles traversing the tracker are also accounted for in this process. These effects are incorporated by Runge-Kutta based iterative propagator to describe a parametrized material distribution of the CMS detector and relevant interactions assuming every track is a pion.

Spurious track segments not corresponding to actual particle trajectories are removed after reconstruction. Requirements on minimum fit quality (χ^2/NDF), proximity to the primary vertex (Δz), and proximity to the beam spot ($d_0/\delta d_0$) are used to remove such tracks.

4.2 Primary Vertex

Primary vertex (PV) reconstruction ensures the position of each proton-proton interaction in every event. Reconstructed tracks with high fit quality and several tracker hits are propagated back to the beamline. A clustering algorithm combines the position of closest-approach to the beamline into vertices based on their z-axis location [77]. The clustering algorithm currently used is a deterministic annealing algorithm, which produces a high performance in successful cluster finding in a noisy environment [79]

4.3 Particle Flow

The CMS detector is suited to using the particle flow (PF) technique in event reconstruction. The general principal of PF is to combine information from tracks and

calorimeter deposits into one object. This analysis relies on the transverse missing energy (E_{T}^{miss}) as provided by the particle flow algorithm. This section describes the PF algorithm as well as the PF E_{T}^{miss}.

4.3.1 Particle Flow Reconstruction

Basic Elements

The basic elements of the PF algorithm are tracks in the tracker, track segments in the muon chambers, and energy clusters from the ECAL and HCAL. Calorimeter clustering begins with a local maximum energy deposition as a seed, and are grown by incorporating neighboring cells with an energy above a certain threshold. The threshold is 2σ above the standard electronic noise of the subdetector (80 MeV in ECAL Barrel, 300 MeV in ECAL Endcap, and 800 MeV in the HCAL). An individual particle will produce multiple PF elements, and a linking algorithm is used to incorporate the elements from each subsystem into one object.

Linking Algorithm

The linking algorithm finds the PF elements from each detector that correspond to individual objects and groups them together. Tracks are associated with calorimeter clusters by extrapolating from the outermost tracker hit, through the preshower and ECAL, and one interaction length into the HCAL. Pairwise matching between the extrapolated track and nearby calorimeter clusters is performed, and linking occurs if the track extrapolation falls within the cluster cells as measured in the (η, ϕ) plane for the ECAL barrel and HCAL and (x, y) plane for the ECAL endcap and preshower. Calorimeter-to-calorimeter cluster linking is performed in a similar way by extrapolating clusters between the ECAL and HCAL, seeded with the cluster from the more granular detector.

In cases where multiple objects from one detector are linked with the same object from another detector, only the pair with the closest link (best fit) is kept.

Bremsstrahlung photons in the ECAL are linked by searching for ECAL clusters

which are consistent with a tangential projection from the GSF electron track reconstruction. Additionally, bremsstrahlung photons radiated within the tracker are identified by tracks corresponding to photon conversion and can be linked to the GSF electron.

Linking information from the muon chambers is also performed, and is described in the muon reconstruction Section 4.5.

4.3.2 E_{T}^{miss}

Missing transverse energy (E_{T}^{miss}) is used to describe imbalances in energy deposition, projected into the transverse plane. E_{T}^{miss} is defined as the negative vector sum of all transverse momenta in an event, as in Equation 4.1.

$$E_T^{miss} = -\sum_p \vec{p_T} \tag{4.1}$$

Particle flow E_{T}^{miss} is constructed from reconstructed PF particles.

4.4 Electron Reconstruction

Electron reconstruction starts with an energy deposition in the ECAL, known as a supercluster. With the supercluster as a seed, a track is projected inwards from the ECAL, and pairs of hits in the silicon pixel tracker are searched for. From these, further tracker hits compatible with the trajectory are incorporated into the electron reconstruction. Due to Bremsstrahlung, electrons lose significant amounts of energy and change trajectory. The Bremsstrahlung losses are accounted for using a set of possible energy loss models. This is incorporated using a weighted technique known as a Gaussian Sum Filter (GSF) algorithm.

From the electron track reconstruction, multiple observables describing the kinematics of the electron, the surrounding event, and quality of the reconstruction are produced. These are later used to identify candidate electrons originating in the signal processes for this analysis,as described in Chapter 5.6.2.

4.5 Muon Reconstruction

Standalone Muons

A standalone muon track is built solely from information collected by the muon chambers. Energy depositions in the CSC and DT are combined as track segments. These are used as seeds for track reconstruction from the muon chambers CSC, DT, and RPCs, which are combined using a Kalman filter [80].

Global Muons

The global muon reconstruction starts with an energy deposition in the muon chambers which is propagated inwards towards the inner tracker. Standalone muon tracks are used as the seed for global muon reconstruction. Kalman filter techniques are used to combine the tracker and muon track segments to form a global muon. Energy loss effects due to detector material and support structure between the tracker and muon chambers are also accounted for. Global muon reconstruction improves momentum resolution for muons with $p_{\mathrm{T}} > 200\,\mathrm{GeV}$.

Tracker Muons

Tracker muons are muons which are identified as tracks in the tracker with at least $p_{\mathrm{T}} > 0.5$ and $p > 2.5\,\mathrm{GeV}$. Tracker muon reconstruction is similar to global muon reconstruction, but the seed is a track segment from the inner tracker as opposed to a muon track segment.

Chapter 5

Data Samples and Event Selection

The data used in this analysis were collected in late 2017 by the CMS Experiment during Run II of the LHC. At this time, the LHC delivered two sets of pp collisions, at $\sqrt{s} = 5.02\,\text{TeV}$ (2017G) and at $\sqrt{s} = 13\,\text{TeV}$ (2017H) with special run conditions which are specifically motivated by precision electroweak measurements. This chapter provides details of the run conditions, data collection, and Monte Carlo simulations associated with these data taking periods. Details regarding the object identification criteria and event selection are also provided.

5.1 Datasets

Data used in this analysis are from the LHC run eras 2017G and 2017H, consisting of pp collisions at $\sqrt{s} = 5.02\,\text{TeV}$ with integrated luminosity $\mathcal{L} = 299.1 \pm 5\,\text{pb}^{-1}$ and $\sqrt{s} = 13\,\text{TeV}$ with integrated luminosity $\mathcal{L} = 199.3 \pm 4\,\text{pb}^{-1}$, respectively. These two data taking periods had special run conditions with very few additional pp collisions in concurrent or adjacent bunch crossings. The additional collisions are referred to as pileup events. Runs with low pileup are particularly suited for electroweak precision measurements such as this one, as additional pileup events contribute to increased background and worsening object resolution. Names of the data streams and relevant run era and reconstruction version identifications are listed in Table 5.2 and Table 5.1.

Data stream	Run & version
SingleMuon	Run2017G-17Nov2017-v1
HighEGJet	Run2017G-17Nov2017-v2

Table 5.1: Data streams and the respective run and reconstruction versions for the 2017G (5.02 TeV) data taking.

Data stream	Run & version
SingleMuon	Run2017H-17Nov2017-v2
HighEGJet	Run2017H-17Nov2017-v1

Table 5.2: Data streams and the respective run and reconstruction versions for the 2017H (13 TeV) data taking.

5.2 Triggers

All events considered must have at least one lepton selected by the relevant trigger path. For muons, the kinematic requirement is $p_{\mathrm{T}} > 17\,\mathrm{GeV}$ and $|\eta| < 2.4$ for both $\sqrt{s} = 5.02\,\mathrm{TeV}$ and $\sqrt{s} = 13\,\mathrm{TeV}$. For electrons, the kinematic requirement is $p_{\mathrm{T}} > 20\,\mathrm{GeV}$ ($p_{\mathrm{T}} > 17\,\mathrm{GeV}$) and $|\eta| < 2.5$ for $\sqrt{s} = 5.02\,\mathrm{TeV}$ ($\sqrt{s} = 13\,\mathrm{TeV}$). Additional isolation and reconstruction quality criteria, which are less restrictive than the offline selection criteria, are applied at the trigger level. The trigger menus used in the low pileup runs include triggers with looser selection criteria which are not used in normal LHC run conditions. Names of the trigger paths are listed in Table 5.3

$\sqrt{s} = 13\,\mathrm{TeV}$	$\sqrt{s} = 5.02\,\mathrm{TeV}$
`HLT_HIEle20_WPLoose_Gsf`	`HLT_HIEle17_WPLoose_Gsf`
`HLT_HIMu17`	`HLT_HIMu17`

Table 5.3: Data streams and reconstruction versions for the 2017G (5.02 TeV) data taking.

5.3 Luminosity

Data used for physics analyses are required to pass the quality certification regarding operation of detector subsystems during the data taking period. Pileup conditions during the data taking periods are shown in Figure 5-1 (Figure 5-2) for 2017H (2017G), with an average of $\langle\mu\rangle = 3$ collisions per bunch crossing. Uncertainties on the luminosity measurement are 1.7% (3.5%) for the certified data at $\sqrt{s} = 13\,\text{TeV}$ ($\sqrt{s} = 5.02\,\text{TeV}$). The total integrated luminosity collected by the data streams during $\sqrt{s} = 5.02\,\text{TeV}$ and $\sqrt{s} = 13\,\text{TeV}$ are listed in Table 5.4 [76, 81].

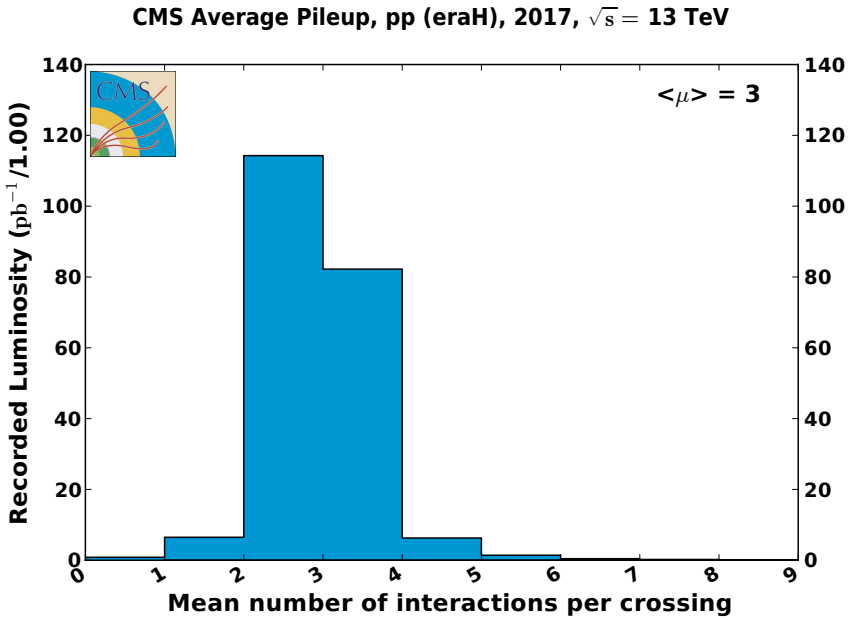

Figure 5-1: Distribution of the number of interactions per bunch crossing for the low pileup $\sqrt{s} = 13\,\text{TeV}$ (2017H) data taking period. The average number of interactions per crossing is $< \mu >= 3$ [81].

$\sqrt{s}$ [TeV]	Run Era	Luminosity [pb^{-1}]
5.02	2017G	199.2 ± 3.39
13	2017H	291.1 ± 11.64

Table 5.4: Datasets and their respective integrated luminosity measurements.

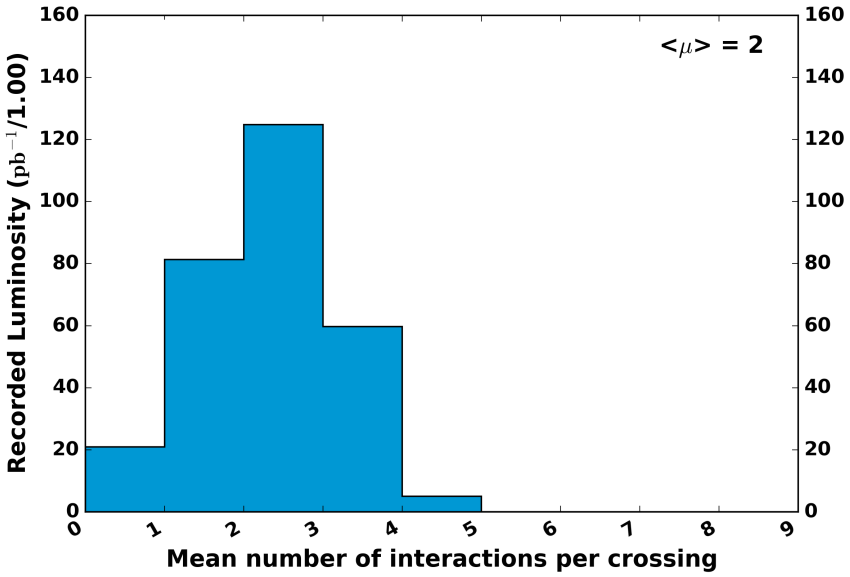

Figure 5-2: Distribution of the number of interactions per bunch crossing for the $\sqrt{s} = 5.02\,\text{TeV}$ (2017G) data taking period. The average number of interactions per crossing is $< \mu >= 2$ [81].

5.4 Simulated samples

Several simulated Monte Carlo (MC) samples are used in the descriptions of signal and background processes. The $W^{\pm}$ and Z boson signal events are simulated at next-to-leading order (NLO) with up to two outgoing partons at Born level by MADGRAPH5_aMC@NLO 2.3.3 [82]. An additional set of simulations of the $W^{\pm}$ and Z boson signal processes are provided at NLO by POWHEG 2.0 [83–86] for the $W^{\pm}$ and MINLO [87] for the Z boson. Background samples (di-boson and $t\bar{t}$) are also simulated with POWHEG 2.0. Underlying event modeling, parton showering, hadronization, and final state radiation are done by PYTHIA 8.230 [88], using tune CP5 [89] and default parton distribution functions (PDFs) provided by NNPDF3.1 [43]. Primary sample names and their respective production cross sections are listed in Table 5.5 (Table 5.6) for $\sqrt{s} = 5.02\,\text{TeV}$ ($\sqrt{s} = 13\,\text{TeV}$).

The distribution of pileup interactions is simulated to match the corresponding conditions in data. For all simulated samples, simulation of detector response is performed by GEANT4 [90], with full event reconstruction being done using the same

algorithms used to reconstruct data. Object and event reconstruction was described in Chapter 4.

Sample name	Generator	Cross section [pb]
W+Jets	aMC@NLO	21159
$WW \to 2\ell 2\nu$	POWHEG	2.52
$WZ \to 3\ell\nu$	POWHEG	1.23
$ZZ \to 4\ell$	POWHEG	2.75
$ZZ \to 2\ell 2\nu$	POWHEG	2.75
$t\bar{t}$	POWHEG	69.5
DY+jets$\to \ell\ell$	aMC@NLO	2141

Table 5.5: Names and cross sections of simulated samples corresponding to run era 2017G ($\sqrt{s} = 5.02\,\text{TeV}$).

Sample name	Generator	Cross section [pb]
W+0 jets	aMC@NLO	49397
W+1 jets	aMC@NLO	8087
W+2 jets	aMC@NLO	3176
ZZ	POWHEG	16.523
$WZ \to 3\ell\nu$	POWHEG	4.912
$WZ \to 2\ell 2\nu$	POWHEG	12.6
$t\bar{t} \to 2\ell 2\nu$	POWHEG	88.29
$t\bar{t} \to$ semileptonic	POWHEG	365.35
$t\bar{t} \to$ hadronic	POWHEG	377.96
DY+jets$\to \ell\ell$	aMC@NLO	6225.42

Table 5.6: Names and cross sections of simulated samples corresponding to run era 2017H ($\sqrt{s} = 13\,\text{TeV}$).

5.5 Event Selection & Fiducial Region

Preliminary $W^{\pm}$ and Z boson event candidates are identified by the presence of at least one lepton identified by the single electron and single muon triggers described in Section 5.2. These are further selected by applying the offline electron or muon reconstruction identification criteria described in Section 5.6.

Z boson selection

Candidate Z boson events are selected using the following criteria:

- two well-identified leptons
- leptons are oppositely charged
- leptons are same flavor
- at least one lepton matched to trigger
- $60\,\text{GeV} \leq \text{M}_{ll} \leq 120\,\text{GeV}$

W boson selection

Candidate W boson events are selected using the following criteria:

- well-identified lepton
- lepton matched to trigger
- veto against events containing additional leptons

Fiducial Region

The fiducial region for the $W^{\pm}$ and Z boson acceptance at generator-level emulates the selection at reconstruction level. This requires kinematic cuts $p_{\text{T}} > 25\,\text{GeV}$ and $|\eta| < 2.4$ for all charged leptons. Additionally, the Z boson fiducial region includes a requirement on the dilepton mass: $60\,\text{GeV} \leq \text{M}_{ll} \leq 120\,\text{GeV}$. The fiducial region for the W boson includes the transverse mass requirement $m_{\text{T}} > 40\,\text{GeV}$.

5.6 Object Identification

The W and Z boson candidates are identified by the presence of one or two, respectively, well-identified leptons passing a strong set of criteria ensuring proper reconstruction and identification. This section contains a description of the identification requirements for the $W \to \ell\nu$ and $Z \to \ell\ell$ signal leptons, as well as the requirements for the lepton veto for the $W^{\pm}$ boson selection.

5.6.1 Isolation

One of the most important observables used to separate the leptons from W^+ and W^- boson events from QCD background is the isolation. Isolated leptons have little other activity within a cone of $\Delta R < 0.3$, and leptons from $W \to \ell\nu$ decays are generally isolated. The isolation of a lepton is constructed from the sum of all charged and neutral hadrons and ECAL deposits within $\Delta R < 0.3$ of the lepton, as shown in Equation 5.1.

$$I_{PF} = \frac{1}{p_{\mathrm{T}}} \sum_{\Delta R<0.3} (p_{\mathrm{T}}^{h^0} + p_{\mathrm{T}}^{h^\pm} + p_{\mathrm{T}}^{\gamma}) \tag{5.1}$$

The individual contributions to the PF isolation are the sums of corresponding particle types which fall within a cone of $\Delta R < 0.4$.

5.6.2 Electrons

Electrons originating from candidate W^+, W^-, and Z bosons are required to pass a standard cut-based identification. Backgrounds producing electron-like signatures include overlapping charged and neutral pions, pions showering in the ECAL, and jets, and the selection criteria are designed to exclude these. The thresholds for observables required to pass this requirement are listed in Table 5.7. Descriptions of the observables are provided below. The $W^\pm$ boson selection requires the absence of additional leptons in the event. The veto is performed with leptons fulfilling the loose working point identification requirements, with criteria for electrons listed in Table 5.8.

Electron Observables

- **($\Delta\eta_{In}$,$\Delta\phi_{In}$):** Geometric matching of the ECAL supercluster and electron GSF track, extrapolated to the vertex. Real electrons are well-matched since they come from the same object.

- **$\sigma_{i\eta i\eta}$:** Shape of the shower in the ECAL. Electrons can be discriminated from jets by the evolution of the shower in the 5x5 crystal region around the seed.

- **H/E:** Ratio of energy deposited in HCAL to ECAL. Electrons tend to deposit most of their energy in the ECAL, while jets deposit substantial amounts their of energy in the HCAL.

- $|d_{0,bs}|$**,** $|d_{z,bs}|$**:** Impact parameters are defined as the distance of closest approach of the track to the vertex. Requiring an impact parameter cut removes electrons from displaced vertices.

- $|1/E - 1/p|$**:** Electron energy measured in ECAL is compatible with momentum measured in tracker.

- **Number of Missing Hits**: Number of missing tracker hits in tracker layer

- **Isolation:** Requiring that electrons be isolated reduces the number of jets reconstructed as electrons.

- **Conversion probability**: Photons converting to electron-positron pairs are a source of isolated electrons. Electrons from photon conversion are identified by fitting e^+e^- pairs to a common vertex.

Observable	Barrel	Endcap
p_T	> 25 GeV	
$\|\eta\|$	< 2.4	
$\Delta\eta_{In}$	< 0.0032	< 0.00632
$\Delta\phi_{In}$	< 0.0547	< 0.0394
$\sigma_{i\eta i\eta}$	< 0.0106	< 0.0387
H/E	$< 0.046 + 1.16/E_{SC} + 0.0324\rho/E_{SC}$	$< 0.0275 + 2.52/E_{SC} + 0.183\rho/E_{SC}$
$\|d_{0,bs}\|$	< 0.05	< 0.10
$\|d_{z,bs}\|$	< 0.10	< 0.20
$\|1/E - 1/p\|$	< 0.184	< 0.0721
$\text{Iso}_{\text{PF}}/p_{\text{T}}$	$< 0.0478 + 0.506/p_{\text{T},ele}$	$< 0.0658 + 0.963/p_{\text{T},ele}$
Missing Hits	≤ 1	
Pass conversion veto		

Table 5.7: Reconstructed identification and isolation criteria fulfilling the medium cut-based ID for electron selection.

Observable	Barrel	Endcap
p_T	> 25 GeV	
$\|\eta\|$	< 2.4	
$\Delta\eta_{In}$	< 0.00463	< 0.00814
$\Delta\phi_{In}$	< 0.148	< 0.19
$\sigma_{i\eta i\eta}$	< 0.0126	< 0.0457
H/E	$< 0.05 + 1.16/E_{SC} + 0.0324\rho/E_{SC}$	$< 0.05 + 2.54/E_{SC} + 0.183\rho/E_{SC}$
$\|d_{0,bs}\|$	< 0.05	< 0.10
$\|d_{z,bs}\|$	< 0.10	< 0.20
$\|1/E - 1/p\|$	< 0.209	< 0.132
$\text{Iso}_{\text{PF}}/p_{\text{T}}$	$< 0.198 + 0.506/p_{T,ele}$	$< 0.203 + 0.963/p_{T,ele}$
Missing Hits	≤ 2	≤ 3
Pass conversion veto		

Table 5.8: Reconstructed identification and isolation criteria fulfilling the loose cut-based ID for electron selection used as a veto on $W^{\pm}$ events with additional leptons present.

5.6.3 Muons

Muons originating from a candidate $W^{\pm}$ or Z boson are required to pass the standard cut-based identification with an additional requirement on muon isolation. The thresholds for observables required to pass this requirement are listed in Table 5.9. Descriptions of the observables are provided below. As in the electron channel, the $W^{\pm}$ boson selection requires the absence of additional leptons in an event which pass the loose cut-based ID. The criteria for muons is listed in Table 5.10.

Muon Observables

- **Global Muon & PF Muon:** Muon candidate is successfully reconstructed by these algorithms

- χ^2**/ndof:** Quality of the muon track fit, require convergence of the fit.

- **Number of Valid Hits:** Number of muon system hits included in the global muon reconstruction. Global muons rarely have 0 valid hits.

- **Number of Matched Stations:** Number of muon segments in the muon stations

- **Number of Pixel Hits:** Activity in the pixel tracker associated with the muon removes muons from backgrounds such as cosmic rays and decay-in-flight of pions and kaons.

- **Number of Tracker Hits:** Similar to the pixel tracker requirements, the total number of tracker hits can further reduce backgrounds from decay-in-flight.

- $|d_{0,bs}|$**,** $|d_{z,bs}|$**:** Impact parameters d_0 and d_z are defined as the distance of closest approach of a track to the primary interaction vertex. Removes muons from displaced vertices and cosmic rays.

- **Isolation:** Muons originating from heavy flavor decays often have other leptons and light mesons nearby, and are therefore less isolated.

Observable	Value/Range
p_{T}	> 25 GeV
$\lvert\eta\rvert$	< 2.4
ID	GlobalMuon
ID	PFMuon
χ^2/ndof	< 10
# Valid Mu Hits	≥ 1
# Matched Stations	≥ 2
# Tracker Layers	≥ 6
# Valid Pixel Hits	≥ 1
$\lvert d_{0,bs}\rvert$	< 0.2
$\lvert d_{z,bs}\rvert$	< 0.5
$\mathrm{Iso}_{\mathrm{PF}}/p_{\mathrm{T}}$	< 0.15

Table 5.9: Reconstructed identification and isolation criteria fulfilling the cut-based ID with tight isolation requirement for muon selection.

Observable	Value/Range
p_{T}	> 10 GeV
$\lvert\eta\rvert$	< 2.4
ID	GlobalMuon **OR** TrackerMuon
ID	PFMuon

Table 5.10: Reconstructed identification and isolation criteria for identifying additional muons used as a veto on $W^{\pm}$ boson events.

Chapter 6

Acceptance

6.1 Acceptance Calculation

The acceptance, A, for $W^{\pm}$ and Z boson events is the fraction of simulated events producing decay products within the fiducial volume satisfying the geometric and kinematic requirements. The specific requirements are $p_{\mathrm{T}} > 25\,\mathrm{GeV}$ and $|\eta| < 2.4$ for both electrons and muons (Table 6.1). An additional requirement on transverse mass, $m_{\mathrm{T}} > 40\,\mathrm{GeV}$, is applied for $W^{\pm}$ events. For Z events, only those which are generated with $60\,\mathrm{GeV} \leq \mathrm{M}_{ll} \leq 120\,\mathrm{GeV}$ are considered. Generator-level acceptance can be

Observable	Muon	Electron
$\lvert\eta\rvert$	< 2.4	< 2.4
p_T	> 25 GeV	> 25 GeV

Table 6.1: Kinematic and fiducial requirements for leptons.

computed before and after the effects of final-state radiation (FSR) are simulated. The acceptance values for W^+, W^-, and Z bosons are calculated from aMC@NLO with NNPDF3.1 PDF and PYTHIA 8.2 for parton showering are shown in Table 6.2 (Table 6.3) for $\sqrt{s} = 5.02\,\mathrm{TeV}$ ($\sqrt{s} = 13\,\mathrm{TeV}$). The post-FSR column indicates that the leptons have undergone bremsstrahlung, and the dressed lepton category incorporates final state radiation photons into the lepton kinematics. This is done by identifying any photons which are within $\Delta R < 0.1$ of the lepton and adding

them back to the lepton momentum vector. Statistical uncertainty in the generator-level acceptance is negligible. Additional uncertainties from theoretical sources are discussed in the next section.

Process	$A_{Gen}(\text{Post} - \text{FSR})$	$A_{Gen}(\text{Dressed})$
$W \to e^+\nu$	0.535	0.556
$W \to e^-\nu$	0.504	0.521
$W \to e\nu$	0.523	0.542
$Z \to ee$	0.445	0.468
$W \to \mu^+\nu$	0.548	0.555
$W \to \mu^-\nu$	0.514	0.518
$W \to \mu\nu$	0.535	0.541
$Z \to \mu\mu$	0.461	0.468

Table 6.2: Acceptance for post-FSR and dressed leptons at $\sqrt{s} = 5.02\,\text{TeV}$.

Process	$A_{Gen}(\text{Post} - \text{FSR})$	$A_{Gen}(\text{Dressed})$
$W \to e^+\nu$	0.418	0.434
$W \to e^-\nu$	0.434	0.449
$W \to e\nu$	0.425	0.440
$Z \to ee$	0.360	0.378
$W \to \mu^+\nu$	0.427	0.433
$W \to \mu^-\nu$	0.443	0.448
$W \to \mu\nu$	0.434	0.439
$Z \to \mu\mu$	0.372	0.378

Table 6.3: Acceptance for post-FSR and dressed leptons at $\sqrt{s} = 13\,\text{TeV}$.

6.2 Systematic Uncertainty

Uncertainties in the measurement due to theoretical predictions are studied by using the acceptance and comparing baseline values to alternate predictive models. The differences are taken as the uncertainties.

PDF uncertainties

The proton PDFs describe the momentum probability distributions of quarks and gluons within the proton, and are obtained by fitting to experimental data. Several different collaborations produce PDFs, with derivations using different techniques

and different datasets. Methods for evaluating uncertainties in the PDFs due to uncertainties in their parameters are also provided, generally in the form of error PDFs with a $\pm 1\sigma$ variation on each parameter value. NNPDF provides replica PDFs which are created by using a Monte Carlo technique to sample the probability distributions of observables. Following the procedure outlined in Reference [46], the uncertainty in acceptance due to the PDF uncertainties is taken as the standard deviation of the replica set acceptance values. Results are listed in Table 6.4 and Table 6.5.

Resummation and NNLO QCD

For low-p_{T} boson production, the fixed order calculations are unreliable due to soft gluon emissions producing logarithmic divergences in the cross section calculation [91]. Resummation of the logarithmic terms is included as one of the components of the boson production cross section, and different tools can provide predictions to different orders of accuracy. Parton shower models with leading logarithmic (LL) accuracy (e.g. PYTHIA, SHERPA, HERWIG [88, 92, 93]) can be combined with fixed-order calculations (e.g. aMC@NLO, MINLO, POWHEG) to provide full event descriptions [82, 86, 94, 95]. Higher-order resummation terms can be matched to the fixed-order calculations to provide accurate predictions over the entire boson p_{T} range [96, 97]. The primary simulations are provided by aMC@NLO, interfaced to PYTHIA 8 for parton showering and MadGraph 5 for the hard-scatter matrix element calculations. Resummation to LL is provided by PYTHIA 8 and QCD calculations to NLO are provided by MadGraph 5. Higher-order descriptions—NNLO for perturbative QCD and next-to-next-to-leading-logarithmic (NNLL) for resummation of soft QCD effects—are provided by RESBOS [98–100] for $\sqrt{s} = 13\,\mathrm{TeV}$ and DY-TURBO using the CT14 [101] NNLO PDF set for $\sqrt{s} = 13\,\mathrm{TeV}$ and $\sqrt{s} = 5.02\,\mathrm{TeV}$ as no RESBOS grids exist yet for $\sqrt{s} = 5.02\,\mathrm{TeV}$. Differences in acceptance predictions between the baseline sample with QCD to NLO and resummation to LL and the DY-TURBO prediction with QCD to NNLO and resummation to NNLL are taken as the uncertainties.

Higher-Order QCD

Perturbative QCD predictions for W and Z boson production are currently only available to NNLO [102, 103]. To estimate the effect of the missing higher-order terms of the expansion, the renormalization (μ_R) and factorization (μ_F) scales are varied by a factor of 2 from their baseline value, i.e. baseline $\mu = M_W$ with variations $\mu = M_W/2$ and $\mu = 2M_W$. Acceptance computed for each combination of μ_R and μ_F variations is compared to the baseline acceptance value and the maximum difference is used to estimate the uncertainty due to missing higher-order QCD terms. Results (as a percentage of the acceptance) are shown in Table 6.4 and Table 6.5.

Electroweak Corrections

The electroweak corrections include both types of radiative photon corrections—final state radiation(FSR) and higher-order corrections in α. Final state radiation is photons originating from the final state leptons. Higher-order electroweak include radiated photons originating from the W or Z boson as well as loop corrections. The baseline sample uses PYTHIA 8 which provides electroweak calculations to LO. To estimate the effect of the NLO electroweak terms, PHOTOS [104] is used as a comparison. Because PHOTOS cannot be interfaced to the aMC@NLO generator, two additional sets of simulations are produced using POWHEG as a generator, interfaced with PHOTOS or PYTHIA 8. The difference in acceptance values between the two simulations is taken to be the uncertainty due to FSR modeling and missing higher-order electroweak terms.

Source	W^+	W^-	W	W^+/W^-	Z	W^+/Z	W^-/Z	W/Z
QCD	0.273	0.221	0.249	0.058	0.242	0.166	0.133	0.151
PDF	0.388	0.349	0.350	0.253	0.404	0.249	0.209	0.194
Resummation	0.705	0.638	0.679	0.067	0.391	0.317	0.251	0.291
EWK & FSR	0.333	0.247	0.214	0.275	0.083	0.414	0.140	0.297
Total [%]	0.91	0.80	0.83	0.38	0.62	0.60	0.38	0.48

Table 6.4: Uncertainties (as % of acceptance) from theory sources for all muon channel measurements at $\sqrt{s} = 13\,\text{TeV}$.

Source	W^+	W^-	W	W^+/W^-	Z	W^+/Z	W^-/Z	W/Z
QCD	0.262	0.233	0.243	0.080	0.251	0.118	0.147	0.127
PDF	0.386	0.348	0.351	0.253	0.412	0.241	0.212	0.192
Resummation	0.637	0.638	0.639	0.002	0.379	0.258	0.260	0.260
EWK & FSR	0.140	0.058	0.186	0.108	0.048	0.090	0.198	0.137
Total [%]	0.80	0.76	0.79	0.28	0.61	0.38	0.41	0.37

Table 6.5: Uncertainties from theory sources (as % of acceptance value) for muon channels at $\sqrt{s} = 13\,\text{TeV}$.

Source	W^+	W^-	W	W^+/W^-	Z	W^+/Z	W^-/Z	W/Z
QCD	0.246	0.155	0.211	0.138	0.203	0.447	0.357	0.412
PDF	0.121	0.188	0.103	0.225	0.179	0.230	0.251	0.212
Resummation	0.239	0.342	0.274	0.102	0.143	0.098	0.200	0.132
EWK & FSR	0.333	0.247	0.214	0.275	0.083	0.414	0.140	0.297
Total [%]	0.49	0.49	0.42	0.39	0.31	0.66	0.50	0.56

Table 6.6: Uncertainties (as % of acceptance) from theory sources for all electron channel measurements at $\sqrt{s} = 5.02\,\text{TeV}$.

Source	W^+	W^-	W	W^+/W^-	Z	W^+/Z	W^-/Z	W/Z
QCD	0.244	0.199	0.226	0.136	0.193	0.435	0.392	0.418
PDF	0.115	0.188	0.102	0.223	0.175	0.223	0.248	0.206
Resummation	0.168	0.397	0.255	0.228	0.154	0.016	0.243	0.101
EWK & FSR	0.140	0.058	0.186	0.108	0.048	0.090	0.198	0.137
Total [%]	0.34	0.48	0.40	0.36	0.30	0.50	0.56	0.49

Table 6.7: Uncertainties from theory sources (as % of acceptance value) for muon channels at $\sqrt{s} = 5.02\,\text{TeV}$.

Chapter 7

Lepton Efficiency Scale Factors

The efficiency of the trigger and reconstruction and identification steps for leptons is non-unity and differs between simulation and data. Determining the efficiency of the reconstruction and identification stages in simulation and data provides a scale factor $\epsilon_{data}/\epsilon_{MC}$ for each lepton to effectively match the reconstruction efficiency of simulation to data. The scale factor is applied to the simulated signal and background samples to emulate the lepton reconstruction and identification efficiency expected in data. Efficiency scale factors are derived for leptons in $|\eta| < 2.4$ and $p_{\mathrm{T}} > 25\,\mathrm{GeV}$, with sufficient p_{T} and η granularity chosen to separate behavior in different kinematic regions and detector geometries. The factorization of the efficiency categories for electrons is shown in Equation 7.1 and for muons in Equation 7.2.

$$\epsilon_e = \epsilon_{GSF+Sel+ISO} \times \epsilon_{Trigger} \tag{7.1}$$

$$\epsilon_\mu = \epsilon_{Sel+ISO+Trk} \times \epsilon_{Sta} \times \epsilon_{Trigger} \tag{7.2}$$

The efficiency categories for electrons are:

- $\epsilon_{GSF+Sel+ISO}$: Efficiency of reconstructing a GSF electron which passes the electron selection requirements
- $\epsilon_{Trigger}$: Efficiency of a GSF electron passing selection requirements being selected by the trigger

Likewise the categories for muons are:

- ϵ_{Sta}: Efficiency for a global muon to be matched to the standalone muon system
- $\epsilon_{Sel+Iso+Trk}$: Efficiency of a standalone muon to be matched to a global muon with tracker hits as well as satisfying the muon selection and isolation criteria
- $\epsilon_{Trigger}$: Efficiency of a fully reconstructed muon passing selection requirements also being selected by the trigger

In the simulated $Z \to \ell\ell$ events, it is further required that both of the leptons be matched with $\Delta R < 0.5$ to a generator-level lepton originating from the Z boson.

7.1 Tag and Probe

A tag-and-probe method is employed on the $Z \to \ell\ell$ sample, with leptons required to have $p_{\mathrm{T}} > 25\,\mathrm{GeV}$ and $|\eta| < 2.4$. $Z \to \ell\ell$ events provide a high-purity sample of high-p_{T} leptons which have similar kinematic properties to those also present in the leptonic W boson decays [105]. Tag leptons are required to pass the standard analysis selection cuts as well as be matched to the appropriate trigger. Probe leptons are then selected from leptons passing the loose kinematic cuts of $p_T > 25$ GeV, $|\eta| < 2.4$, and producing a tag+probe invariant mass in the range $60\,\mathrm{GeV} \leq \mathrm{M}_{ll} \leq 120\,\mathrm{GeV}$. Probes are classified by their ability to pass a set of criteria depending on the efficiency category being studied. Calculation of the efficiency is described in Section 7.2.

Lepton efficiencies are calculated based on the probe p_{T} and η. Binning by η is listed in Table 7.1 and binning by p_{T} is listed in Table 7.2. Identical (p_{T}, η) binning is used at $\sqrt{s} = 5.02\,\mathrm{TeV}$ and $\sqrt{s} = 13\,\mathrm{TeV}$ for a given category. The trigger efficiency for all channels is derived with positively and negatively charged categories separated, while the charges are combined for the other categories [106]. Electron efficiency η binning includes a category specifically to accommodate the gap between the endcap and barrel which contains a large amount of inactive material and has a significantly lower efficiency than other areas.

Channel	η bins
Muon	-2.4, -2.1, -1.6, -1.2, -0.9, -0.3, 0, 0.3, 0.9, 1.2, 1.6, 2.1, 2.4
Electron	-2.4, -2.0, -1.566, -1.4442, -1.0, -0.5, 0, 0.5, 1.0, 1.4442, 1.566, 2.0, 2.4

Table 7.1: η bin boundaries for each lepton channel. Bins are chosen based on the geometry of the muon system and ECAL.

Category	Channel	p_{T} bins [GeV]
Trigger	electron, muon	25, 26.5, 28, 29.5, 31, 32.5, 35, 40, 45, 50, 60, 80, ∞
GSF+ID+Iso	electron	
Standalone	muon	25, 35, 50, ∞
Selection+Iso	muon	

Table 7.2: p_{T} bin boundaries used for each efficiency category. Trigger efficiency includes finer bins at lower p_{T} to capture any trigger turn-on effects. Other categories are relatively stable with respect to p_{T}.

7.2 Fitting Method

Probes are classified into a "pass" and "fail" category for efficiency type being studied. The number of passing and failing $Z \to ll$ events determine the efficiency as shown in Equation 7.3. For simulated samples, which are pure $Z \to \ell\ell$, N_{pass} and N_{fail} can be determined by counting the number of events in each category per (p_{T}, η) bin.

$$\epsilon = \frac{N_{pass}}{N_{pass} + N_{fail}} \tag{7.3}$$

Data may also include background events in addition to the $Z \to \ell\ell$ signal events, particularly the failing probe categories which can have significant contributions from non-resonant backgrounds such as QCD. A fit is performed with the $Z \to \ell\ell$ signal described by the reconstructed M_{ll} distribution from simulation convolved with a Gaussian, and a background described by an analytic function. The choice of analytic function depends on the category of efficiency, and more complicated functions are used to model effects in categories with larger background contributions. The primary background models are:

- **Exponential** (1 free parameter) for categories with relatively low background contribution. Used as background model for all 'pass' categories as well as the

'fail' category for muon selection+isolation+track efficiency.

- **Gaussian Error function** $\times$ **Exponential** $f(x) = erf(b(a-x))e^{c(x-M_Z)}$ (3 free parameters) Used for 'fail' category of electron GSF+Selection efficiency. High p_{T} requirements for tag and probe result in kinematic turn-on in M_{ll} spectrum, which can be described with this model.

- **Quadratic polynomial** (3 free parameters) for muon standalone efficiency. This category has a lower resolution and relatively large background contribution in the failing probe category and cannot be fit with the exponential.

After construction of the signal and background models, the passing and failing categories for a given kinematic bin are simultaneously fit with Equations 7.4 and 7.5 to extract ϵ. Examples of the fit are shown in Figure 7-1.The events in the category of ϵ_{HLT} have negligible background, and ϵ is determined by counting events in the "pass" and "fail" categories.

$$F^{pass}(m_{ll}) = \epsilon \times N_{tot} \times F_{sig}^{pass}(m_{ll}) + N_{bkg}^{pass} \times F_{bkg}^{pass}(m_{ll}) \tag{7.4}$$

$$F^{fail}(m_{ll}) = (1-\epsilon) \times N_{tot} \times F_{sig}^{fail}(m_{ll}) + N_{bkg}^{fail} \times F_{bkg}^{fail}(m_{ll}) \tag{7.5}$$

7.3 Modeling and Systematic Uncertainties

Uncertainties in the efficiency factors is evaluated for sources including signal model choice, background model choice, and tag selection. The variations in the scale factors is propagated to the discriminant distributions used in the final fit.

7.3.1 Evaluating Model Differences

Uncertainties in the scale factors are evaluated as coming from model-dependence of results on the signal and background shapes. These include the FSR model, generator, and background model. Additionally, the impact of the minimum tag selection p_{T} is evaluated. The impact of the model assumptions is evaluated by generating a set of

simulated datasets from the M_{ll} distribution describing the original efficiency model and fitting with the alternative models. The pull, $(\epsilon_{meas} - \epsilon_{true})/\sigma_{meas}$, for each trial is calculated, and the mean pull per p_T-η bin is taken to be the uncertainty due to the alternate model.

Generator Model

aMC@NLO vs. POWHEG: The primary signal simulation for this analysis is generated by MadGraph 5_aMC@NLO interfaced to PYTHIA 8 for parton showering. One of the features of aMC@NLO is that it allows for negative event weights arising from loop diagrams at NLO. Another event generator, POWHEG, disallows this and instead calculates to LO in the kinematic region where negative values would appear. To estimate the kinematic differences between these two approaches, samples with aMC@NLO and POWHEG 2 (both interfaced to PYTHIA 8 for parton showering) are compared. New signal models are created from the POWHEG M_{ll} distributions convolved with a Gaussian.

Final-State Radiation Model

PYTHIA vs. PHOTOS: Final state radiation and higher-order electroweak corrections for the main set of simulations is performed by PYTHIA 8. As described in Chapter 6.2, differences in the order of FSR and electroweak corrections are estimated by comparing PYTHIA and PHOTOS with both interfaced to POWHEG. Post-FSR information from these samples are used to reweight the reconstructed M_{ll} distributions from the primary aMC@NLO +PYTHIA 8 simulation. The reweighted M_{ll} distributions are used to create alternative fitting models.

Background Model

The $Z \to \ell\ell$ events generally provide a clean signature with minimal background, but there can be significant backgrounds from QCD or W+jets primarily appearing in the probes failing the reconstruction and selection categories. In the fits, the backgrounds are modeled with analytic functions as described below.

- **exponential** for all passing categories and muon selection+isolation+track efficiency

- **exponential** $\times$ **erf** for electron GSF ID+Isolation efficiency

- **quadratic polynomial** for muon standalone efficiency failing probes

The alternate set of fitting functions is constructed with:

- **power law** $f(x) \propto x^{-k}, k \geq 0$ for alternative model in all categories. Able to describe the falling M_{ll} spectrum in the low-background categories as well as the

Examples of a muon standalone efficiency fit using the standard quadratic function and the alternative power law model are shown in Figure 7-1.

Tag Selection Uncertainty

Uncertainty due to the selection criteria of the tag lepton are evaluated by directly comparing the impact of efficiency scale factors using the standard cut ($p_{\mathrm{T}} > 25\,\mathrm{GeV}$) to efficiency scale factors derived using tag leptons with $p_{\mathrm{T}} > 30\,\mathrm{GeV}$.

7.3.2 Statistical Uncertainty

Statistical uncertainties in the efficiency scale factor are taken from the average over all variations on the measurement. The statistical uncertainty for a single (p_{T}, η) bin is treated as Poisson, as given in Ref. [107]. Uncertainties for a given (p_{T}, η) bin are correlated across all events containing leptons in the bin, while the uncertainties from separate (p_{T}, η) bins are treated as uncorrelated. Individual categories (reconstruction, identification and isolation, trigger, etc.) are also treated as uncorrelated. The overall impact on the signal yield from the efficiency scale factor statistical uncertainties for the electron and muon channels in $\sqrt{s} = 5.02\,\mathrm{TeV}$ and $\sqrt{s} = 13\,\mathrm{TeV}$ are listed in Table 7.3.

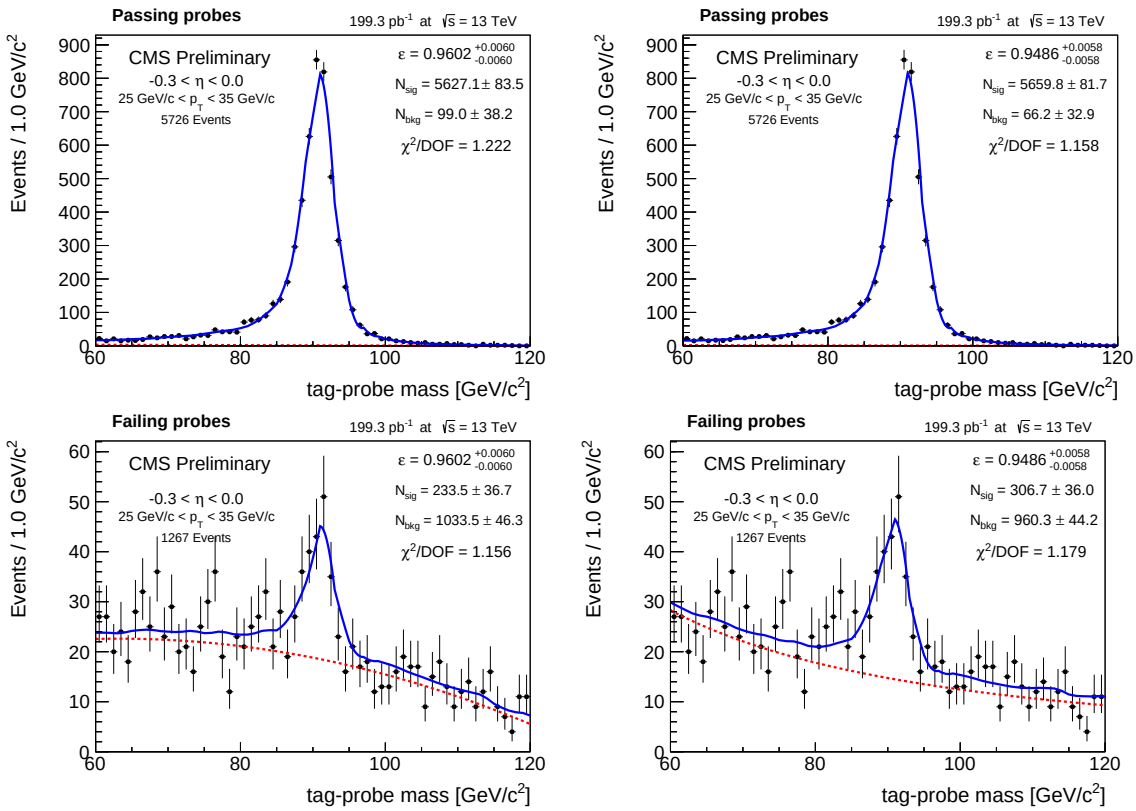

Figure 7-1: Examples of passing (top) and failing (bottom) probes from the same (p_{T}, η) bin in the muon standalone efficiency category. The baseline efficiency value is determined using a fit with a quadratic polynomial background model (left) and uncertainties due to background model choice are evaluated using a fit with a power law background (right).

(13 TeV)	electron [%]	muon [%]
W^+	0.489	0.291
W^-	0.485	0.278
Z	0.498	0.283

(5 TeV)	electron [%]	muon [%]
W^+	0.489	0.245
W^-	0.471	0.231
Z	0.526	0.268

Table 7.3: Statistical uncertainty (as % of total) in the efficiency scale factor calculations on the W^+, W^-, and Z boson acceptance at $\sqrt{s} = 13\,\mathrm{TeV}$ (left) and $\sqrt{s} = 5.02\,\mathrm{TeV}$ (right).

Source	W^+	W^-	W	W^+/W^-	Z	W^+/Z	W^+/Z	W/Z
FSR	0.191	0.169	0.181	0.021	0.238	0.049	0.070	0.058
MC	0.073	0.067	0.070	0.006	0.094	0.023	0.029	0.025
Background	0.007	0.008	0.008	0.000	0.012	0.002	0.002	0.002
Tag pT	0.033	0.038	0.035	0.004	0.093	0.058	0.054	0.056
Statistical	0.286	0.278	0.202	0.009	0.279	0.008	0.001	0.076
Total [%]	0.35	0.33	0.28	0.00	0.39	0.07	0.08	0.10

Table 7.4: Uncertainties on the lepton efficiency scale factors for the muon channel in 13 TeV

Source	W^+	W^-	W	W^+/W^-	Z	W^+/Z	W^+/Z	W/Z
FSR	0.081	0.080	0.081	0.001	0.166	0.087	0.089	0.085
MC	0.057	0.057	0.056	0.000	0.093	0.038	0.038	0.036
Background	0.056	0.053	0.055	0.004	0.099	0.041	0.044	0.045
Tag pT	0.016	0.018	0.017	0.001	0.047	0.066	0.067	0.063
Statistical	0.489	0.486	0.349	0.001	0.488	0.002	0.003	0.137
Total [%]	0.50	0.50	0.36	0.00	0.53	0.11	0.11	0.18

Table 7.5: Uncertainties on the lepton efficiency scale factors for the electron channel in 13 TeV

Source	W^+	W^-	W	W^+/W^-	Z	W^+/Z	W^+/Z	W/Z
MC	0.09	0.08	0.09	0.00	0.15	0.07	0.07	0.07
FSR	0.17	0.15	0.32	0.01	0.27	0.23	0.26	0.24
Bkg Model	0.01	0.01	0.01	0.01	0.00	0.01	0.01	0.01
Tag pT	0.48	0.49	0.48	0.01	0.88	0.45	0.45	0.45
stat	0.25	0.24	0.20	0.32	0.26	0.38	0.36	0.35
Total [%]	0.56	0.56	0.61	0.32	0.96	0.62	0.62	0.61

Table 7.6: Summary of the propagated muon efficiency systematic uncertainties at 5 TeV.

Source	W^+	W^-	W	W^+/W^-	Z	W^+/Z	W^+/Z	W/Z
MC	0.00	0.00	0.00	0.00	0.02	0.00	0.00	0.00
FSR	0.01	0.01	0.01	0.00	0.13	0.15	0.15	0.15
Bkg Model	0.00	0.00	0.00	0.00	0.00	0.00	0.00	0.00
Tag pT	0.02	0.02	0.02	0.01	0.06	0.03	0.04	0.04
stat	0.50	0.49	0.44	0.67	0.51	0.75	0.74	0.72
Total [%]	0.50	0.49	0.44	0.66	0.52	0.76	0.75	0.73

Table 7.7: Summary of the propagated electron efficiency systematic uncertainties at 5 TeV.

7.4 Results

Tables listing the scale factors for each category and (p_{T}, η) bin and figures comparing the efficiencies in data and simulation are provided in Appendix A.

Chapter 8

Other Corrections

8.1 Lepton Momentum Corrections

Reconstructed lepton momenta require additional corrections in data and simulation to ensure agreement of observable distributions. Several sources which are not fully modeled in the simulation, such as detector alignment, reconstruction software, and magnetic field uncertainty are encompassed by these additional corrections. These effects generally apply to both muons and electrons, but the magnitude of the overall correction is much smaller for muons. Scale factors align the maximum of the $Z \to \ell\ell$ M_{ll} distribution observed in data to the expected value, while the resolution of lepton momentum reconstruction in simulation is corrected to match data.

8.1.1 Electron Energy Scale and Resolution

Electron energy is corrected at the ECAL cluster energy level. Corrections are derived for separate categories of observables such as η, and E_{T}, with data further separated by run number. The scale factors for the data correction are derived by fitting a Breit-Wigner function [108] convolved with a Crystal-Ball function [109,110] to the dilepton invariant mass distribution for $Z \to ee$ events. The scale factor is the difference between the expected dilepton mass and the maximum determined by this fit. Smearing factors are likewise determined by using the simulated Z boson invariant mass dis-

tribution as a probability density function in a maximum likelihood fit, and using the residual to derive a correction factor. Applying this with a Gaussian smearing is sufficient to describe the data for all categories [111]. Systematic uncertainties related to the energy scale and resolution corrections are computed as the difference between locations of the maximum of the $Z \to ee$ M_{ll} distribution from varying electron categorization. Scale and resolution corrections are derived using the method described above, from $Z \to ee$ simulation and the 2017H ($\sqrt{s} = 13\,\text{TeV}$) single electron trigger dataset. Due to changing detector conditions and calibration, scale corrections are dependent on run number. Scale corrections for the 2017G ($\sqrt{s} = 5.02\,\text{TeV}$) dataset are based on the 2017H Run Number 306936. As these data were taken nearly consecutively, the LHC and detector conditions are sufficiently similar to produce adequate results for events from all categories considered. The M_{ll} distributions before and after applying electron energy scale corrections are shown in Figure 8-1 (Figure 8-2) for $\sqrt{s} = 13\,\text{TeV}$ ($\sqrt{s} = 5.02\,\text{TeV}$).

8.1.2 Muon Momentum Corrections

As with electrons, muon momentum measurements include the need for corrections, though the effect is much smaller than for electrons. Corrections are derived from average lepton p_T and $Z \to \mu\mu$ invariant mass distribution, so that the maximum and width of the $Z \to \mu\mu$ invariant mass in simulation matches data [112]. A single set of corrections is used for the entirety of 2017 data-taking. Distributions of $Z \to \mu\mu$ M_{ll} before and after applying muon momentum corrections are shown in Figure 8-3 (Figure 8-4) for $\sqrt{s} = 5.02\,\text{TeV}$ ($\sqrt{s} = 13\,\text{TeV}$).

8.2 ECAL L1 Trigger Prefiring

Radiation damage to the $PbWO_4$ crystals in the ECAL result in color centers forming within the crystal lattice, reducing transparency and altering light propagation through the crystal. Corrections to account for this effect were light transmission were not applied in a way which completely removed the timing drift. Trigger primitives

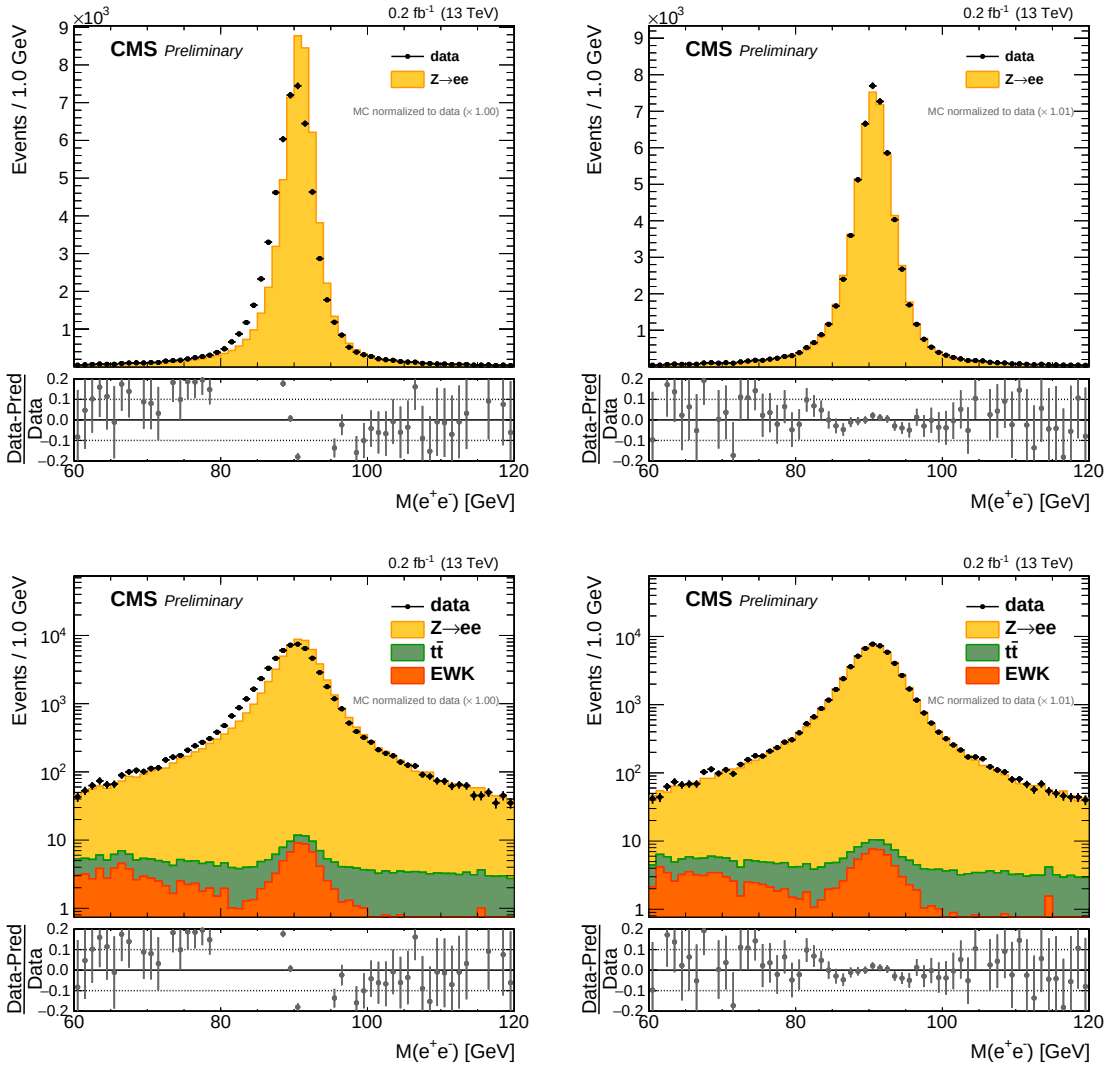

Figure 8-1: $Z \to ee$ dilepton mass spectrum at $\sqrt{s} = 13\,\text{TeV}$, with (right) and without (left) electron energy scale and resolution corrections.

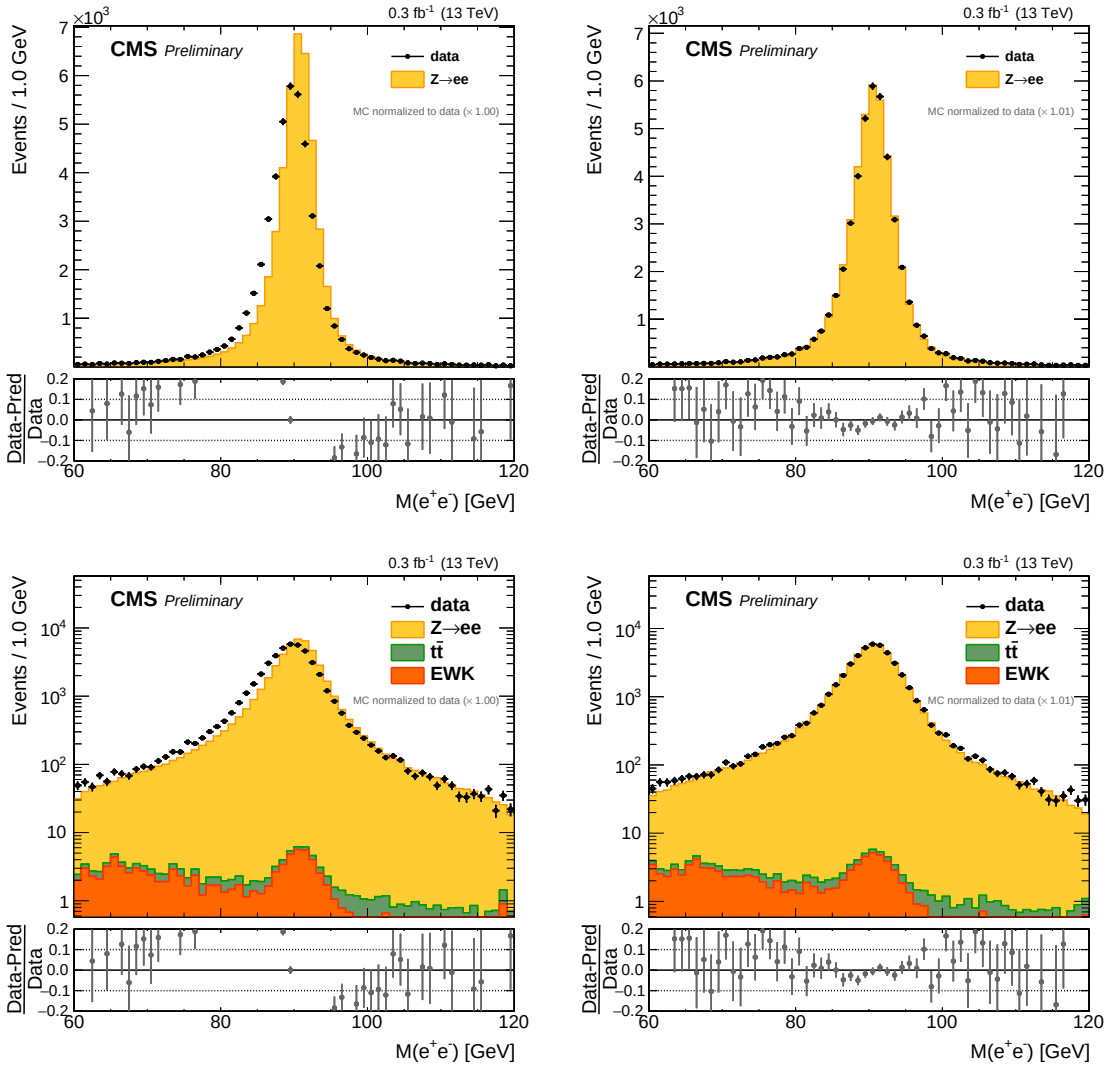

Figure 8-2: $Z \to ee$ dilepton mass spectrum at $\sqrt{s} = 5.02\,\text{TeV}$, with (right) and without (left) electron energy scale and resolution corrections.

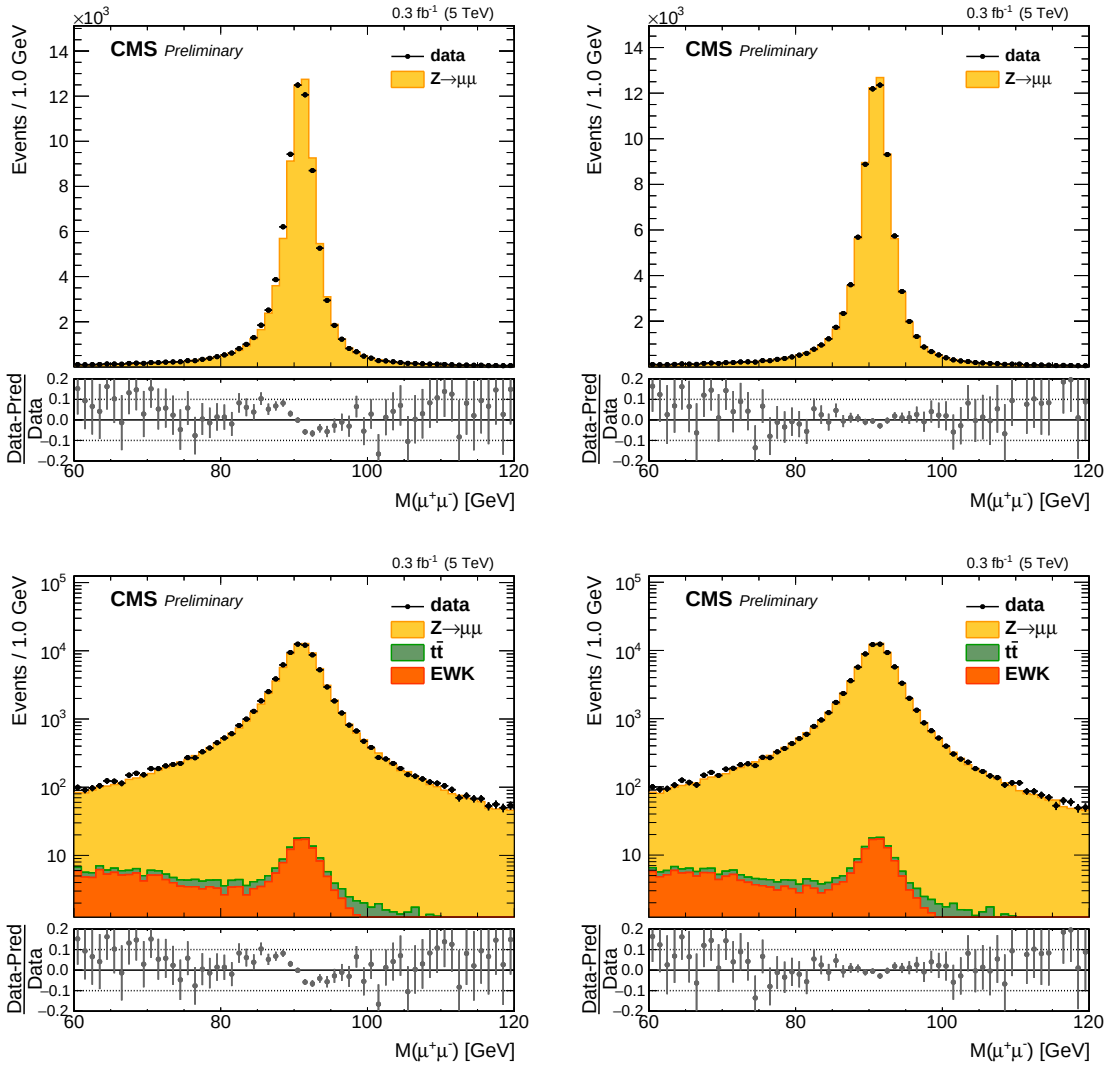

Figure 8-3: $Z \to \mu\mu$ dilepton mass spectrum at $\sqrt{s} = 5.02\,\text{TeV}$, with (right) and without (left) muon momentum corrections.

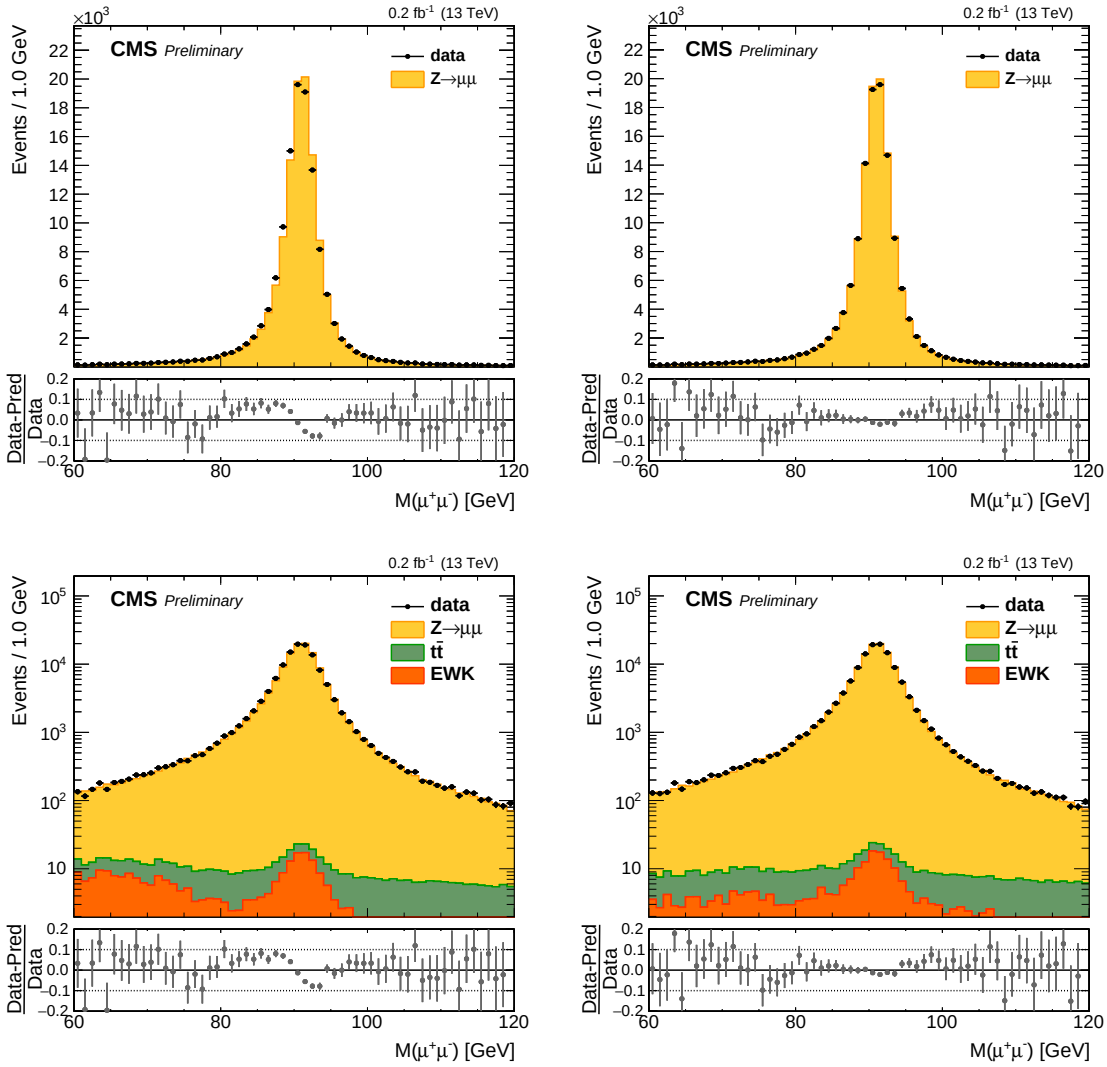

Figure 8-4: $Z \to \mu\mu$ dilepton mass spectrum at $\sqrt{s} = 13\,\text{TeV}$, with (right) and without (left) muon momentum corrections.

(TPs) in the forward regions of ECAL, $2.0 < |\eta| < 3.0$, were affected by the timing drift during the 2017 data-taking period. TPs in the forward ECAL region could be incorrectly associated with the prior bunch crossing, an effect described as "prefiring". The global trigger rules disallow the collection of consecutive bunch crossings, and no more than one event accepted per three consecutive bunch crossings. Therefore events susceptible to prefiring will be discarded by the trigger while the prior event will be read out. The prefiring effect is not described in simulation, and rates of prefiring due to large ECAL deposits are studied for jets and photons. Prefiring efficiency scale factors are calculated for an event based on the kinematics of the photons and jets, as described in Equation 8.1.

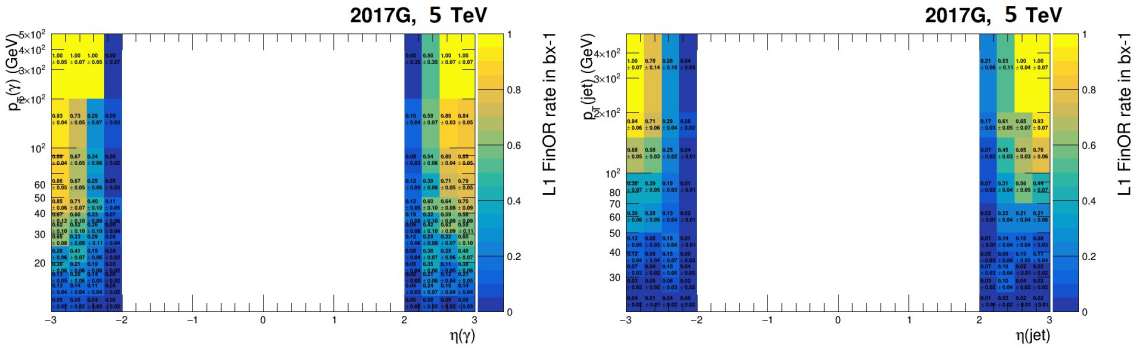

Figure 8-5: Pre-firing probability maps for photons (left) and jets (right) for 2017G ($\sqrt{s} = 5.02\,\text{TeV}$). The $z-$axis represents the probability of an object with (p_T, η) causing pre-firing. Objects with higher p_T and $|\eta| \sim 3$ are more likely to cause pre-firing. Objects with $|\eta| < 2$ do not cause pre-firing.

$$\epsilon_{pref} = 1 - P(\text{prefire}) = \prod_{i=\gamma,jets} (1 - \epsilon_i^{pref}(\eta, p_T)) \tag{8.1}$$

In cases where a photon and jet overlap (with $\Delta R < 0.4$), $\epsilon_i = \max(\epsilon_\gamma, \epsilon_{jet})$. Prefiring rates by (p_T, η) for jets and photons are shown in Figure 8-5 for 2017G ($\sqrt{s} = 5.02\,\text{TeV}$) and Figure 8-6 for 2017H ($\sqrt{s} = 13\,\text{TeV}$). These are derived from a tag-and-probe method using the trigger rules to select a set of "un-prefireable" events as a reference value. Per-event prefiring efficiency scale factors are applied to all simulated samples. Correction factors on the $W^\pm$ and Z boson yields are listed in Table 8.1 for

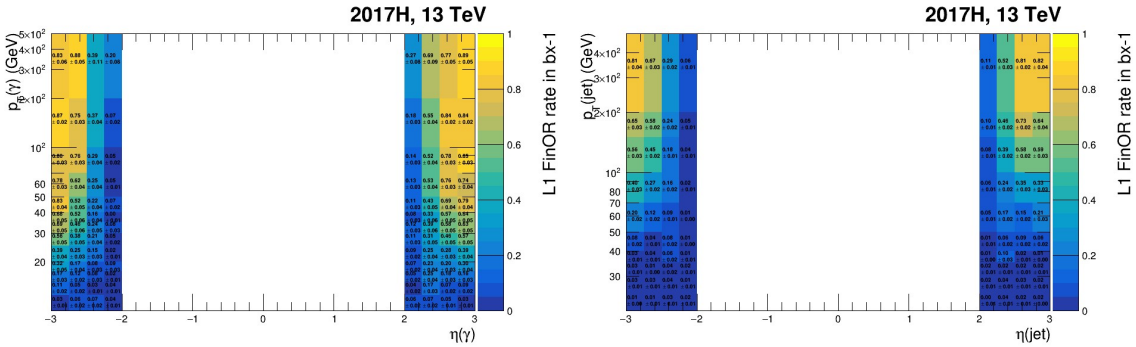

Figure 8-6: Pre-firing probability maps for photons (left) and jets (right) for 2017H ($\sqrt{s} = 13\,\text{TeV}$). The $z-$axis represents the probability of an object with (p_T, η) causing pre-firing. Objects with higher p_T and $|\eta| \sim 3$ are more likely to cause pre-firing. Objects with $|\eta| < 2$ do not cause pre-firing.

2017G ($\sqrt{s} = 5.02\,\text{TeV}$) and Table 8.2 for 2017H ($\sqrt{s} = 13\,\text{TeV}$). Uncertainties in the prefiring rate per object are taken to be the maximum of the statistical uncertainty or 20% of the prefiring rate for the particular (p_T, η) bin. The effect of prefiring on the $Z \to ee$ rapidity distribution for 2017G (2017H) is shown in Figure 8-7 (Figure 8-8). These figures also demonstrate the effectiveness of the corrections at mitigating the effects of prefiring on forward events.

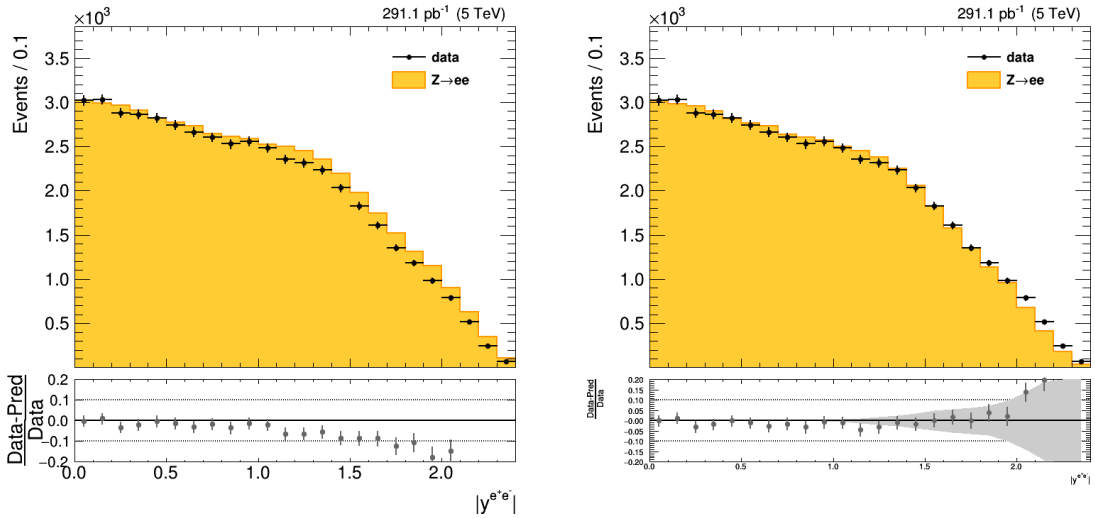

Figure 8-7: $Z \to ee$ rapidity before (left) and after (right) pre-firing corrections, 2017G ($\sqrt{s} = 5.02\,\text{TeV}$). Uncertainty (gray) shows $\pm 1\sigma$ deviation from central value of prefiring efficiency per event.

Process	Jets	Photons	Total
$W \to e^+\nu$	0.990	0.977	0.975
$W \to e^-\nu$	0.990	0.978	0.976
$Z \to ee$	0.986	0.961	0.959
$W \to \mu^+\nu$	0.989	0.998	0.988
$W \to \mu^-\nu$	0.989	0.999	0.989
$Z \to \mu\mu$	0.985	0.999	0.985

Table 8.1: Impact of prefiring on the reconstruction efficiency of each of the W^+, W^-, and Z boson channels for the $\sqrt{s} = 5.02\,\text{TeV}$ (2017G) dataset. Corrections are applied differentially and table reports total efficiency integrated over full phase space. The "Total" column includes proper counting of overlapping objects and is the total efficiency scale factor due to pre-firing.

Process	Jets	Photons	Total
$W \to e^+\nu$	0.989	0.970	0.967
$W \to e^-\nu$	0.990	0.974	0.971
$Z \to ee$	0.988	0.964	0.962
$W \to \mu^+\nu$	0.990	0.996	0.988
$W \to \mu^-\nu$	0.991	0.997	0.989
$Z \to \mu\mu$	0.989	0.997	0.987

Table 8.2: Impact of prefiring on the reconstruction efficiency of each of the W^+, W^-, and Z boson channels for the $\sqrt{s} = 13\,\text{TeV}$ (2017H) dataset. Corrections are applied differentially and table reports total efficiency integrated over full phase space. The "Total" column includes proper counting of overlapping objects and is the total efficiency scale factor due to pre-firing.

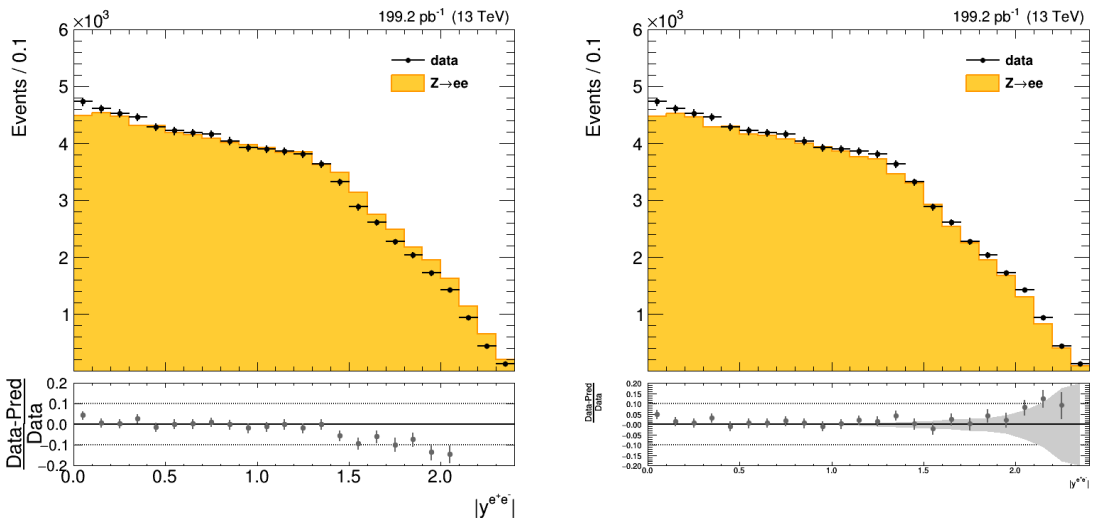

Figure 8-8: $Z \to ee$ rapidity before (left) and after (right) pre-firing corrections, 2017H ($\sqrt{s} = 13\,\text{TeV}$). Uncertainty (gray) shows $\pm 1\sigma$ deviation from central value of prefiring efficiency per event.

8.3 Charge misidentification

In electrons, charge determination in event reconstruction can be affected by bremsstrahlung photons converting to electron-positron pairs close to the original electron track. This can potentially cause the GSF track reconstruction to incorporate additional information which results in the incorrect charge being assigned to the reconstructed electron. The rate at which this occurs can be determined from the number of events in a $Z \to e^+e^-$ sample where the e^+e^- pairs are reconstructed with charges of opposite-sign (OS) or same-sign (SS). Cases where both or neither charge is reconstructed properly result in an OS event, while one correct and one incorrect charge assignment result in a SS event. Given a charge misidentification rate of f_{misID} and a total number of $Z \to ee$ events $N_Z = N_{OS} + N_{SS}$, the number of expected OS events (N_{OS}) and SS events (N_{SS}) is described in Equation 8.2.

$$\begin{aligned} N_{OS} &= (1 - f_{\text{misID}})^2 \times N_Z + f_{\text{misID}}^2 \times N_Z \\ N_{SS} &= 2 \times f_{\text{misID}}(1 - f_{\text{misID}}) \times N_Z \end{aligned} \tag{8.2}$$

Given that the rate of charge misidentification is generally very small ($f_{\text{misID}} << 1$), the quadratic terms can be dropped and these are approximated by:

$$\begin{aligned} N_{OS} &= (1 - 2 \times f_{\text{misID}}) \times N_Z \\ N_{SS} &= 2 \times f_{\text{misID}} \times N_Z \end{aligned} \tag{8.3}$$

From Equation 8.3, the misidentication rate f_{misID} can determined from the rate of observed SS events:

$$f_{\text{misID}} = \frac{N_{SS}}{2 \times (N_{SS} + N_{OS})} \tag{8.4}$$

The misidentification rate is calculated for both data and simulation, with separate categories for barrel and endcap regions, and the difference between the rates in data and simulation is used as the f_{misID} in Equation 8.5. As shown in Equation 8.5, the number of W^+ and W^- bosons N_i ($i = W^+, W^-$) produced can be estimated from the number of selected W^+ and W^- bosons N_i^{sel} ($i = W^+, W^-$) and f_{misID}. The systematic uncertainty on each channel due to the charge misidentification is taken as the difference between the N_i and N_i^{sel}. The uncertainty on the Z boson yield can be similarly determined from the SS and OS yields. The uncertainties are summarized in Table 8.3 for the $\sqrt{s} = 5.02\,\text{TeV}$ and $\sqrt{s} = 13\,\text{TeV}$ electron channels. Studies on cosmic muons show that there is a negligible effect on muons.

$$\begin{aligned} N_{W^+} &= N_{W^+}^{sel} \times (1 - f_{\text{misID}}) + N_{W^-}^{sel} \times f_{\text{misID}} \\ N_{W^-} &= N_{W^+}^{sel} \times f_{\text{misID}} + N_{W^-}^{sel} \times (1 - f_{\text{misID}}) \end{aligned} \tag{8.5}$$

Source	W^+	W^-	W	W^+/W^-	Z	W^+/Z	W^-/Z	W/Z
13 TeV [%]	0.068	0.087	-	0.018	0.205	0.136	0.118	0.205
5 TeV [%]	0.060	0.079	-	0.018	0.179	0.118	0.100	0.179

Table 8.3: Uncertainty as a percentage of signal yield due to electron charge misidentification at $\sqrt{s} = 5.02\,\text{TeV}$ and $\sqrt{s} = 13\,\text{TeV}$.

Chapter 9

Hadronic Recoil Corrections

Missing transverse energy spectra of the W and Z boson signal simulation does not fully describe the observed distributions in data. This is attributable to multiple effects, such as mis-modeling of multiple scattering and detector simulation, or imperfect detector calibration in data. Therefore, the simulated E_{T}^{miss} distribution is not able to describe the observed E_{T}^{miss} distribution to sufficient precision necessary for this measurement. In order to compensate for this, $Z \to \mu\mu$ events in data and simulation are used to produce corrections to the hadronic recoil. These corrections are used to match the E_{T}^{miss} resolution and response in simulated W and Z boson events to that of data.

The W and Z boson share a similar production mechanism and are similar in mass, so data corrections derived from $Z \to \mu\mu$. The hadronic recoil of each event is corrected, and the E_{T}^{miss} is recomputed based on these corrected values.

The hadronic recoil is characterized as the negative vector sum of the E_{T}^{miss} and the p_{T} of the daughter leptons from the W or Z boson, as shown in Equation 9.1. This is effectively everything "else" in the event except for the W boson and daughter leptons.

$$\vec{U} = -(\vec{E_T^{miss}} + \sum p_T^l) \tag{9.1}$$

The recoil is split into two components: the projection parallel to the boson momentum, $u_{||}$, and perpendicular to the boson momentum, $u_{\perp}$, as shown in Equa-

tions 9.2 and 9.3.

$$u_{||} = ||\vec{U} \cdot \vec{Z_{p_T}}|| \tag{9.2}$$

$$u_{\perp} = ||\vec{U} - u_{||}|| \tag{9.3}$$

The $u_{||}$ and $u_{\perp}$ observables are both the source and target of the recoil corrections. The method by which these distributions are parametrized and corrected are described in the following sections.

9.1 Recoil Modeling

The recoil corrections provide a transformation from the simulated recoil distributions into a data-like distribution. The transformation is created from the difference in recoil distributions in $Z \to \ell\ell$ samples from simulation and data. Recoil distributions in simulated W boson events are corrected by the difference between data and simulated $Z \to \ell\ell$ recoil.

9.2 Parametrization Derivation

Recoil is parametrized in general the same way for each of the samples:

1. $u_{||}$ and $u_{\perp}$ are binned by boson p_{T}
2. $u_{||}$ and $u_{\perp}$ in each p_{T} bin are fit with a double-Gaussian function

Figures 9-1 and 9-2 provide examples of these double-Gaussian fits in data and simulation. Recoil parametrization is done in data for $Z \to \mu\mu$ and simulation for $Z \to \mu\mu$ and $W \to \mu\nu$. The p_{T} of the Z bosons is determined by the reconstructed dilepton p_{T}. For W bosons, the p_{T} is taken directly from the generator-level information in the simulation. The parametrization of the recoil in the W boson sample is further separated by charge, to be applied separately to W^+ and W^-. Additionally, fits for $u_{||}$ and $u_{\perp}$ in Z data include the simulated dilepton background contributions from electroweak and $t\bar{t}$ sources.

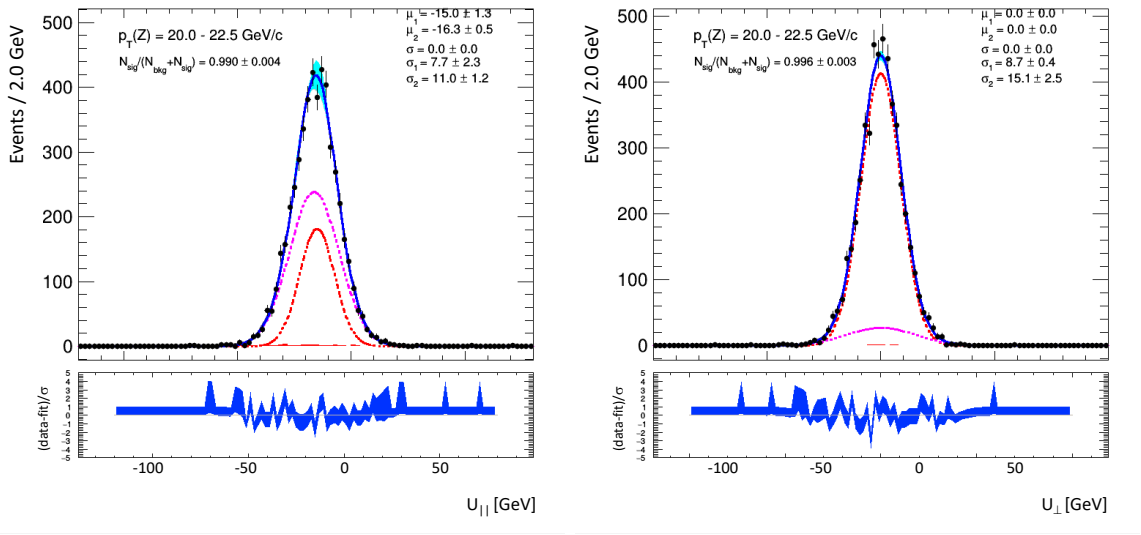

Figure 9-1: Examples of the recoil parametrization fits for $u_{||}$ (left) and $u_{\perp}$ (right) in data for 20 GeV $< m_{\mu\mu} <$ 22.5 GeV. The two Gaussians are shown, with their sum in blue.

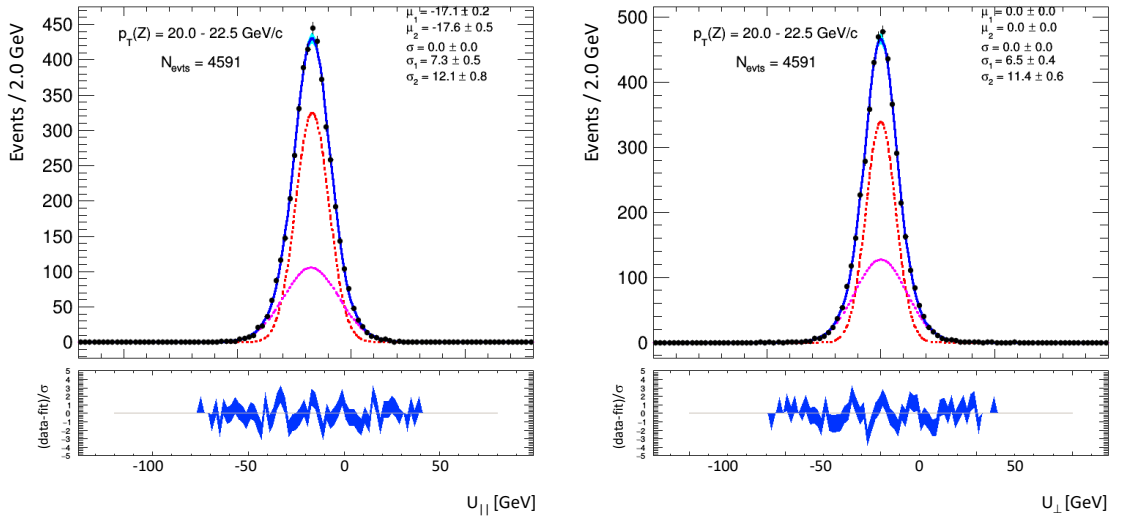

Figure 9-2: Examples of the recoil parametrization fits for $u_{||}$ (left) and $u_{\perp}$ (right) in MC for 20 GeV $< m_{\mu\mu} <$ 22.5 GeV. The two Gaussians are shown, with their sum in blue.

9.3 Application of Corrections

The corrections derived in the previous section can be applied to the W or Z Monte Carlo. For simulated W or Z event, the original $u_{||}$ and $u_{\perp}$ are replaced by a corrected value and the E_{T}^{miss} is recomputed.

Correcting Recoil

Using the same boson p_{T} definition that was used to create the parametrization, the recoil distributions in simulated W and Z bosons are corrected in the following manner:

1. Each fit result is integrated to create a cumulative distribution function (CDF)
2. A p-value is determined by evaluating the CDF of the W boson simulation: $p_i = F_{U_i}^{M}(u_i)$
3. u_i^M value is determined by finding the root of the CDF from simulated Z bosons at p: $u_i^M = F_{U_i}^{Data^{-1}}(p_i)$
4. u_i^{Data} value is determined by finding the root of the CDF from Z bosons in data at p: $u_i^{Data} = F_{U_i}^{Data^{-1}}(p_i)$
5. The original recoil value is shifted by the difference between the Z boson recoil in data (u_i^D) and simulation (u_i^M): $u_i' = u_i + (u_i^D - u_i^M)$
6. $u_{||}'$ and $u_{\perp}'$ are used to compute a new MET value for the event

When applying recoil corrections to $Z \to \ell\ell$ events, the first step is based off the Z boson simulation and the steps effectively reduce to replacing the u_i components with the result of step 4.

Validation

The effect of the recoil corrections on the $Z \to \mu\mu$ E_{T}^{miss} and recoil distributions is shown in Figures 9-3 and 9-4. Closure of the recoil corrections is performed by

comparing the mean and width of the recoil distributions of $Z \to \ell\ell$ events in data, simulated $Z \to \ell\ell$ without corrections, and $Z \to \ell\ell$ with corrections. These are shown in Figure 9-5 [13 TeV] and Figure 9-6 [5 TeV].

9.4 Uncertainties

The parametrization method described above implicitly makes the assumption that the recoil distribution can uniformly be described by a double-Gaussian over the entire p_{T} range as well as the assumption that the parametrization can be treated as one inclusive rapidity region. Alternative models are used to address the systematic uncertainty due to these assumptions.

The impact of these uncertainties is accounted for by propagating the differences in E_{T}^{miss} through m_{T} to as uncertainties on the W boson signal fit as described in the following chapter. Additionally, statistical uncertainties for each of the fit parameters is propagated to the final result in the same way. The details of how each of the uncertainties is modeled is calculated is listed below.

1. **Binning**: The baseline rapidity (y) binning is a single inclusive bin. An alternative using three y bins ($|y| < 0.5$, $0.5 < |y| < 1.0$, and $|y| < 1.0$) is fit with the double-Gaussian function.

2. **Model**: The baseline fit model is a double-Gaussian. A Gaussian kernel is used as an alternative.

3. **Statistical uncertainty**: One additional correction set per free parameter is created to estimate the impact of statistical uncertainty in the fit results on the E_{T}^{miss} modeling. There are a total of 10 correction sets, 6 for $u_{||}$ and 4 for $u_{\perp}$ (two Gaussians with μ, σ, and normalization, $u_{\perp}$ has $\mu = 0$ fixed for both Gaussians). Principal component analysis of each fit result is used to create the variation correction sets by diagonalizing the covariance matrix and varying one eigenvalue by $\pm 1\sigma$ and creating a new function from the altered covariance matrix.

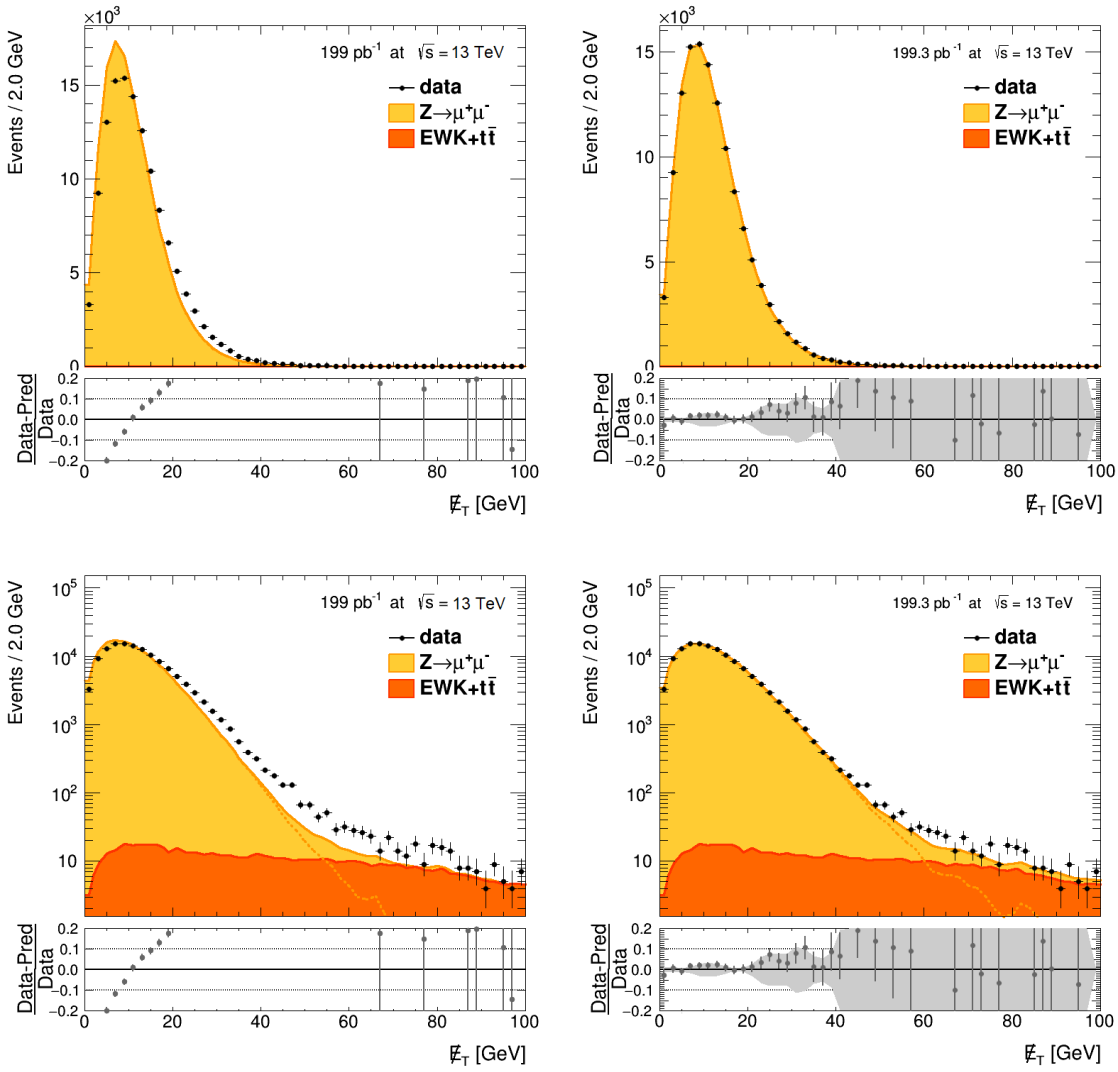

Figure 9-3: E_{T}^{miss} spectrum for $Z \to \mu\mu$ sample, without (left) and including (right) recoil corrections on linear (top) and log-y (bottom) scales. Gray band on recoil-corrected figures shows total uncertainty from modeling and statistical sources.

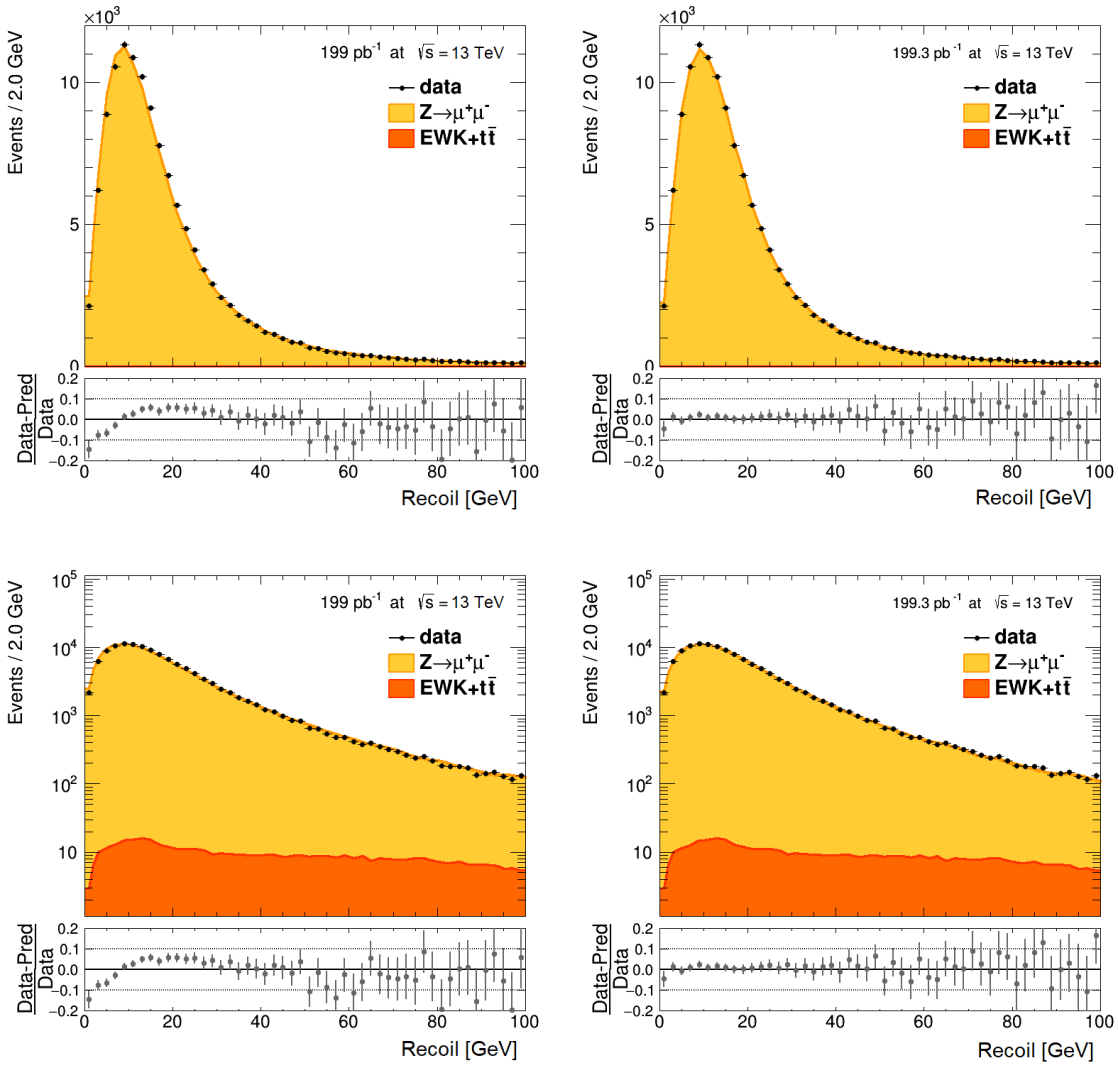

Figure 9-4: Recoil spectrum for $Z \to \mu\mu$ sample, without (left) and including (right) recoil corrections on linear (top) and log-y (bottom) scales.

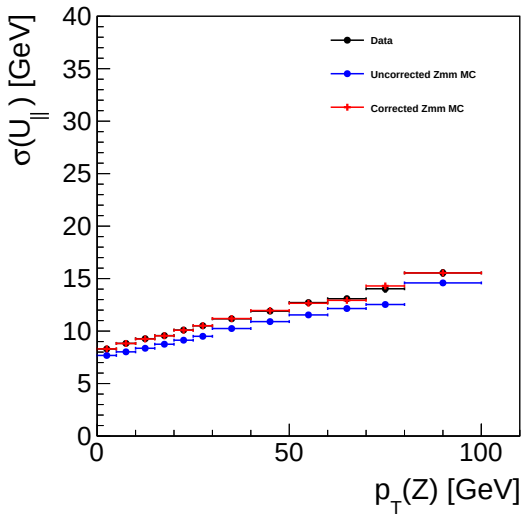

(a) Resolution of $u_{||}$

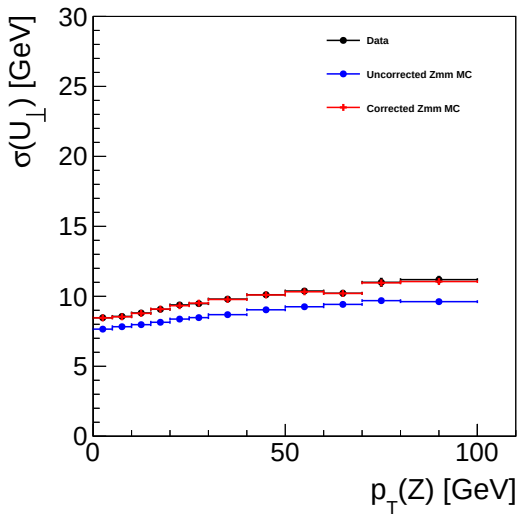

(b) Resolution of $u_{\perp}$

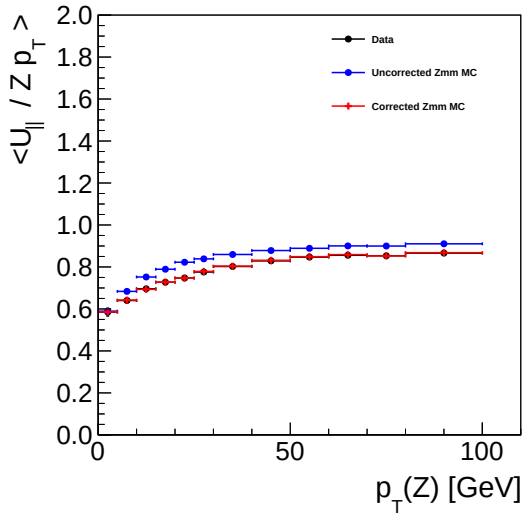

(c) p_T-corrected response of $u_{||}$

Figure 9-5: Closure of the recoil corrections derived from and applied to $Z \to \mu\mu$ samples for the 13 TeV dataset. The raw recoil distribution in Monte Carlo (blue) is corrected (red) towards the target spectrum of data (black).

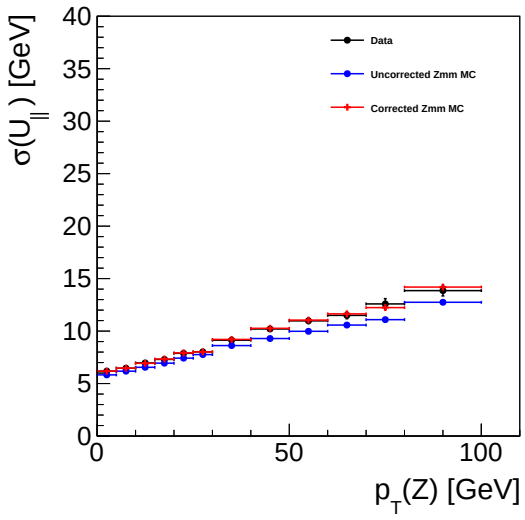

(a) Resolution of $u_{||}$

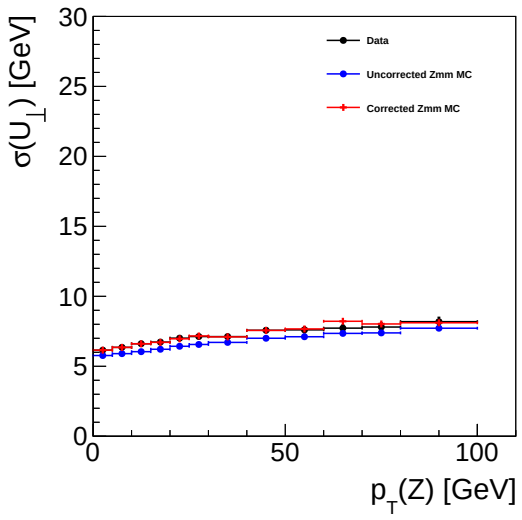

(b) Resolution of $u_{\perp}$

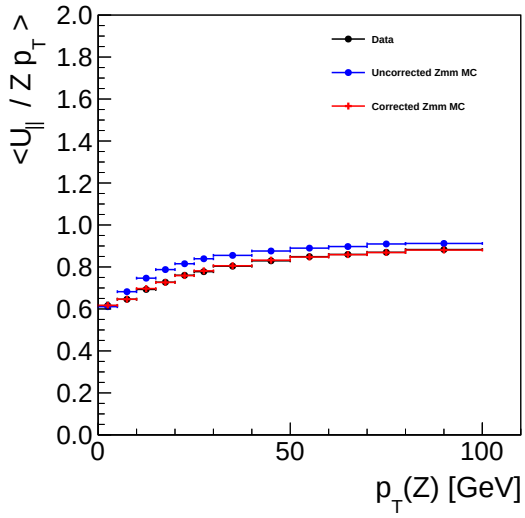

(c) p_T-corrected response of $u_{||}$

Figure 9-6: Closure of the recoil corrections derived from and applied to $Z \to \mu\mu$ samples for the 5 TeV dataset. The raw recoil distribution in Monte Carlo (blue) is corrected (red) towards the target spectrum of data (black).

Each of these uncertainty models produces an alternate set of recoil corrections. These are applied as described in Section 9.3. The difference in E_{T}^{miss} from each of the listed configurations is incorporated as an uncertainty on the W boson signal m_{T} distribution in the W signal extraction fit.

Chapter 10

Signal Extraction

10.1 Fit Model

The cross sections of the $W^{\pm}$ and Z bosons are determined by a simultaneous fit of W^+, W^-, and Z boson channels. Modeled observable distributions of W^+, W^-, and Z boson signals and associated backgrounds are fit to their respective observable distribution in data. The discriminant for the W^+ and W^- bosons is the transverse mass (m_{T}) observable, and for Z bosons is the dilepton invariant mass M_{ll}. Equation 10.1 shows the definition of m_{T}.

$$m_{\mathrm{T}} = \sqrt{2p_{\mathrm{T}}^{\ell} E_{\mathrm{T}}^{miss}(1 - \cos[\Delta\phi(\vec{\ell}, E_{\mathrm{T}}^{miss})])} \tag{10.1}$$

The M_{ll} and m_{T} distributions for the W^+, W^-, and Z boson signal processes as well as their backgrounds are modeled as described in the following section. The full fit model consists of the W^+, W^-, and Z boson signal models, the diboson background, the $t\bar{t}$ background, the Drell-Yan background, and the W+jets background. The W^+ and W^- boson channels also include a QCD background. All signal and background models include the appropriate correction, which affect the discriminant distribution and overall normalizations. Detailed descriptions of the background processes and modeling are provided in the next section, the remainder of this section describes how these are incorporated into the fit.

Normalizations

Signal process normalizations are independent across channels. Within a given channel, the signal process and background process from the same production mechanism (i.e. $W \to \mu\nu$ and $W \to \tau\nu$) have their rates fixed relative to each other. The $t\bar{t}$ normalizations and diboson normalizations are fully correlated across the W^+, W^-, and Z boson channels. Uncertainties in the normalizations of each of these processes is set to 10%. The Drell-Yan background normalization is correlated between the W^+ and W^- boson channels, with a normalization uncertainty of 3%. QCD background normalization in the W^+ and W^- boson channels are independent and unconstrained.

Shape Uncertainties

Uncertainties in observables which impact the final discriminant distribution are included as shape uncertainties. Prefiring correction uncertainties are fully correlated for all simulated processes in the W^+, W^-, and Z boson channels. Each uncertainty source from the lepton efficiency scale factors is also correlated over all simulated processes in all channels. Each uncertainty due to recoil/E_{T}^{miss} modeling is fully correlated across the W boson signal and W and Z boson background processes in the W^+ and W^- boson channels. The QCD-multijet background uncertainty is correlated between the W^+ and W^- channels.

10.2 Signal Modeling

The Z boson and W^+ and W^- boson signal processes are described by simulation, and include several corrections to improve simulated descriptions of effects seen in data. Lepton momentum scale corrections (Chapter 8), lepton reconstruction and identification efficiency scale factors (Chapter 7), and prefiring corrections (Chapter 8.2) are applied for all of the W^+, W^-, and Z boson processes. The W^+ and W^- boson processes additionally include E_{T}^{miss} corrections, which are described in Chapter 9. Disriminants—M_{ll} for the Z boson and m_{T} for the W^+ and W^- bosons—are calculated after all corrections to kinematic observables have been applied, and

appropriate event weighting is included when constructing the distributions.

10.3 Background Modeling

Backgrounds are estimated from both simulation and data-driven sources. Simulated backgrounds include the $t\bar{t}$ and various electroweak processes, and include the appropriate normalization factors for prefiring and efficiency. Backgrounds to W and Z boson can include $t\bar{t}$ and diboson (WW, WZ, ZZ) processes contributing one or two isolated leptons, respectively. The DY background to the W is from a $Z \to \mu\mu$ or $Z \to ee$ decay with only one lepton being in the detector volume, or the $Z \to \tau\tau$ with one of the τ decaying leptonically. $Z \to \tau\tau$ with leptonic τ decays is also a background to the Z. The $W \to \tau\nu$, with leptonic τ decay also contributes to the W backgrounds. For all of these simulated background processes, lepton efficiency scale factors, lepton momentum scale corrections, and prefiring corrections are applied when producing the m_{T} and M_{ll} distributions. Additionally, the $W \to \tau\nu$ and Drell-Yan background processes in the W^+ and W^- boson channels include E_{T}^{miss} corrections.

QCD Background

The largest background of the W is from QCD multijet background. The primary contributions are heavy-flavor decays and γ+jets with photon conversion to electrons. There are no reliable simulations available to describe this process, therefore the QCD m_{T} distribution is estimated from data. This background region is composed of events passing the standard lepton identification and event selection requirements, with the relative isolation criteria inverted. Contributions from electroweak processes are subtracted. The shape of the QCD m_{T} distribution in the non-isolated lepton control region is assumed to be the same as in the signal region. Multiple isolation regions are considered when constructing the QCD background contribution. Three regions, $0.15 < I < 0.30$, $0.30 < I < 0.45$, and $0.45 < I < 0.55$ are considered. These are shown in Figure 10-1, and the m_{T} distribution is found to be generally

independent of isolation region. Due to the high W boson signal contamination (about 30%), the $0.15 < I < 0.30$ region is not considered when constructing the QCD m_{T} distribution. The primary QCD m_{T} distribution is taken from the $0.30 < I < 0.45$ region, which has around 5% W boson signal contamination. An uncertainty in the QCD estimation is taken from the relative difference between the m_{T} shapes in the $0.30 < I < 0.45$ and $0.45 < I < 0.55$ regions. The uncertainty shapes are constructed from a symmetrization around the central value.

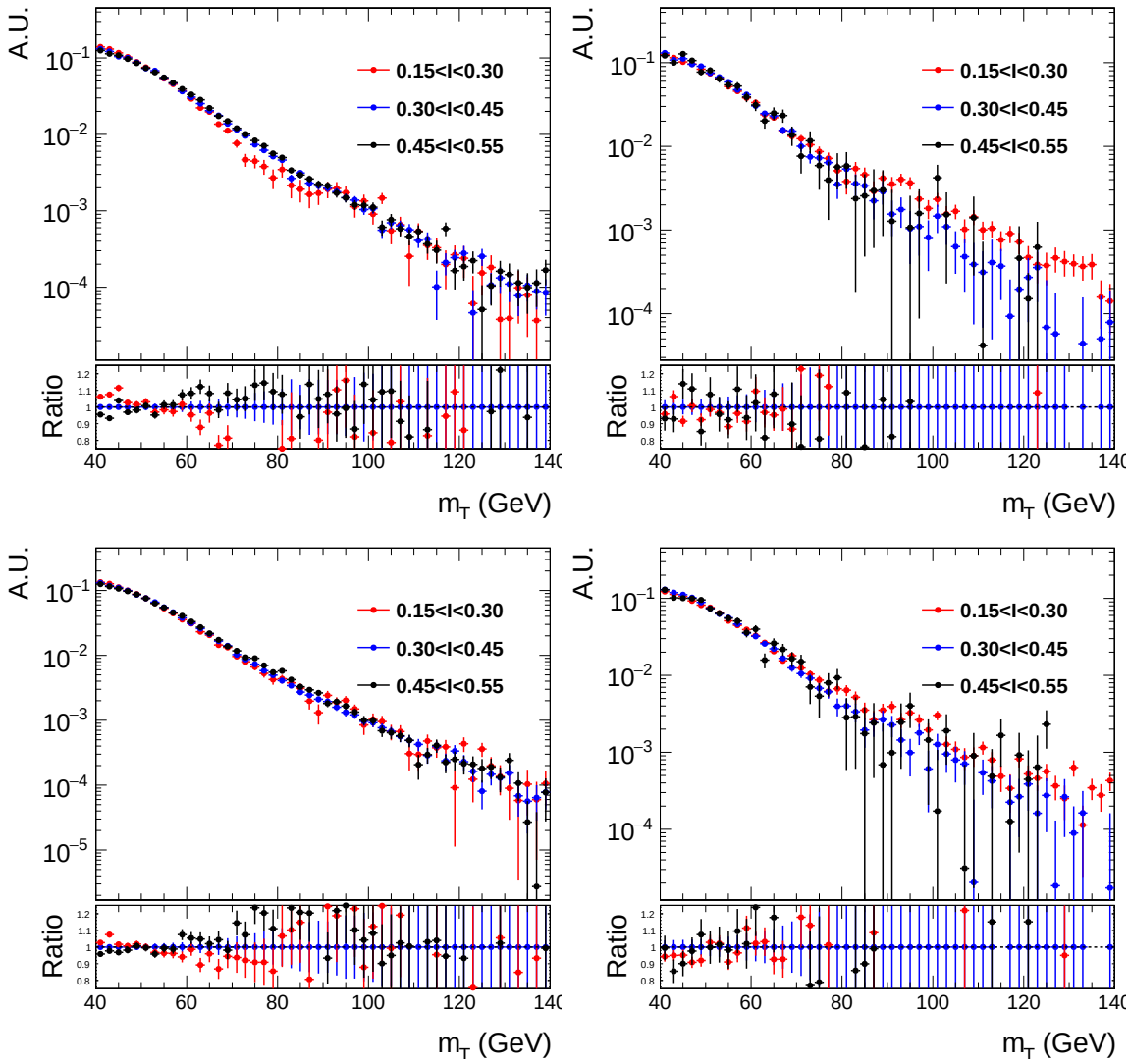

Figure 10-1: QCD control regions for the muon (left) and electron (right) channels with positive (top) and negative (bottom) charges.

10.4 Uncertainties

Uncertainties in corrections are propagated to the final observable distributions m_{T} and M_{ll}. These include variations on the lepton momentum scale factors, recoil corrections, prefiring probability, and lepton efficiency. Estimation of the uncertainties in each of these corrections is described in their respective chapters. This section summarizes how each of the uncertainties is propagated to the final discriminant distributions.

E_{T}^{miss} Uncertainties

Each uncertainty in E_{T}^{miss} modeling is an alternate set of recoil corrections which produces a variant on the m_{T} distribution. The difference between the baseline m_{T} distribution and each variant due to uncertainty in E_{T}^{miss} modeling is taken as the uncertainty. This is propagated into the final fit as a shape uncertainty by symmetrizing around the central m_{T} distribution. E_{T}^{miss} uncertainties are only applicable to the W and Z boson processes in the W^+ and W^- boson signal channels. As described in Chapter 9.4, there are a total of twelve uncertainty shapes from E_{T}^{miss} modeling—two due to model assumptions and ten due to each of the free parameters in each p_{T} bin fit. Each source of uncertainty is considered uncorrelated from the others.

Lepton Efficiency Uncertainties

Differences in lepton reconstruction and identification efficiency due to model and even selection choices are described in Chapter 7.3. These uncertainties are applicable to all simulated processes in each of the W^+, W^-, and Z boson channels. Each uncertainty is taken as the difference between M_{ll} and m_{T} distributions with the baseline efficiency value and one of the variations. As with the E_{T}^{miss} uncertainties, these are symmetrized around the central value of M_{ll} or m_{T} for each channel. Each source of uncertainty—MC generator, FSR model, background model, tag selection—is considered uncorrelated from the others.

Lepton Momentum Uncertainties

Uncertainties in lepton momentum scale factors are also propagated to M_{ll} and m_T distributions. Differences between distributions constructed from the central value and $+1\sigma$ and -1σ variations on the lepton momentum are taken as the uncertainty.

QCD shape uncertainty

As described in the prior section, the QCD multijet background m_T distribution is estimated from data using non-isolated leptons in the range $0.30 < I < 0.45$. To account for differences in m_T distribution across varying levels of isolation, an uncertainty is taken as the difference between the m_T distributions in $0.30 < I < 0.45$ and $0.45 < I < 0.55$. As with the E_T^{miss} and efficiency scale factor uncertainties, the full uncertainty description is taken by symmetrizing around the central values from the $0.30 < I < 0.45$ region. The QCD multijet uncertainty is considered uncorrelated between the W^+ and W^- boson channels.

10.5 Summary

The observed yields resulting from the signal extraction fits for all signal and background processes are listed in Table 10.1 (Table 10.3) for the electron channels and Table 10.2 (Table 10.4) for the muon channels at $\sqrt{s} = 5.02\,\text{TeV}$ ($\sqrt{s} = 13\,\text{TeV}$). Quoted uncertainties include both statistical and systematic sources. The Z boson M_{ll} distributions are shown in Figure 10-2 for $\sqrt{s} = 5.02\,\text{TeV}$ and Figure 10-3 for $\sqrt{s} = 13\,\text{TeV}$. The m_T distributions for the W analyses are shown in Figure 10-4 for W^+ and Figure 10-5 for W^-.

Process	$Z \to ee$	$W^+ \to e^+\nu$	$W^- \to e^-\nu$
Data	47734	438547	289179
Signal	747323 ± 862	398952 ± 338	252850 ± 274
QCD multijet	72 ± 5	27181 ± 333	25968 ± 305
$t\bar{t}$	32 ± 3	679 ± 11	677 ± 11
Drell–Yan	508 ± 9	11734 ± 176	9684 ± 173
$W \to \tau\nu$	< 1	7372 ± 165	5649 ± 159
Diboson	54 ± 5	88 ± 1	80 ± 1

Table 10.1: Best-fit yields from various processes in Z, W^+, and W^- boson with electron final states at $\sqrt{s} = 5.02\,\text{TeV}$. Uncertainties shown are a combination of systematic and statistical.

Process	$Z \to \mu\mu$	$W^+ \to \mu^+\nu$	$W^- \to \mu^-\nu$
Data	79345	672817	428156
Signal	79076 ± 249	626189 ± 554	389637 ± 420
QCD multijet	58 ± 4	12496 ± 238	12616 ± 162
$t\bar{t}$	49 ± 5	828 ± 13	836 ± 14
Drell–Yan	126 ± 3	33295 ± 258	25066 ± 194
$W \to \tau\nu$	< 1	13268 ± 232	8450 ± 159
Diboson	88 ± 9	125 ± 2	112 ± 2

Table 10.2: Best-fit yields from various processes in Z, W^+, and W^- bosons with muon final states at $\sqrt{s} = 5.02\,\text{TeV}$. Uncertainties shown are a combination of systematic and statistical.

Process	$Z \to ee$	$W^+ \to e^+\nu$	$W^- \to e^-\nu$
Data	76229	709630	578135
Signal	73800 ± 1320	605443 ± 372	477096 ± 342
QCD multijet	98 ± 4	77133 ± 475	76496 ± 442
$t\bar{t}$	203 ± 21	5833 ± 94	5871 ± 94
Drell–Yan	748 ± 14	21222 ± 167	18653 ± 153
$W \to \tau\nu$	< 1	9434 ± 109	7422 ± 93
Diboson	93 ± 9	240 ± 3	231 ± 3

Table 10.3: Best-fit yields from various processes in Z, W^+, and W^- bosons with electron final states at $\sqrt{s} = 13\,\text{TeV}$. Uncertainties shown are a combination of systematic and statistical

Process	$Z \to \mu\mu$	$W^+ \to \mu^+\nu$	$W^- \to \mu^-\nu$
Data	128713	1014670	795518
Signal	126473 ± 2261	902641 ± 666	696182 ± 586
QCD multijet	99 ± 6	50374 ± 337	46450 ± 315
$t\bar{t}$	326 ± 34	6558 ± 100	6148 ± 89
Drell–Yan	204 ± 4	55084 ± 305	46742 ± 241
$W \to \tau\nu$	< 1	17802 ± 229	14285 ± 170
Diboson	151 ± 15	317 ± 4	296 ± 4

Table 10.4: Best-fit yields from various processes in Z, W^+, and W^- bosons with muon final states at $\sqrt{s} = 13\,\text{TeV}$. Uncertainties shown are a combination of systematic and statistical.

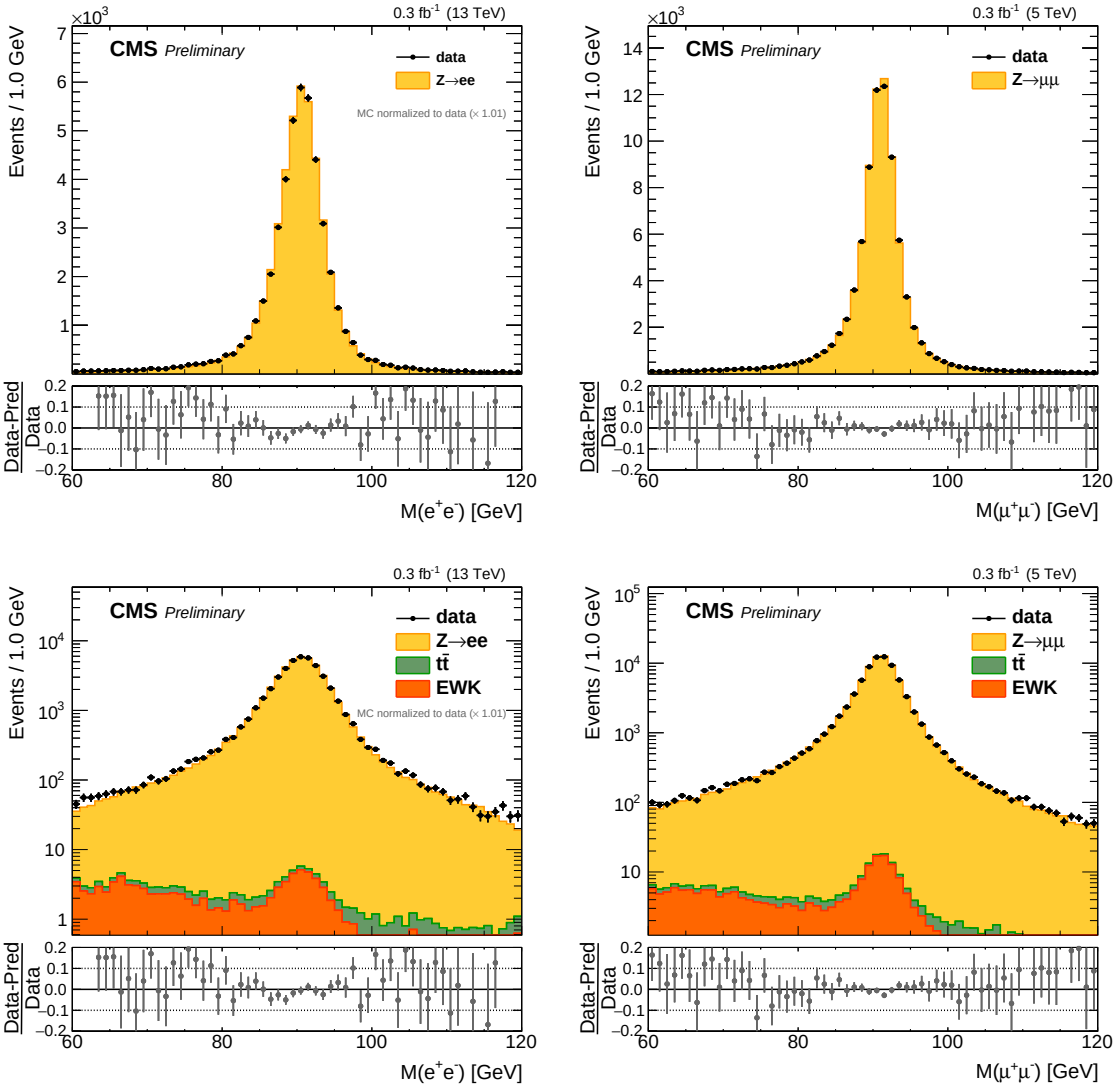

Figure 10-2: The M_{ll} distributions for $Z \to ee$ (left) and $Z \to \mu\mu$ (right) at $\sqrt{s} = 5.02\,\text{TeV}$. The simulated events have been normalized to data.

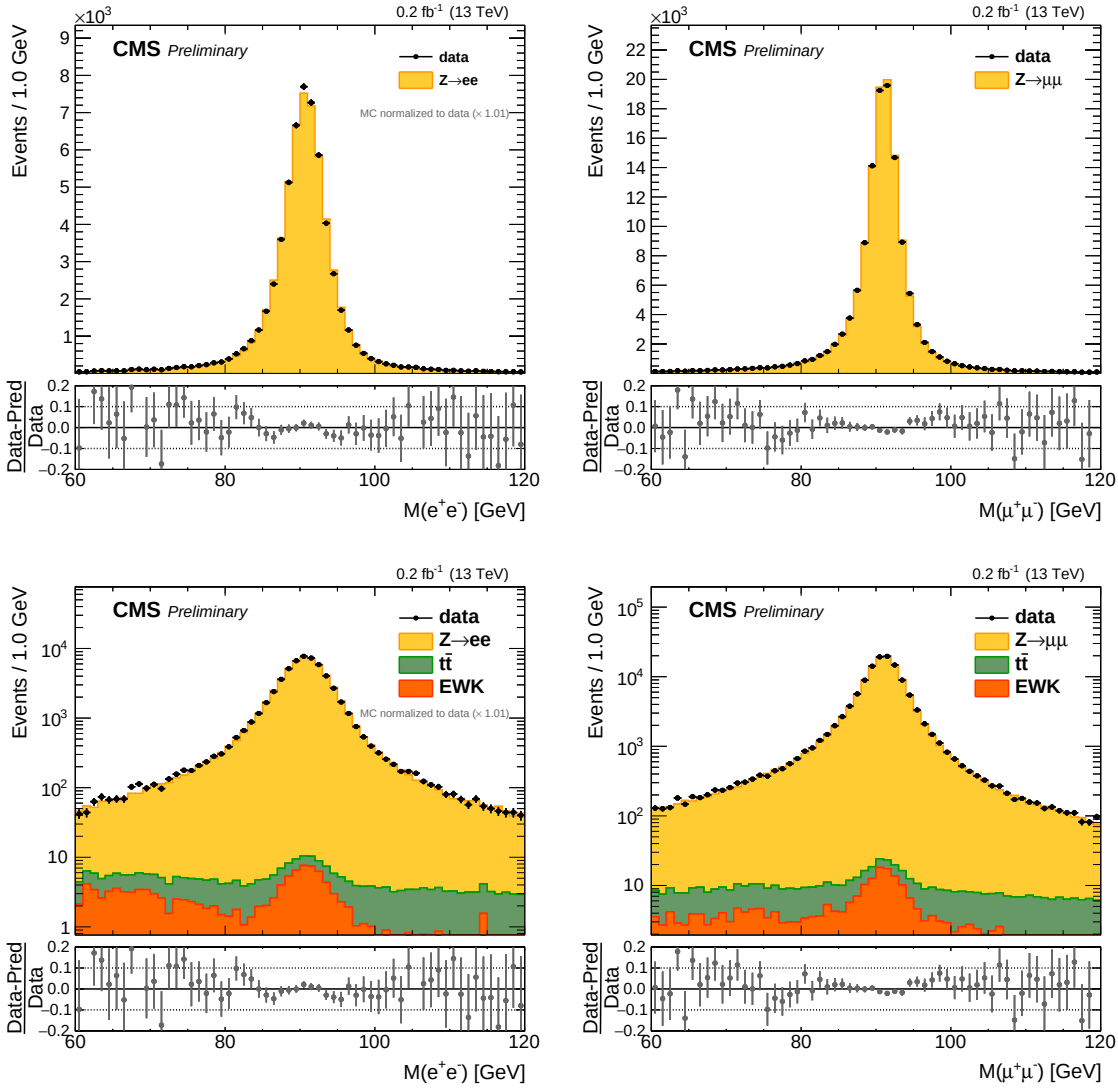

Figure 10-3: The M_{ll} distributions for $Z \to ee$ (left) and $Z \to \mu\mu$ (right) at $\sqrt{s} = 13\,\text{TeV}$. The simulated events have been normalized to data.

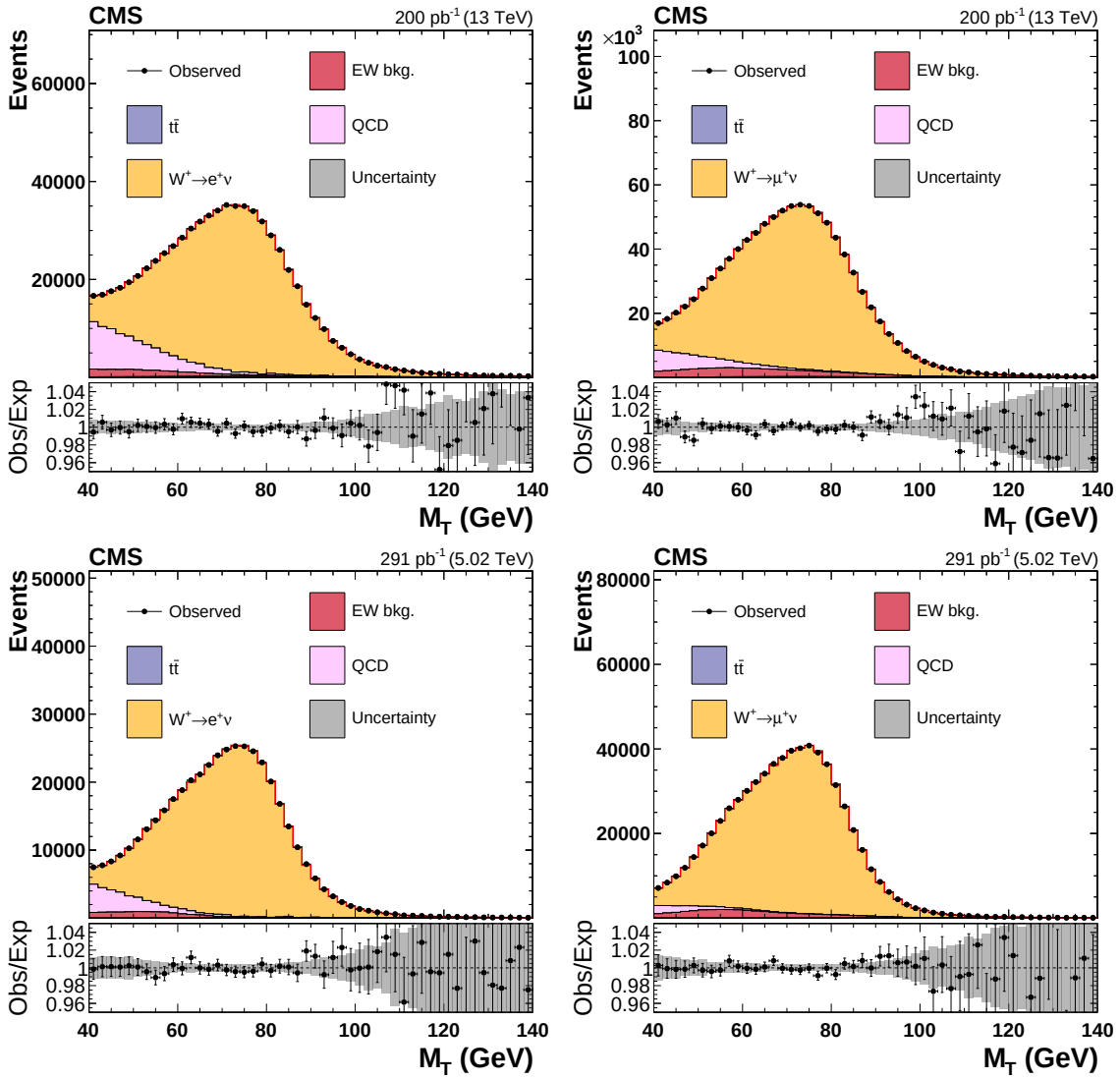

Figure 10-4: Distributions of m_{T} in the W^+ signal selection for electron (left) and muon (right) final states for the pp collisions at $\sqrt{s} = 13\,\mathrm{TeV}$ (upper) and $\sqrt{s} = 5.02\,\mathrm{TeV}$ (lower). The histograms for EW backgrounds include the contributions from Drell–Yan, $W \to \tau\nu$, and diboson processes. The predicted yields are shown with their best-fit normalizations from the fit. The bottom panel in each figure shows the ratio of the number of events observed in data to that of the total signal and background predictions.

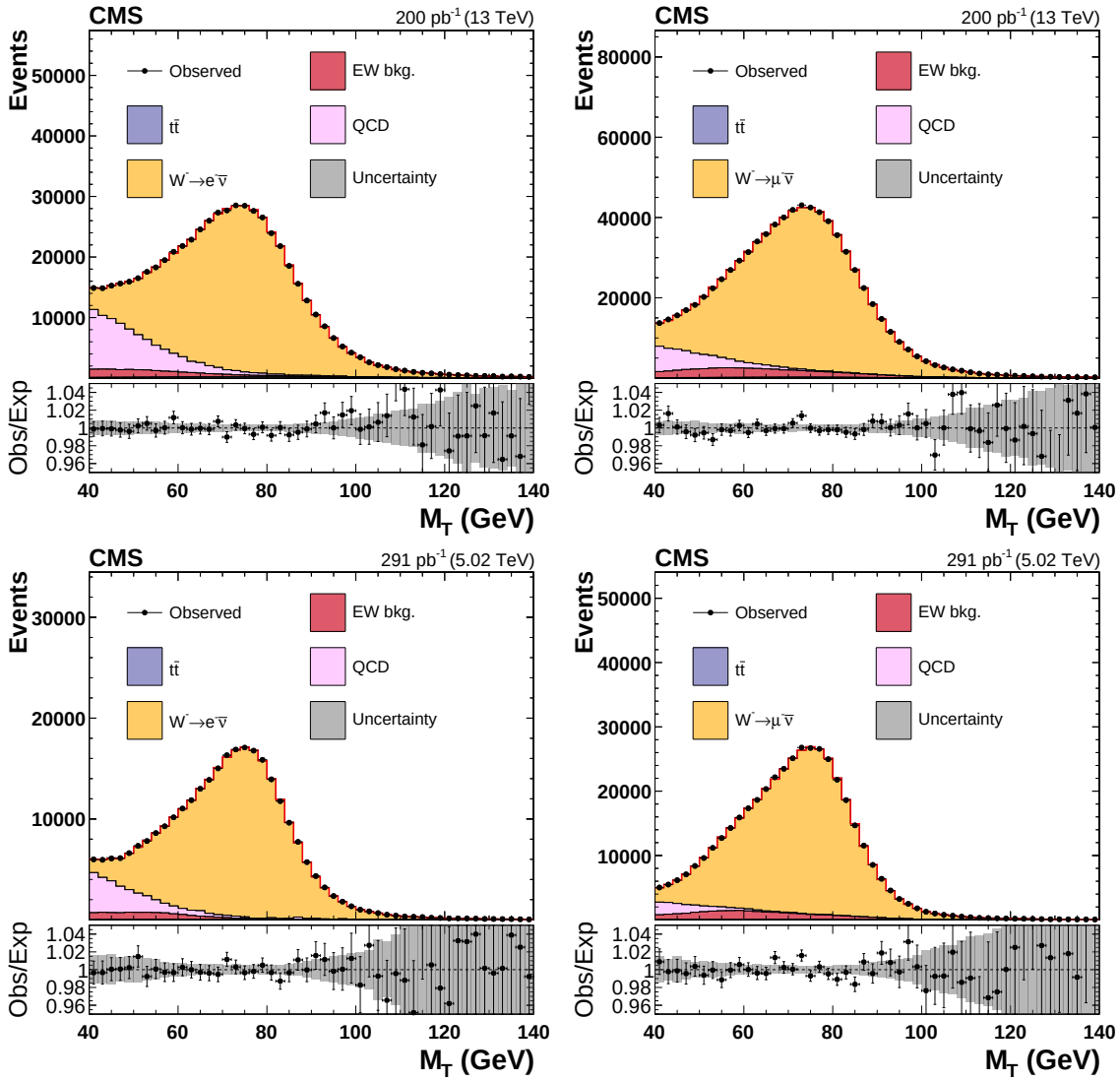

Figure 10-5: Distributions of m_{T} in the W^- signal selection for electron (left) and muon (right) final states for the pp collisions at $\sqrt{s} = 13\,\mathrm{TeV}$ (upper) and $\sqrt{s} = 5.02\,\mathrm{TeV}$ (lower). The histograms for EW backgrounds include the contributions from Drell–Yan, $W \to \tau\nu$, and diboson processes. The predicted yields are shown with their best-fit normalizations from the fit. The bottom panel in each figure shows the ratio of the number of events observed in data to that of the total signal and background predictions.

Chapter 11

Systematic Uncertainties

11.1 Overview

Systematic uncertainties which are taken into account in the simultaneous fit of W^+, W^-, and Z are briefly described. Uncertainties in kinematic observables such as lepton p_{T} or E_{T}^{miss} which additionally impact the m_{T} and M_{ll} distributions are included as shape uncertainties. Detailed descriptions were provided in the respective chapters, and the uncertainties are summarized briefly here.

Luminosity

The luminosity uncertainty for datasets used in this analysis is 4.8% for $\sqrt{s} = 5.02\,\mathrm{TeV}$ dataset and 1.7% for the $\sqrt{s} = 13\,\mathrm{TeV}$ dataset.

Lepton Efficiency

Potential bias in measuring the lepton reconstruction and identification efficiency is estimated by varying the modeling of signal and backgrounds used in the efficiency fits. Signal models constructed from dilepton M_{ll} distributions using different generator and final-state radiation programs are compared. Additionally an alternative background modeling function is used in the fits. Tag selection criteria for the tag-and-probe is included by varying the tag selection requirements. These uncertainties

are correlated between W^+, W^-, and Z channels for a given lepton flavor. Statistical uncertainties are considered uncorrelated in p_{T} and η bins and efficiency categories, and are also uncorrelated in the W^+,W^-, and Z channels.

Lepton Momentum Scale

The lepton p_{T} is varied by the uncertainty in the lepton momentum scale corrections. The variations in lepton p_{T} are propagated to the m_{T} and M_{ll} observables. This is treated as correlated.

ECAL Pre-Firing

The uncertainty in the pre-firing probability for an object is 20% of the pre-firing probability or the statistical uncertainty in the correction factor, whichever is more. This is treated as fully correlated.

E_{T}^{miss} Modeling

Bias due to assumptions made in modeling hadronic recoil are estimated by an alternative model. Assumptions about rapidity binning are accounted for with corrections derived in 3 $|y|$ bins and model choice is accounted for by using a Gaussian kernel fitting function. Statistical uncertainties are evaluated by creating correction sets through a principal component analysis with one uncertainty per free parameter. Variants of m_{T} distributions are treated as fully correlated in the W^+ and W^- channels.

Background Modeling

A shape uncertainty due to the QCD background selection in the W channels is derived from differences in m_{T} distributions in the $0.30 < \mathrm{Iso} < 0.45$ and $0.45 < \mathrm{Iso} < 0.60$ control regions. Normalization uncertainties are applied to the $t\bar{t}$ and diboson backgrounds in the Z channel and additionally to the Drell-Yann background in the W channels.

Source	W^+	W^-	W	W^+/W^-	Z	W^+/Z	W^-/Z	W/Z
Lepton Reco & ID	0.36	0.35	0.29	0.48	0.39	0.50	0.52	0.49
Background modeling	0.13	0.15	0.15	0.19	0.12	0.16	0.18	0.13
Recoil modeling	0.04	0.06	0.06	0.05	0.04	0.06	0.05	0.05
Prefire	0.26	0.24	0.24	0.02	0.31	0.07	0.09	0.08
Total Meas.	0.44	0.44	0.39	0.51	0.50	0.52	0.55	0.50
Theory Unc.	0.34	0.48	0.40	0.36	0.30	0.50	0.56	0.49
Luminosity	1.50	1.50	1.50	0.00	1.50	0.00	0.00	0.00
Total [%]	1.60	1.63	1.60	0.62	1.61	0.72	0.78	0.70

Table 11.1: Systematic uncertainties for all muon channel measurements at $\sqrt{s} = 5.02\,\text{TeV}$.

Theoretical Uncertainties

Variations in theoretical predictions of cross sections are evaluated for different soucres—QCD factorization (μ_F) and renormalization scale (μ_R), PDF variations, resummation schemes, and final-state radiation models. Uncertainties from QCD scale variations and PDF uncertainties are treated as correlated, while the FSR modeling uncertainties are uncorrelated.

11.2 Summary

Summaries of uncertainties are listed in Table 11.3 and Table 11.4 for the $\sqrt{s} = 13\,\text{TeV}$ muon and electron channels. Table 11.1 and Table 11.2 contain summaries of the muon and electron channel uncertainties at $\sqrt{s} = 5.02\,\text{TeV}$.

Source	W^+	W^-	W	W^+/W^-	Z	W^+/Z	W^-/Z	W/Z
Lepton Reco & ID	0.50	0.50	0.36	0.7	0.53	0.61	0.61	0.66
Charge Mis-ID	0.060	0.079	0	0.018	0.178	0.117	0.099	0.178
Background modeling	0.32	0.37	0.37	0.35	0.31	0.27	0.35	0.24
Recoil modeling	0.12	0.13	0.10	0.06	0.17	0.10	0.15	0.12
Prefire	0.49	0.47	0.47	0.02	0.74	0.29	0.32	0.30
Total Meas.	0.78	0.78	0.69	0.72	0.98	0.74	0.79	0.78
Theory Unc.	0.49	0.49	0.42	0.39	0.31	0.66	0.50	0.56
Luminosity	1.50	1.50	1.50	0.00	1.50	0.00	0.00	0.00
Total [%]	1.76	1.76	1.70	0.82	1.82	0.99	0.93	0.96

Table 11.2: Systematic uncertainties for all electron channel measurements at $\sqrt{s} = 5.02\,\text{TeV}$.

Source	W^+	W^-	W	W^+/W^-	Z	W^+/Z	W^-/Z	W/Z
Lepton Reco & ID	0.35	0.33	0.28	0.45	0.39	0.51	0.51	0.49
Background modeling	0.12	0.13	0.13	0.13	0.12	0.14	0.15	0.13
Recoil modeling	0.06	0.07	0.07	0.02	0.04	0.03	0.04	0.03
Prefire	0.25	0.23	0.23	0.02	0.28	0.04	0.06	0.05
Total Meas.	0.44	0.40	0.36	0.46	0.48	0.52	0.53	0.50
Theory Unc.	0.80	0.76	0.79	0.28	0.61	0.38	0.41	0.37
Luminosity	1.70	1.70	1.70	0.00	1.70	0.00	0.00	0.00
Total [%]	1.93	1.90	1.91	0.53	1.87	0.64	0.66	0.62

Table 11.3: Systematic uncertainties for all muon channel measurements at $\sqrt{s} = 13\,\text{TeV}$.

Source	W^+	W^-	W	W^+/W^-	Z	W^+/Z	W^-/Z	W/Z
Lepton Reco & ID	0.50	0.50	0.36	0.7	0.53	0.61	0.61	0.66
Charge Mis-ID	0.07	0.09	-	0.02	0.21	0.14	0.12	0.21
Background modeling	0.33	0.33	0.33	0.27	0.32	0.23	0.25	0.20
Recoil modeling	0.12	0.10	0.10	0.04	0.19	0.10	0.14	0.12
Prefire	0.55	0.47	0.47	0.07	0.67	0.16	0.23	0.20
Total Meas.	0.81	0.76	0.67	0.69	0.94	0.68	0.71	0.75
Theory Unc.	0.91	0.80	0.83	0.38	0.62	0.60	0.38	0.48
Luminosity	1.70	1.70	1.70	0.00	1.70	0.00	0.01	0.01
Total [%]	2.09	2.03	2.01	0.78	2.04	0.91	0.80	0.89

Table 11.4: Systematic uncertainties for all electron channel measurements at $\sqrt{s} = 13\,\text{TeV}$.

Chapter 12

Results

Cross section measurements of W^+, W^-, W, and Z bosons, as well as the ratios, are presented for $\sqrt{s} = 5.02\,\text{TeV}$ and $\sqrt{s} = 13\,\text{TeV}$. Electron and muon final states are studied. Data studied in this analysis includes an integrated luminosity of $299.1 \pm 5\,\text{pb}^{-1}$ at $\sqrt{s} = 5.02\,\text{TeV}$ and $199.3 \pm 4\,\text{pb}^{-1}$ at $\sqrt{s} = 13\,\text{TeV}$. The measurement is performed with a simultaneous fit to the W^+, W^-, and Z boson channels, with background processes and modeling uncertainties correlated across the appropriate channels.

Theoretical predictions of the cross sections and ratios are provided to NNLO using FEWZ and the NNPDF3.1 and CT18 PDF sets. Contributions from both PDF and scale uncertainties are included. The Z boson cross sections require $60\,\text{GeV} \leq \text{M}_{ll} \leq 120\,\text{GeV}$. A summary of the NNPDF3.1 and CT18 PDF set cross section and cross section ratio predictions is shown in Table 12.1. A summary of of the inclusive cross section times branching ratio relative to the predictions from the NNPDF3.1 PDF set for $\sqrt{s} = 5.02\,\text{TeV}$ electron and muon channels is shown in Figure 12-1 and for $\sqrt{s} = 13\,\text{TeV}$ in Figure 12-2. Ratios of cross section time branching ratio with respect to the CT18 PDF set is shown in Figure 12-4 for $\sqrt{s} = 13\,\text{TeV}$ and Figure 12-3 for $\sqrt{s} = 5.02\,\text{TeV}$.

	13 TeV		5 TeV	
	NNPDF3.1	CT18	NNPDF3.1	CT18
σ^{tot}_{W+} [pb]	11571^{+28}_{-28}	11560^{+250}_{-250}	4395^{+48}_{-48}	4323^{+79}_{-124}
σ^{tot}_{W-} [pb]	8550^{+20}_{-20}	8525^{+181}_{-181}	2886^{+31}_{-31}	2858^{+49}_{-77}
σ^{tot}_{W} [pb]	20121^{+47}_{-47}	20085^{+426}_{426}	7280^{78}_{-78}	7181^{123}_{-193}
σ^{tot}_{Z} [pb]	1944^{+14}_{-14}	1922^{+41}_{-41}	$683^{+9.4}_{-9.4}$	659^{+10}_{-16}
$\sigma^{tot}_{W+}/\sigma^{tot}_{W-}$	$1.353^{+0.001}_{-0.001}$	$1.356^{+0.011}_{-0.011}$	$1.523^{+0.002}_{-0.002}$	$1.512^{+0.017}_{-0.016}$
$\sigma^{tot}_{W+}/\sigma^{tot}_{Z}$	$5.956^{+0.005}_{-0.005}$	$6.015^{+0.04}_{-0.04}$	$6.44^{+0.06}_{-0.06}$	$6.56^{+0.06}_{-0.06}$
$\sigma^{tot}_{W-}/\sigma^{tot}_{Z}$	$4.400^{+0.003}_{-0.003}$	$4.44^{+0.03}_{-0.03}$	$4.23^{+0.05}_{-0.05}$	$4.34^{+0.02}_{-0.03}$
$\sigma^{tot}_{W}/\sigma^{tot}_{Z}$	$10.36^{+0.01}_{-0.01}$	$10.45^{+0.07}_{-0.07}$	$10.66^{+0.077}_{-0.077}$	$10.91^{+0.11}_{-0.11}$

Table 12.1: Summary of predictions calculated at NNLO with FEWZ using the NNPDF3.1 and CT18 PDF sets. Cross sections and cross section ratios are provided for $\sqrt{s} = 5.02\,\text{TeV}$ and $\sqrt{s} = 13\,\text{TeV}$.

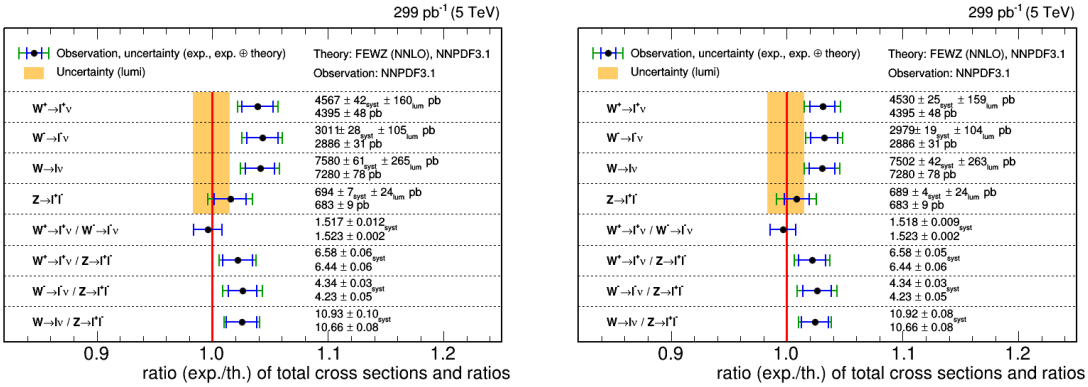

Figure 12-1: Summary of cross section results for the $\sqrt{s} = 5.02\,\text{TeV}$ electron (left) and muon (right) channels. Measured cross sections are compared to predicted values from NNPDF3.1.

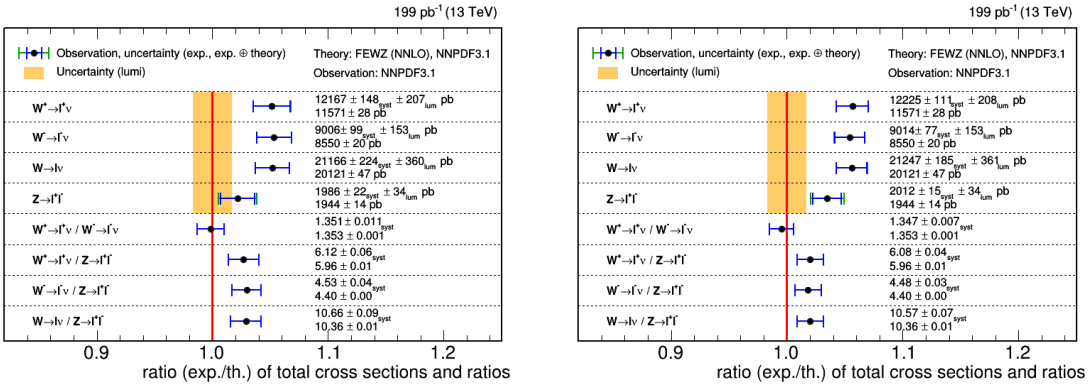

Figure 12-2: Summary of cross section results for the $\sqrt{s} = 13\,\text{TeV}$ electron (left) and muon (right) channels. Measured cross sections are compared to predicted values from the NNPDF3.1 PDF set.

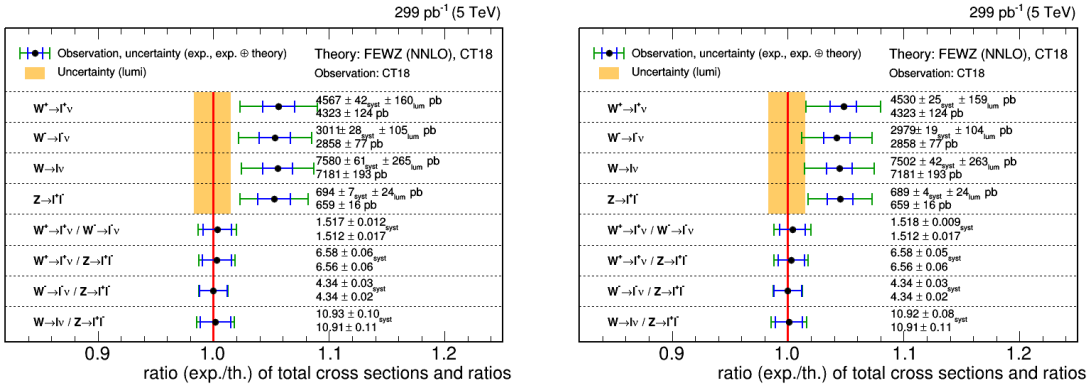

Figure 12-3: Summary of cross section results for the $\sqrt{s} = 5.02\,\text{TeV}$ electron (left) and muon (right) channel. Measured cross sections are compared to predicted values from the CT18 PDF set.

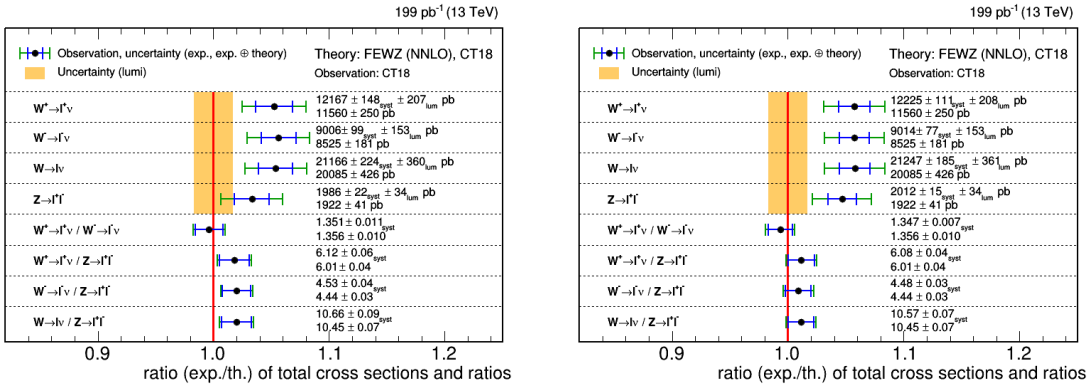

Figure 12-4: Summary of cross section results for the $\sqrt{s} = 13\,\text{TeV}$ electron (left) and muon (right) channel. Measured cross sections are compared to predicted values from the CT18 PDF set.

Chapter 13

Summary

Precision measurements of inclusive cross sections in the electron and muon channels at $\sqrt{s} = 5.02\,\text{TeV}$ and $\sqrt{s} = 13\,\text{TeV}$ are made for:

- W^+ boson cross section
- W^- boson cross section
- W boson cross section
- W^+/W^- cross section ratio
- Z boson cross section
- W^+/Z cross section ratio
- W^-/Z cross section ratio
- W/Z cross section ratio

These represent the first W and Z boson cross section measurements performed at the CMS experiment at $\sqrt{s} = 5.02\,\text{TeV}$. The measurements presented include systematic uncertainties of $< 1\%$ from the measurement and 1.7 % (1.5%) at $\sqrt{s} = 13\,\text{TeV}$ ($\sqrt{s} = 5.02\,\text{TeV}$) from the luminosity calibration.

Recap

Events were selected from well-identified and isolated electrons and muons. Candidate Z boson events required two oppositely charged leptons of the same flavor, and W boson events required the presence of a well-identified and isolated lepton with no other leptons reconstructed in the event. Lepton reconstruction and identification efficiency corrections were derived by the tag-and-probe method from $Z \to ee$ and $Z \to \mu\mu$ samples. Hadronic recoil corrections were derived from $Z \to \mu\mu$ in data and simulation and $W \to \mu\nu$ simulation, to improve E_{T}^{miss} modeling. Additionally, ECAL L1 prefiring efficiency corrections and lepton momentum scale and resolution corrections were applied. Uncertainties associated with these corrections were propagated from the physical observables to the final discriminant distribution. Uncertainties on theoretical calculations from higher-order QCD, NNLO QCD, NNLL resummation, and NLO EWK are also determined. Final yields and cross section values were determined by performing a fit simultaneously to the W^+, W^-, and Z boson channels. Uncertainties in observable distributions, uncertainties in normalizations, and background process normalizations were correlated in all channels where appropriate.

Discussion

The measured cross sections show good agreement between the electron and muon channels at each $\sqrt{s}$. The measured cross section value for W^+, W^-, W, and Z boson channels depends on the total integrated luminosity for the dataset, and at the time of writing this thesis the luminosity calibrations for these datasets were not finalized. Therefore, conclusions should not be drawn from comparisons between the inclusive cross sections of the $\sqrt{s} = 5.02\,\mathrm{TeV}$ and $\sqrt{s} = 13\,\mathrm{TeV}$ datasets. However, the cross section ratios W^+/W^-, W^+/Z, W^+/Z, W/Z are independent of the luminosity measurement. The ratio measurements are consistent across both lepton channels as well as both $\sqrt{s}$.

Precision measurements of the W^+, W^-, W, and Z boson production cross sec-

tions can directly provide insight into some of the proton PDFs as well as setting the foundation for further measurements, particularly differential cross sections, which are important to the global PDF fits. Inclusive cross section and ratio measurements can elucidate some information about the underlying flavor PDFs, for example the ratio of W^+/W^- is primarily affected by the relative contributions of the u and d while the W/Z ratios are additionally influenced by heavier flavor PDFs.

Appendix A

Lepton Efficiencies

A list of tables and figures for $\sqrt{s} = 5.02\,\text{TeV}$ and $\sqrt{s} = 13\,\text{TeV}$ is provided in Table A.1.

Category [13 TeV]	Figure	Table
electron GSF+ID+Iso	A-1	A.2
electron trigger	A-2(+), A-3(−)	A.3(+), A.4(−)
muon Sel.+ID+Iso	A-4	A.5
muon standalone	A-5	A.6
muon trigger	A-6(+), A-7(−)	A.7(+), A.8(−)
Category [5 TeV]	Figure	Table
electron GSF+ID+Iso	A-8	A.9
electron trigger	A-9(+), A-10(−)	A.10(+), A.11(−)
muon Sel.+ID+Iso	A-11	A.12
muon standalone	A-12	A.6
muon trigger	A-13(+), A-14(−)	A.14(+), A.15(−)

Table A.1: List of tables and figures containing $\sqrt{s} = 5.02\,\text{TeV}$ and $\sqrt{s} = 13\,\text{TeV}$ lepton efficiency scale factors.

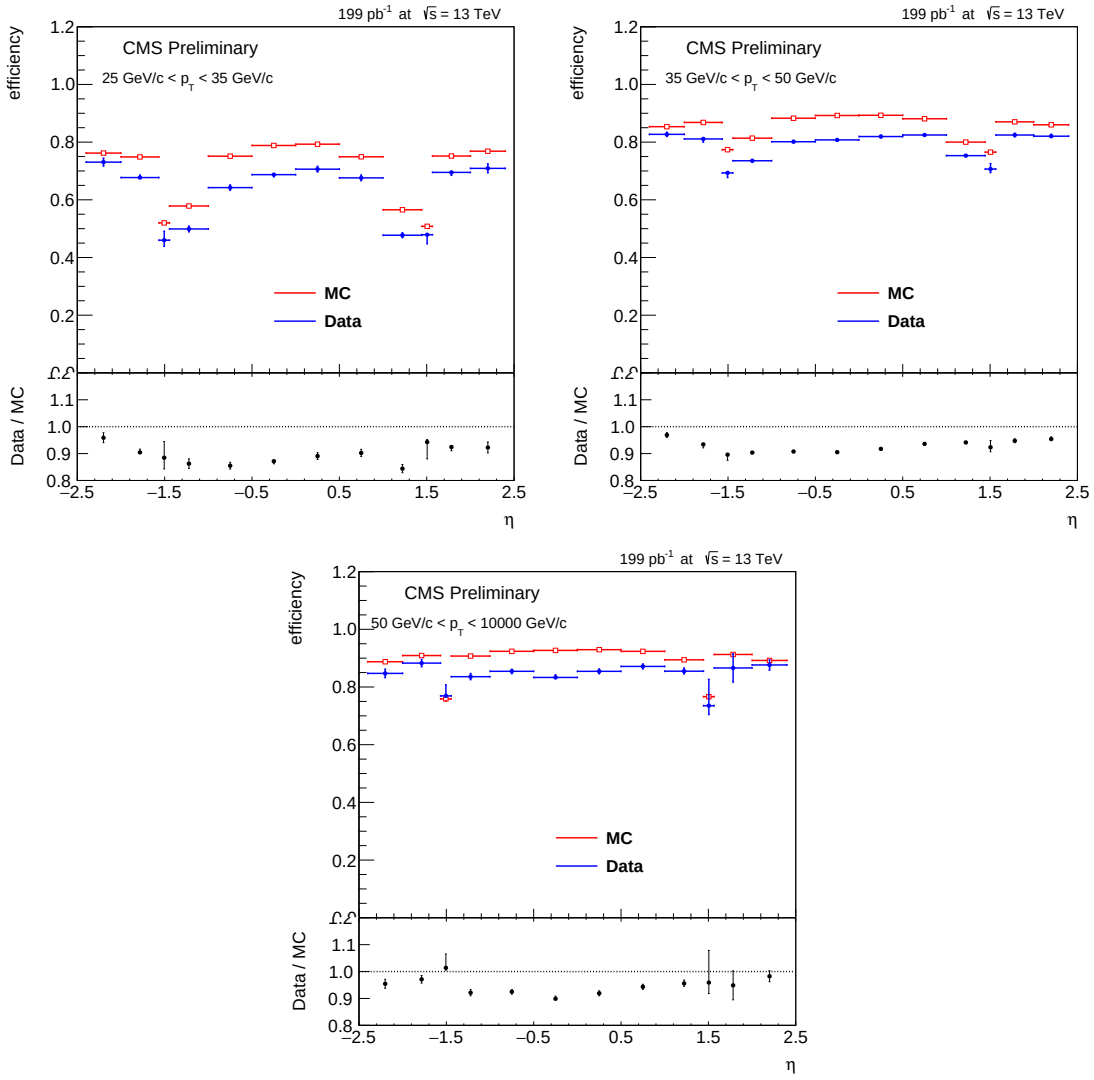

Figure A-1: η dependence of GSF electron identification and isolation efficiency scale factors, separated by p_T bins, for combined charged electrons in the 13 TeV samples.

	$-2.4 < \eta < -2$	$-2 < \eta < -1.566$	$-1.566 < \eta < -1.4442$	$-1.4442 < \eta < -1$	$-1 < \eta < -0.5$	$-0.5 < \eta < 0$
$25 < p_T < 35$	0.959 ± 0.018	0.904 ± 0.009	0.885 ± 0.052	0.863 ± 0.018	0.855 ± 0.013	0.872 ± 0.007
$35 < p_T < 50$	0.969 ± 0.009	0.934 ± 0.009	0.896 ± 0.015	0.904 ± 0.005	0.908 ± 0.003	0.905 ± 0.004
$50 < p_T < 1e+04$	0.955 ± 0.017	0.971 ± 0.014	1.014 ± 0.037	0.921 ± 0.012	0.925 ± 0.008	0.899 ± 0.007
	$0 < \eta < 0.5$	$0.5 < \eta < 1$	$1 < \eta < 1.44$	$1.44 < \eta < 1.57$	$1.57 < \eta < 2$	$2 < \eta < 2.4$
$25 < p_T < 35$	0.891 ± 0.013	0.902 ± 0.013	0.844 ± 0.015	0.943 ± 0.045	0.925 ± 0.010	0.922 ± 0.020
$35 < p_T < 50$	0.917 ± 0.005	0.936 ± 0.001	0.941 ± 0.001	0.923 ± 0.021	0.948 ± 0.007	0.954 ± 0.006
$50 < p_T < 1e+04$	0.919 ± 0.009	0.943 ± 0.009	0.956 ± 0.012	0.959 ± 0.089	0.949 ± 0.054	0.982 ± 0.020

Table A.2: GSF electron identification and isolation efficiency scale factors in (p_T, η) bins for combined charged electrons in the 13 TeV samples.

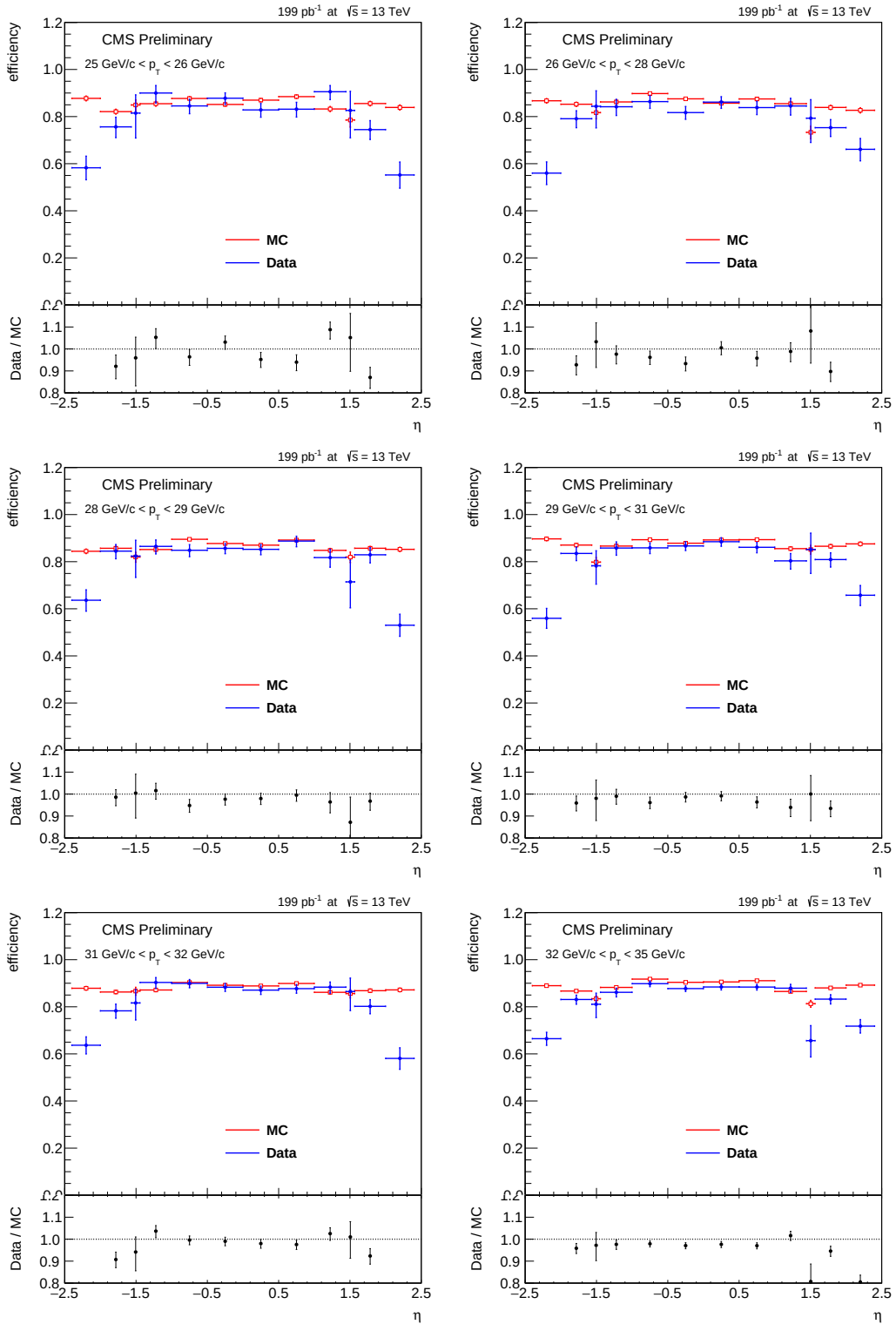

Figure A-2: η dependence of Single electron trigger efficiency scale factors, separated by p_T bins, for positively charged electrons in the 13 TeV samples.

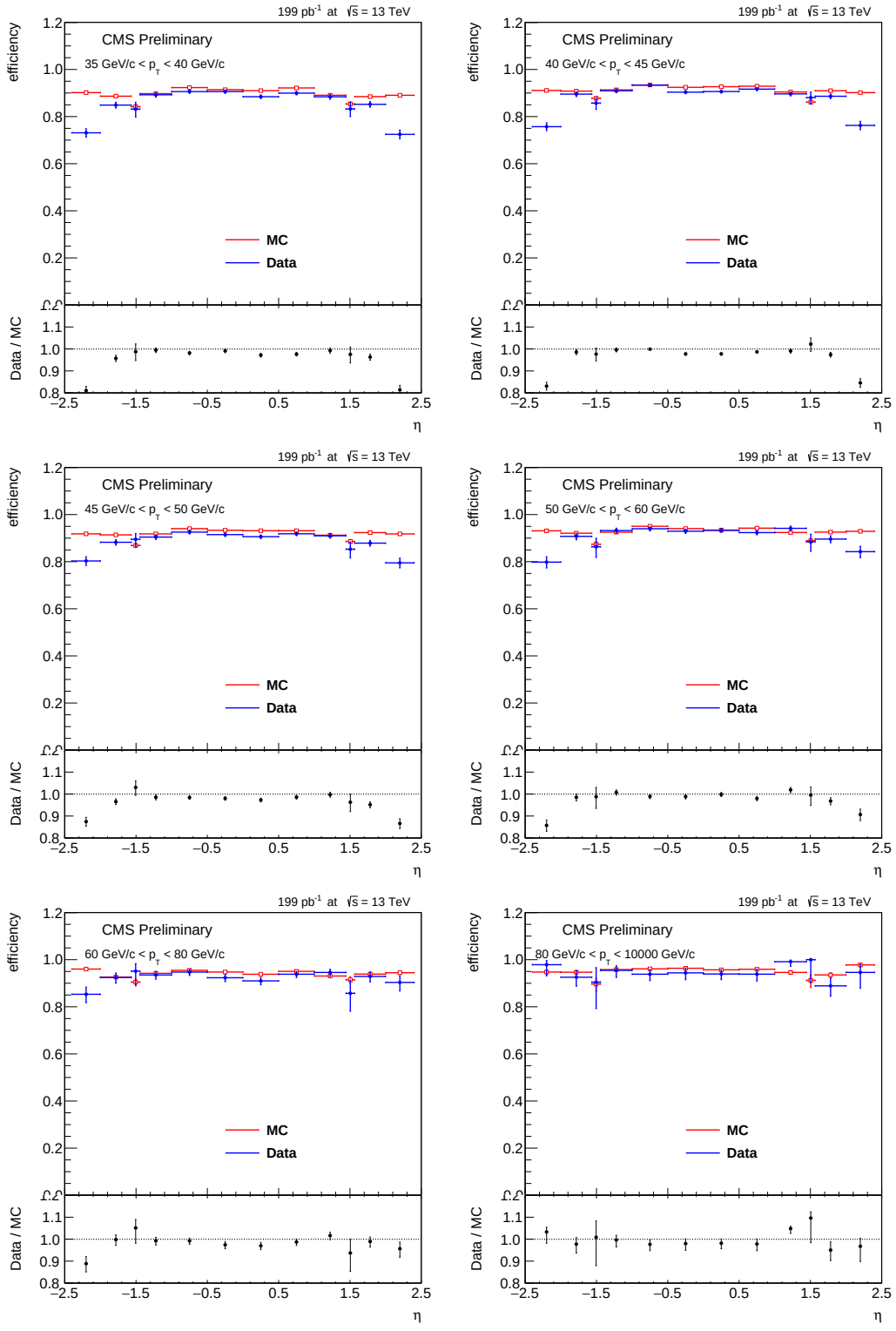

Figure A-2: η dependence of Single electron trigger efficiency scale factors, separated by p_T bins, for positively charged electrons in the 13 TeV samples.

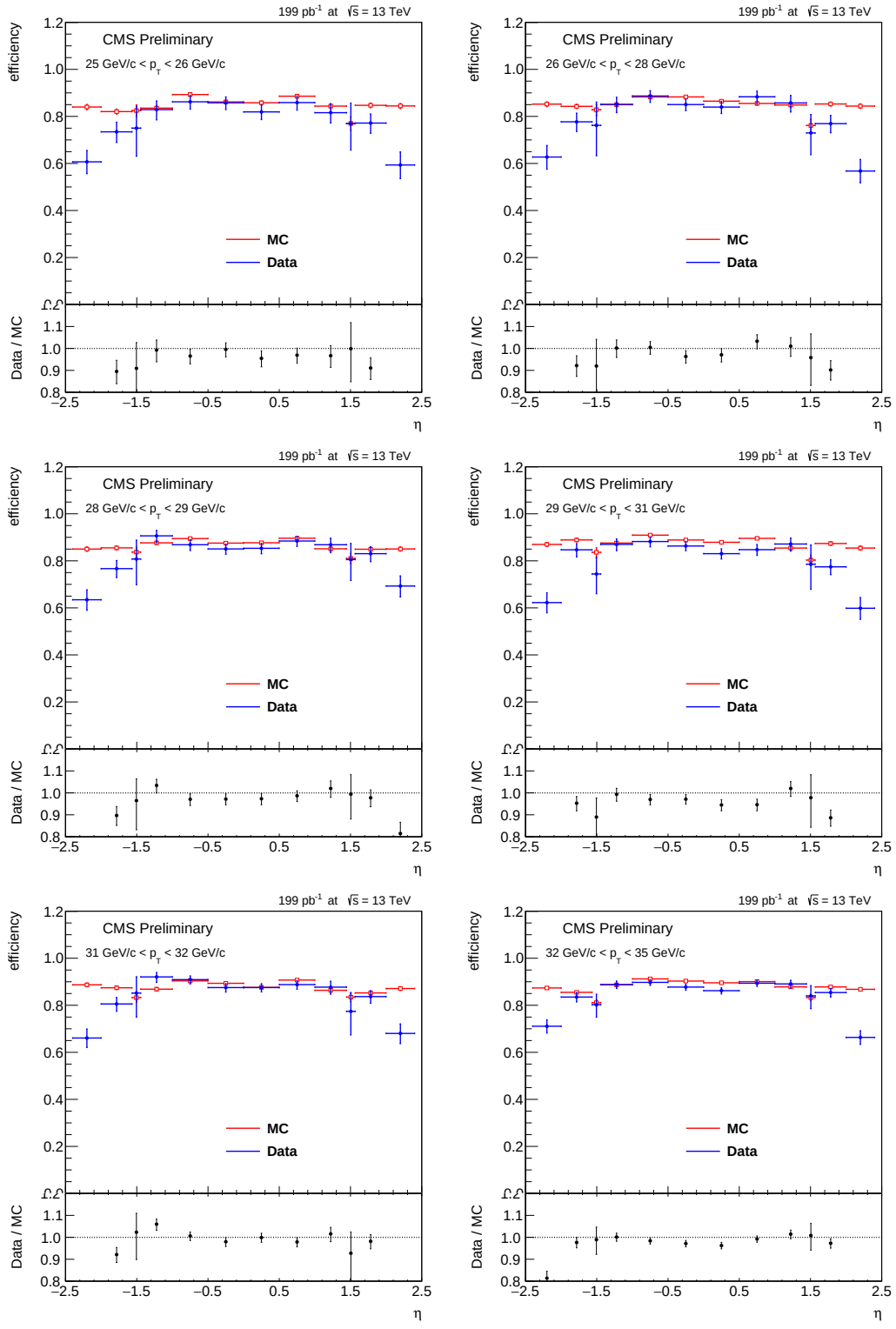

Figure A-3: η dependence of Single electron trigger efficiency scale factors, separated by p_T bins, for negatively charged electrons in the 13 TeV samples.

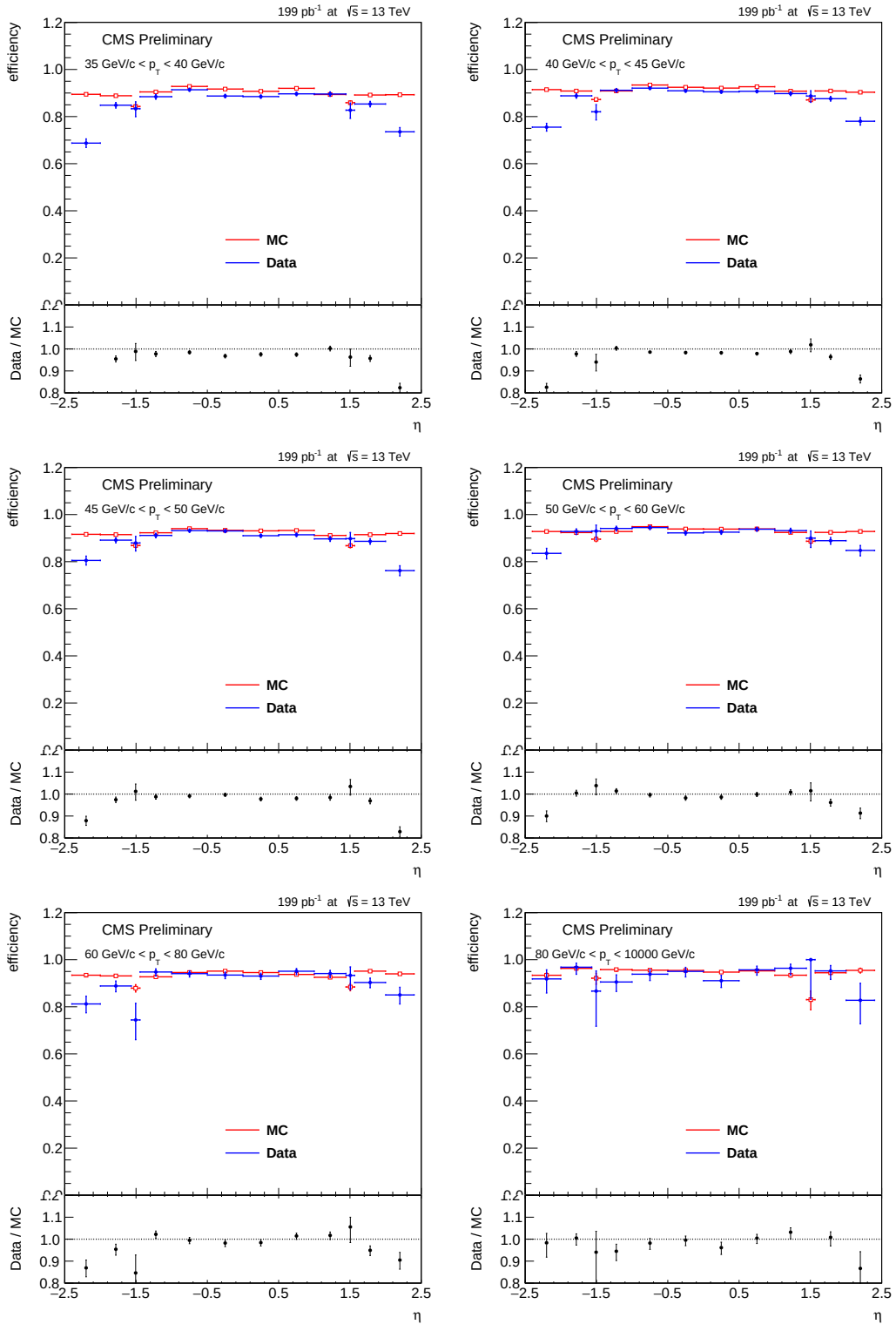

Figure A-3: η dependence of Single electron trigger efficiency scale factors, separated by p_T bins, for negatively charged electrons in the 13 TeV samples.

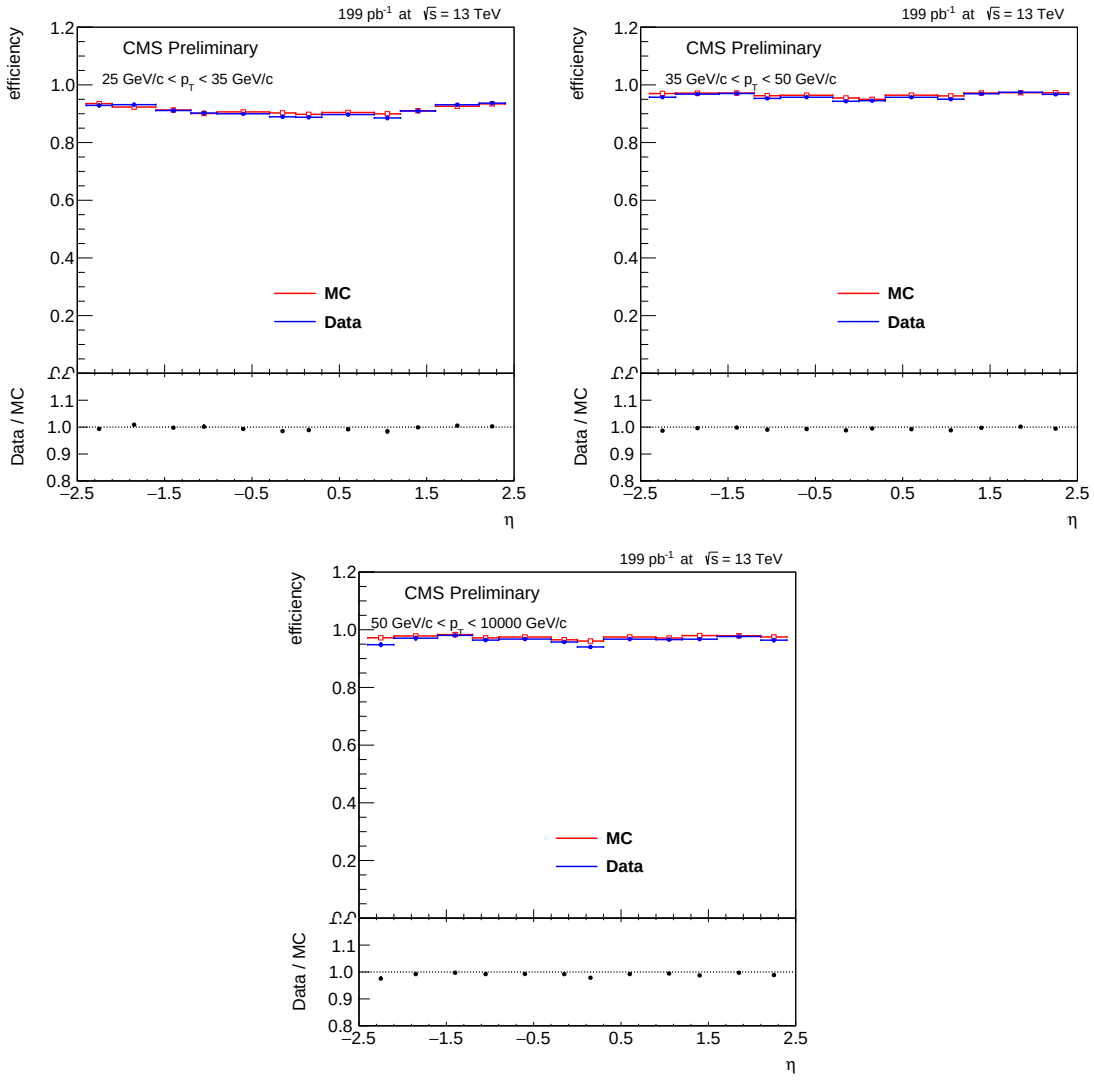

Figure A-4: η dependence of Muon selection efficiency scale factors, separated by p_T bins, for combined charged muons in the 13 TeV samples.

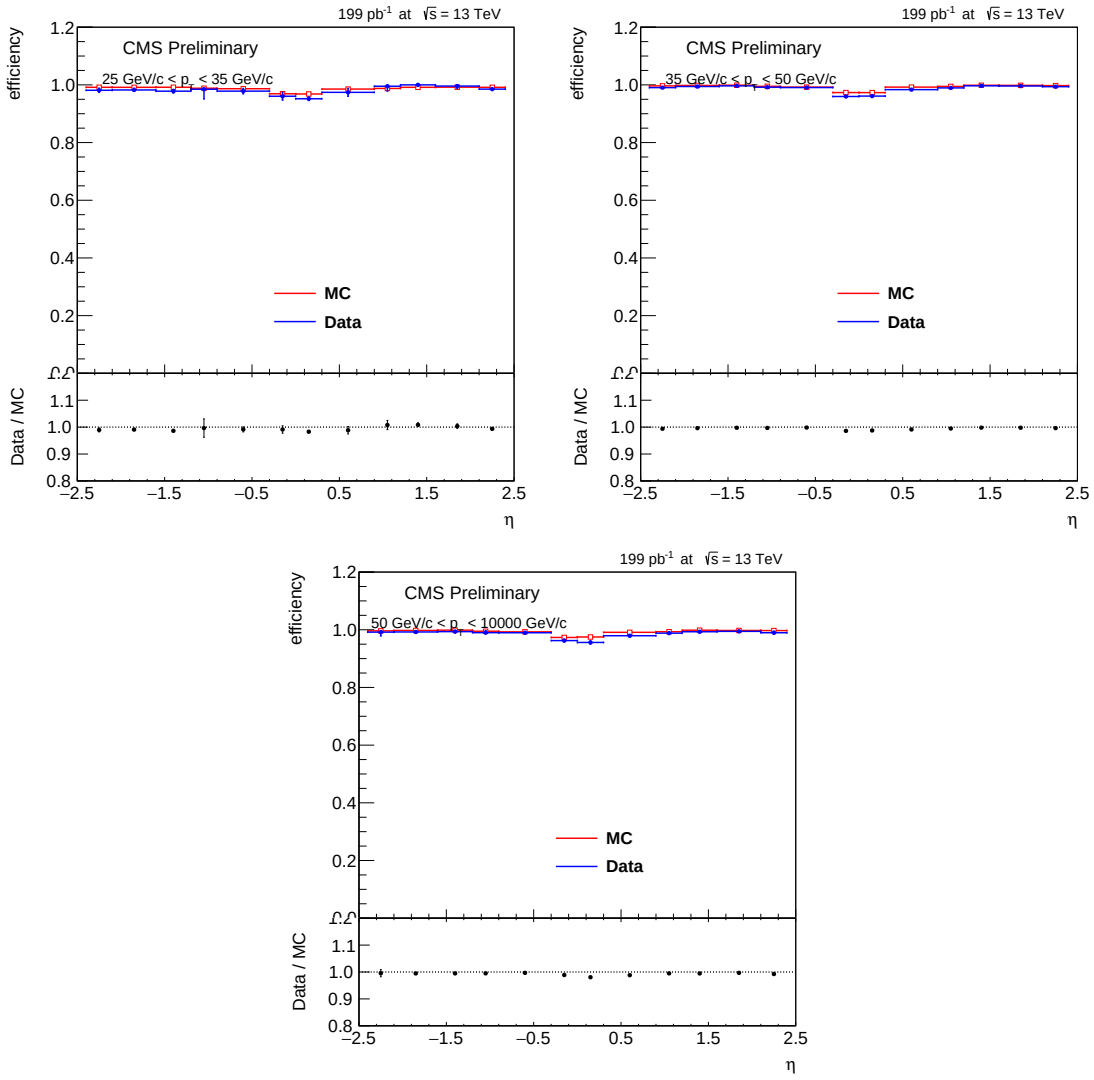

Figure A-5: η dependence of Standalone muon identification efficiency scale factors, separated by p_T bins, for combined charged muons in the 13 TeV samples.

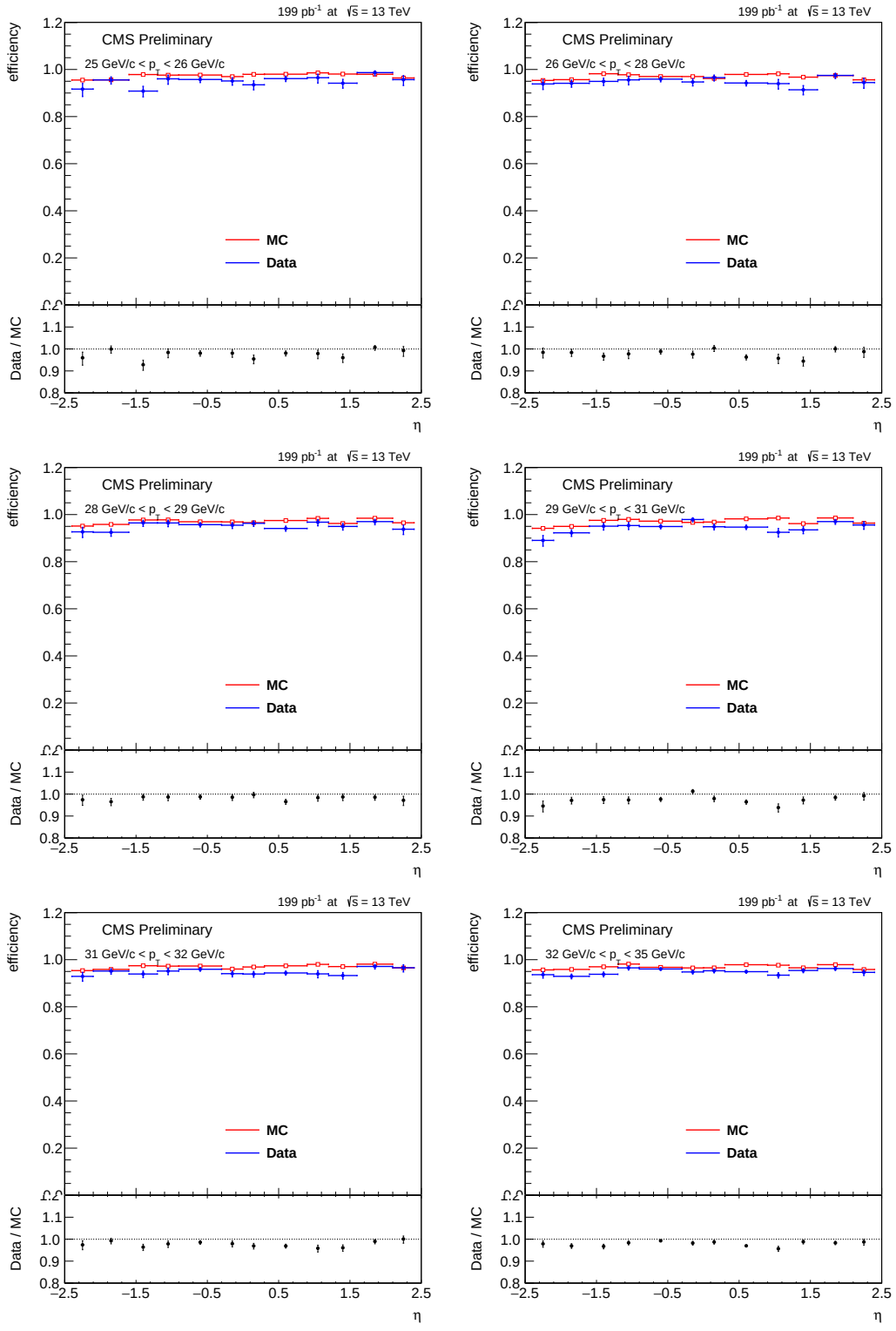

Figure A-6: η dependence of Single muon trigger efficiency scale factors, separated by p_T bins, for positively charged muons in the 13 TeV samples.

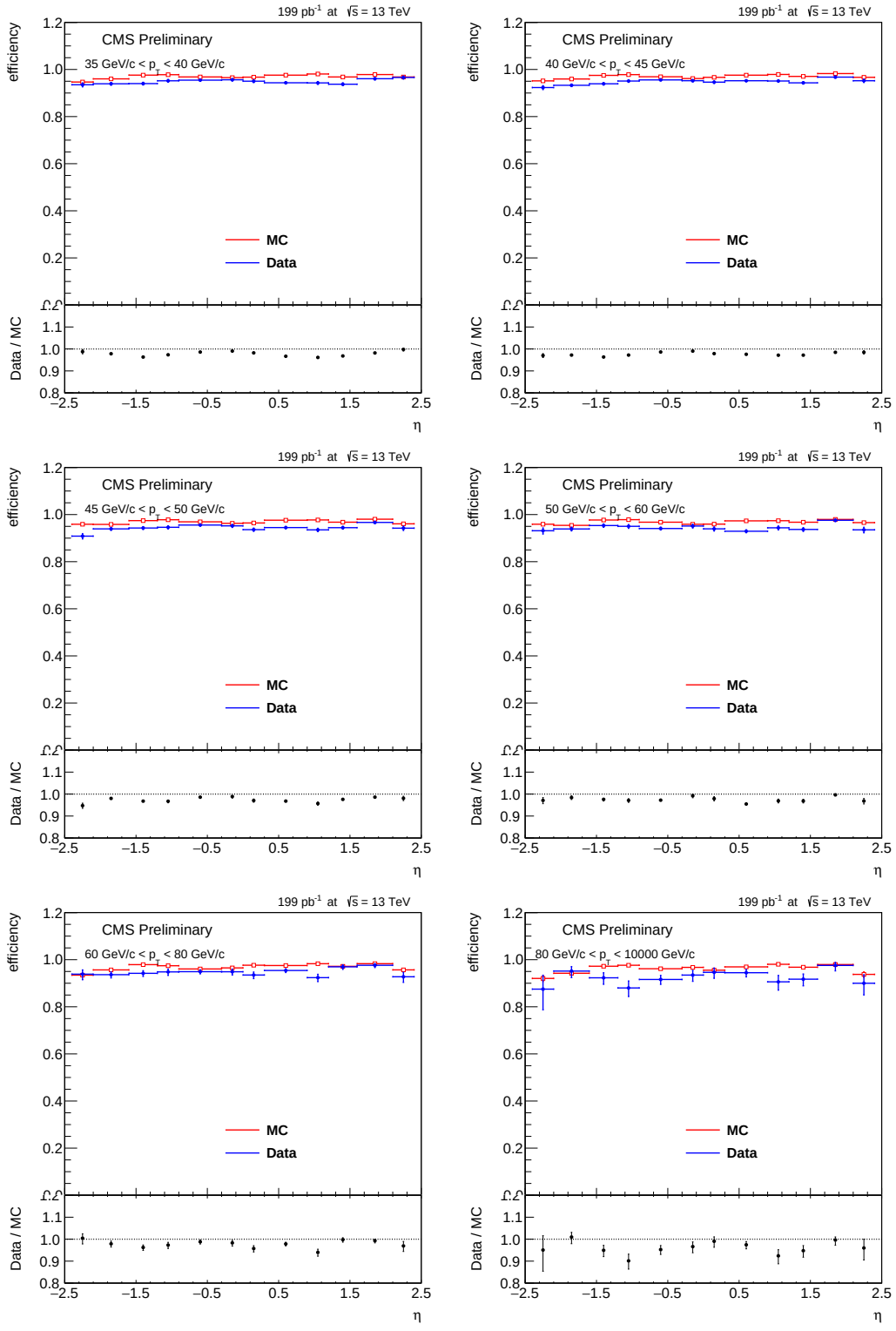

Figure A-6: η dependence of Single muon trigger efficiency scale factors, separated by p_T bins, for positively charged muons in the 13 TeV samples.

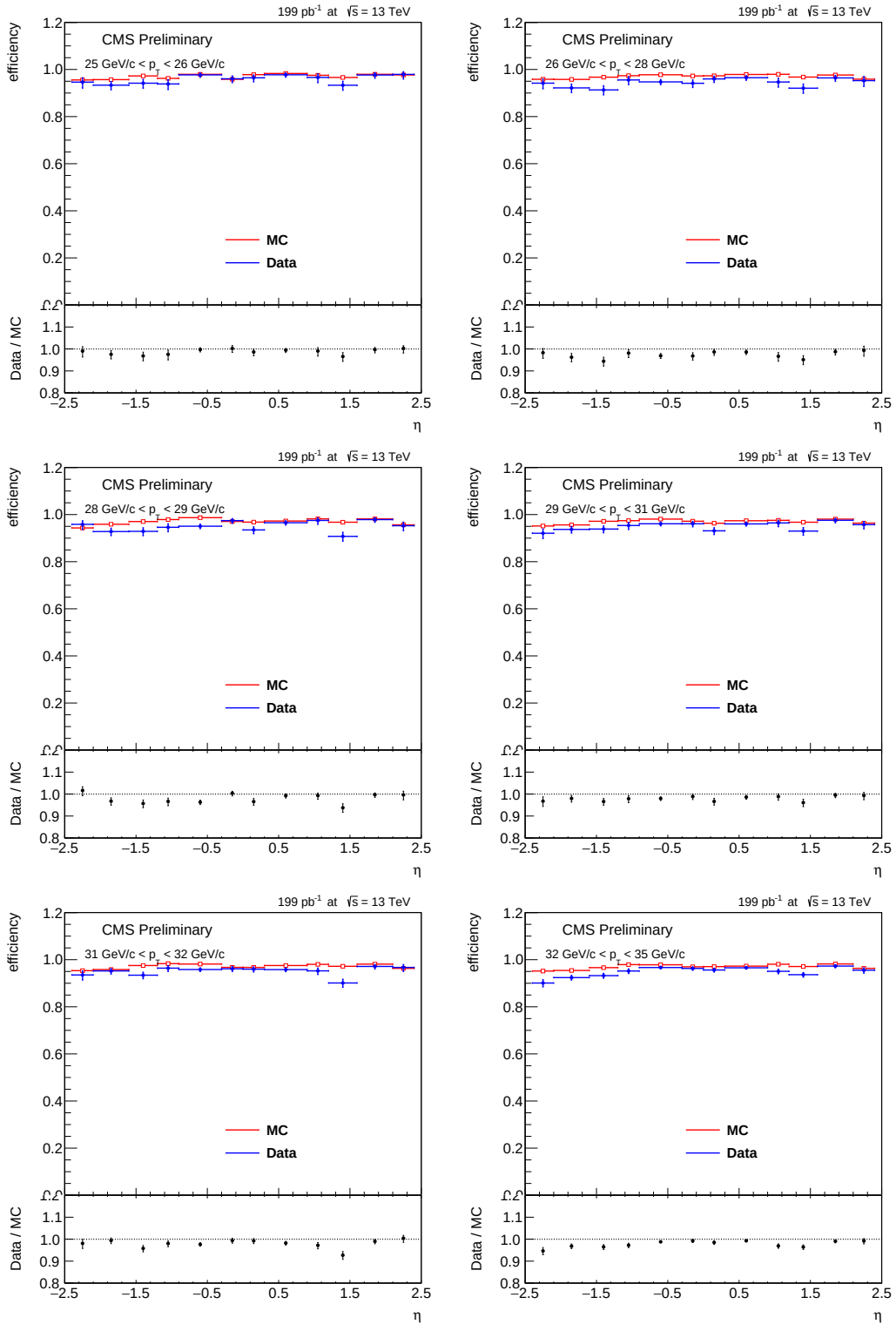

Figure A-7: η dependence of Single muon trigger efficiency scale factors, separated by p_T bins, for negatively charged muons in the 13 TeV samples.

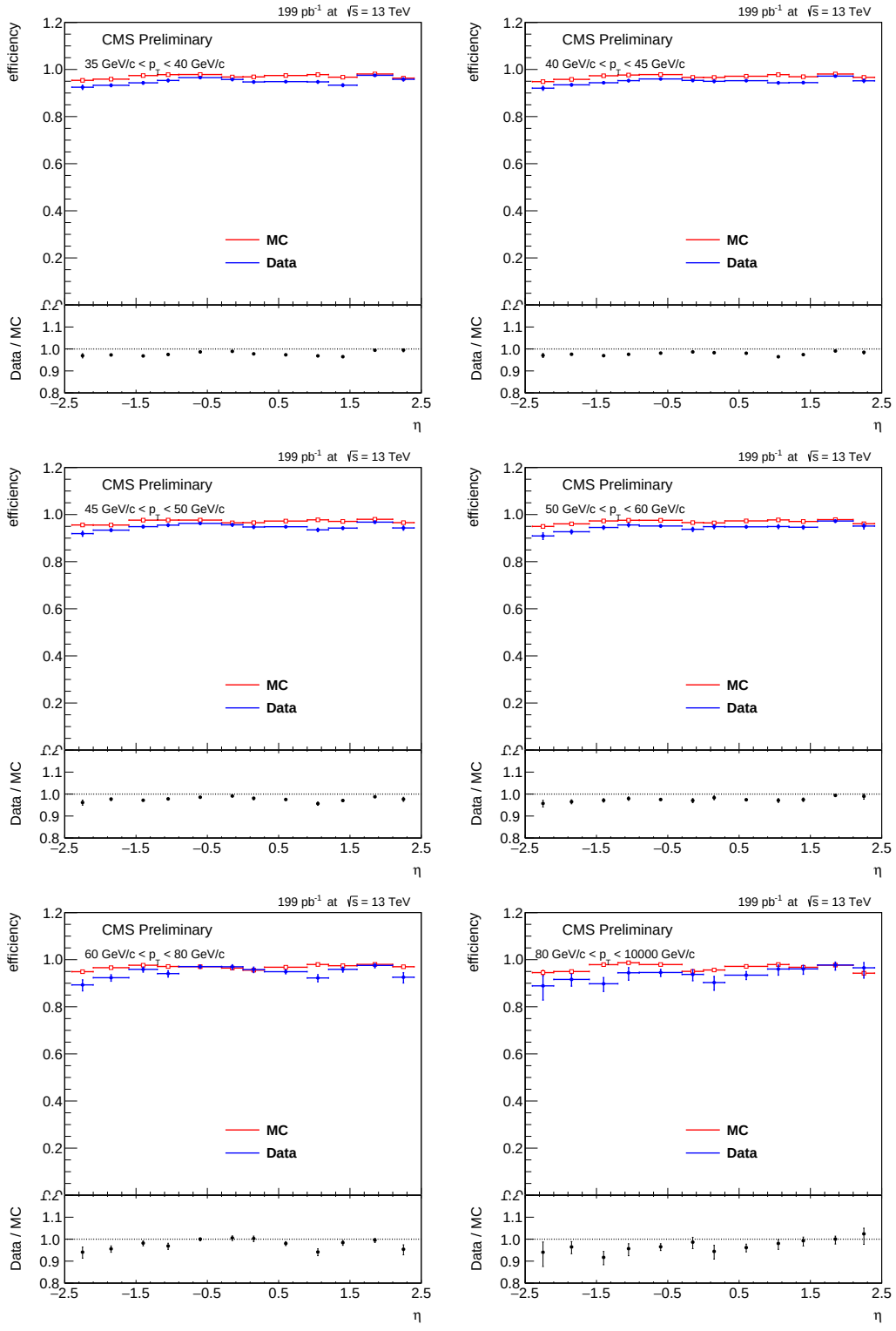

Figure A-7: η dependence of Single muon trigger efficiency scale factors, separated by p_T bins, for negatively charged muons in the 13 TeV samples.

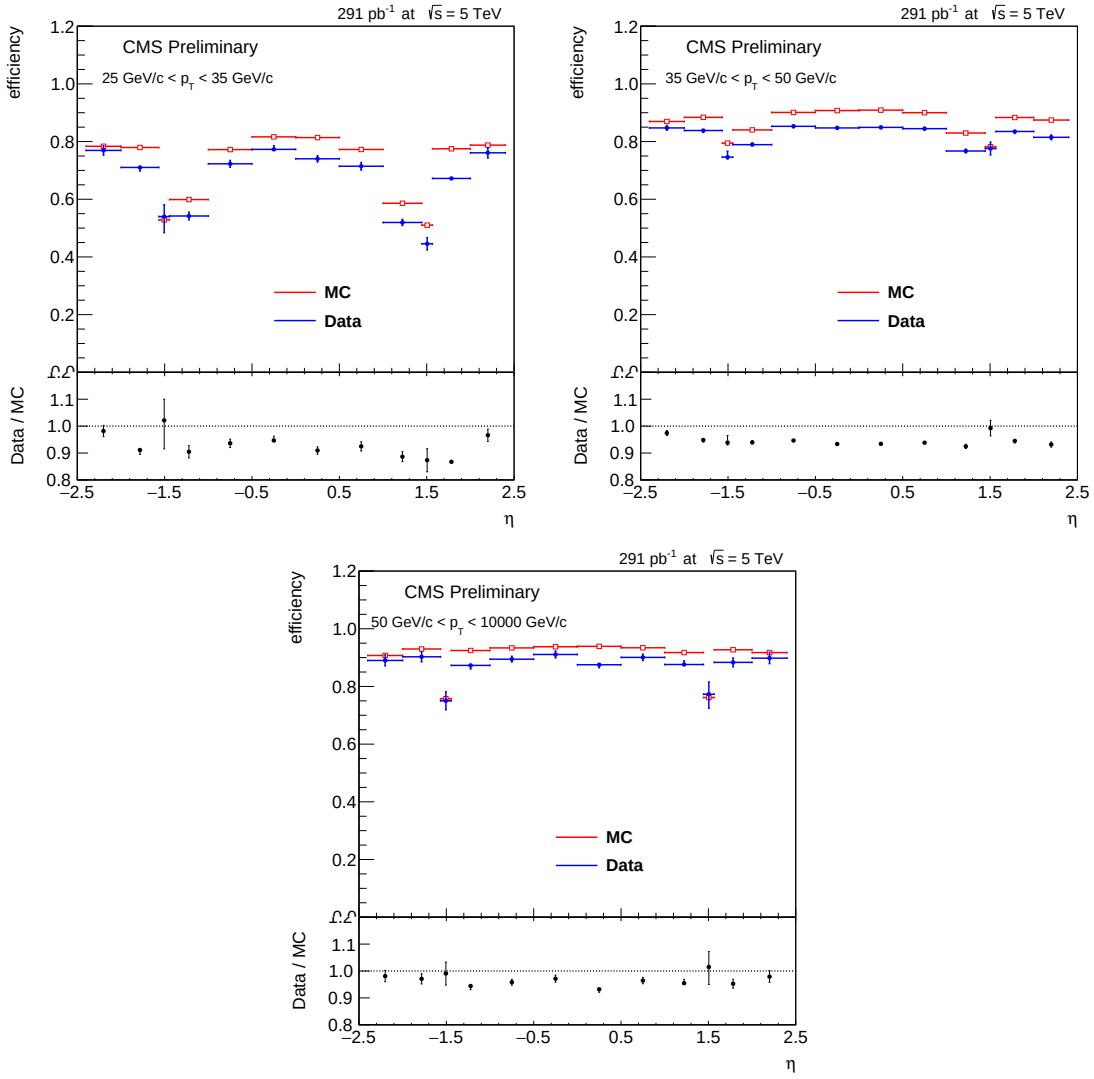

Figure A-8: η dependence of GSF electron identification and isolation efficiency scale factors, separated by p_T bins, for combined charged electrons in the 5 TeV samples.

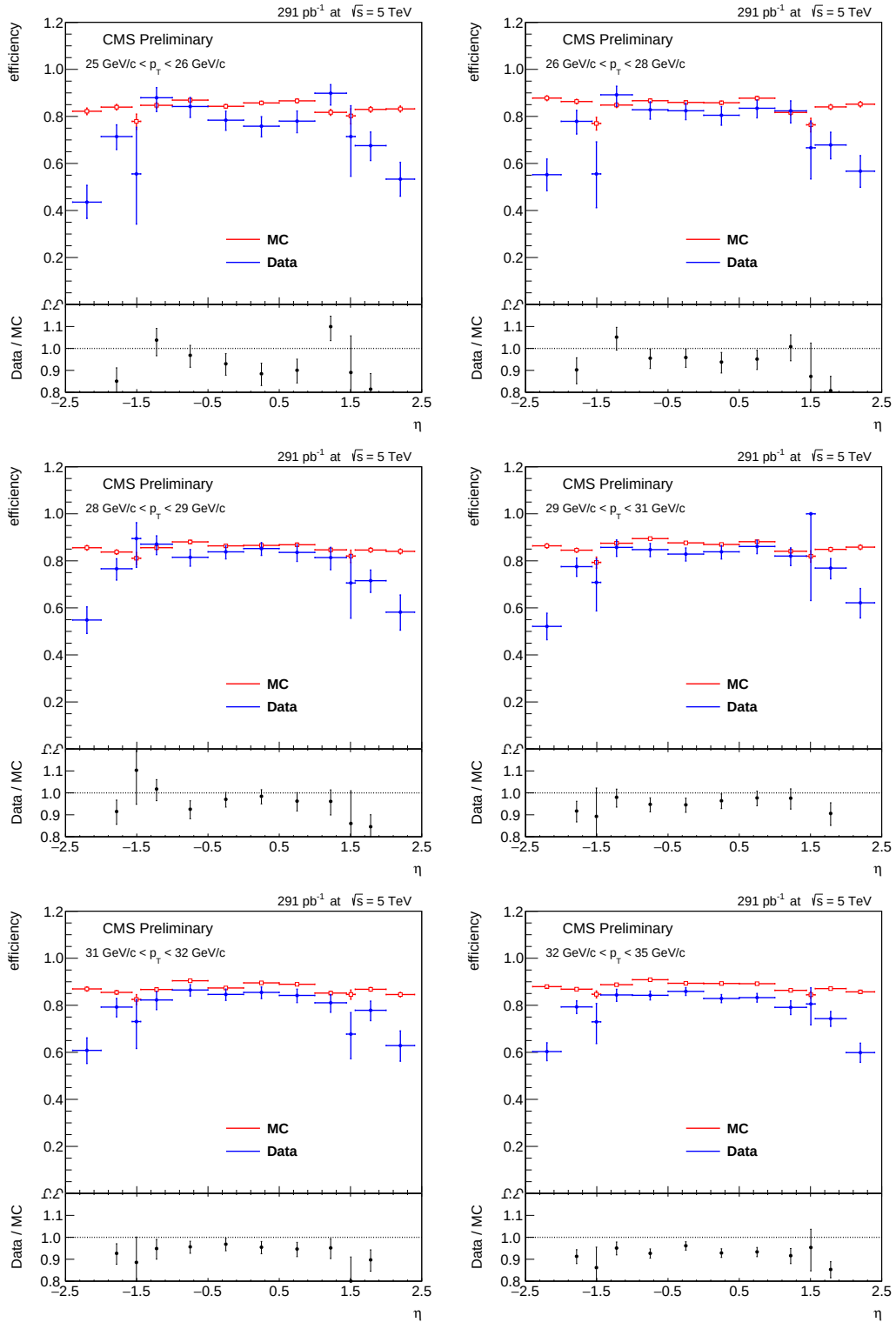

Figure A-9: η dependence of Single electron trigger efficiency scale factors, separated by p_T bins, for positively charged electrons in the 5 TeV samples.

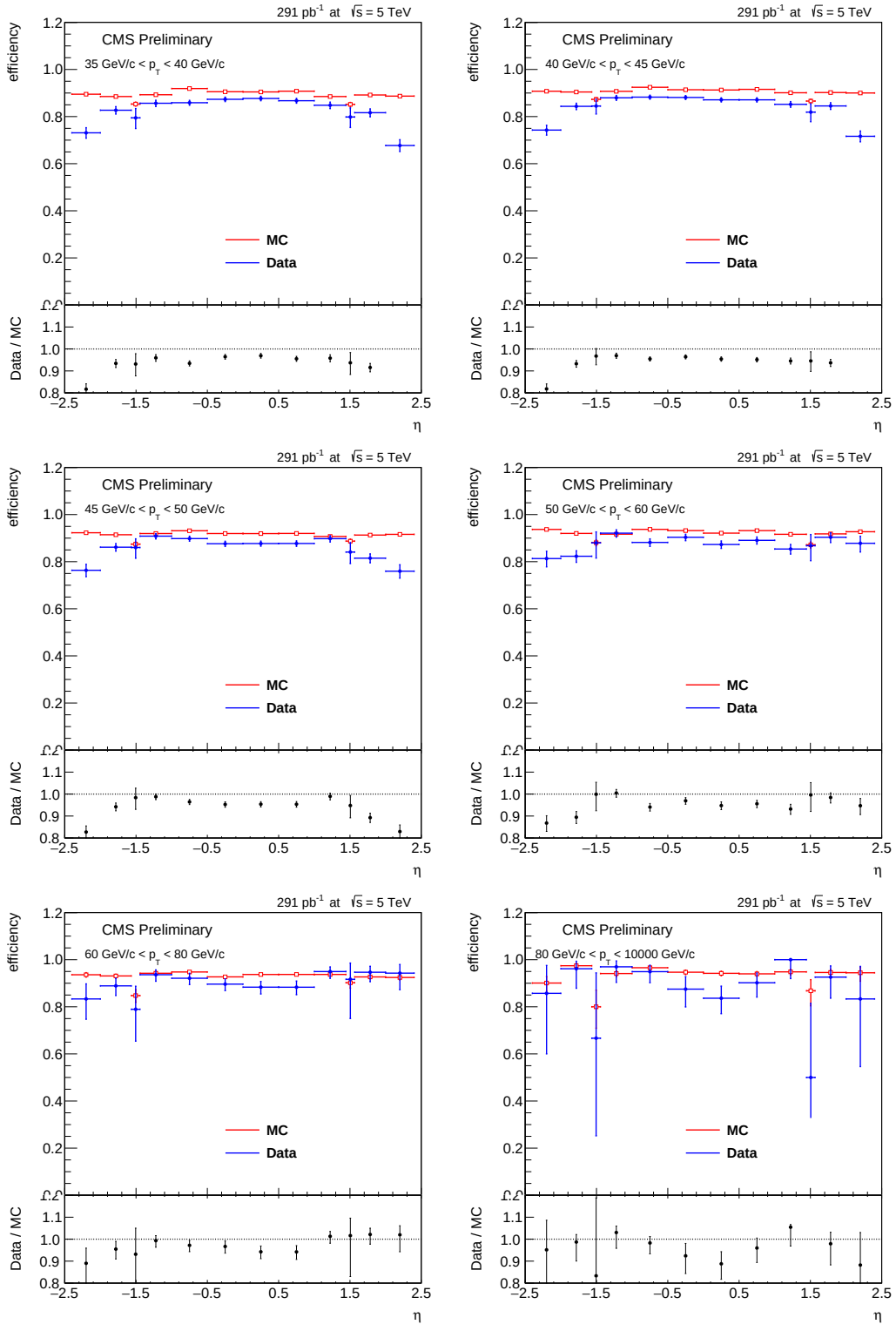

Figure A-9: η dependence of Single electron trigger efficiency scale factors, separated by p_T bins, for positively charged electrons in the 5 TeV samples.

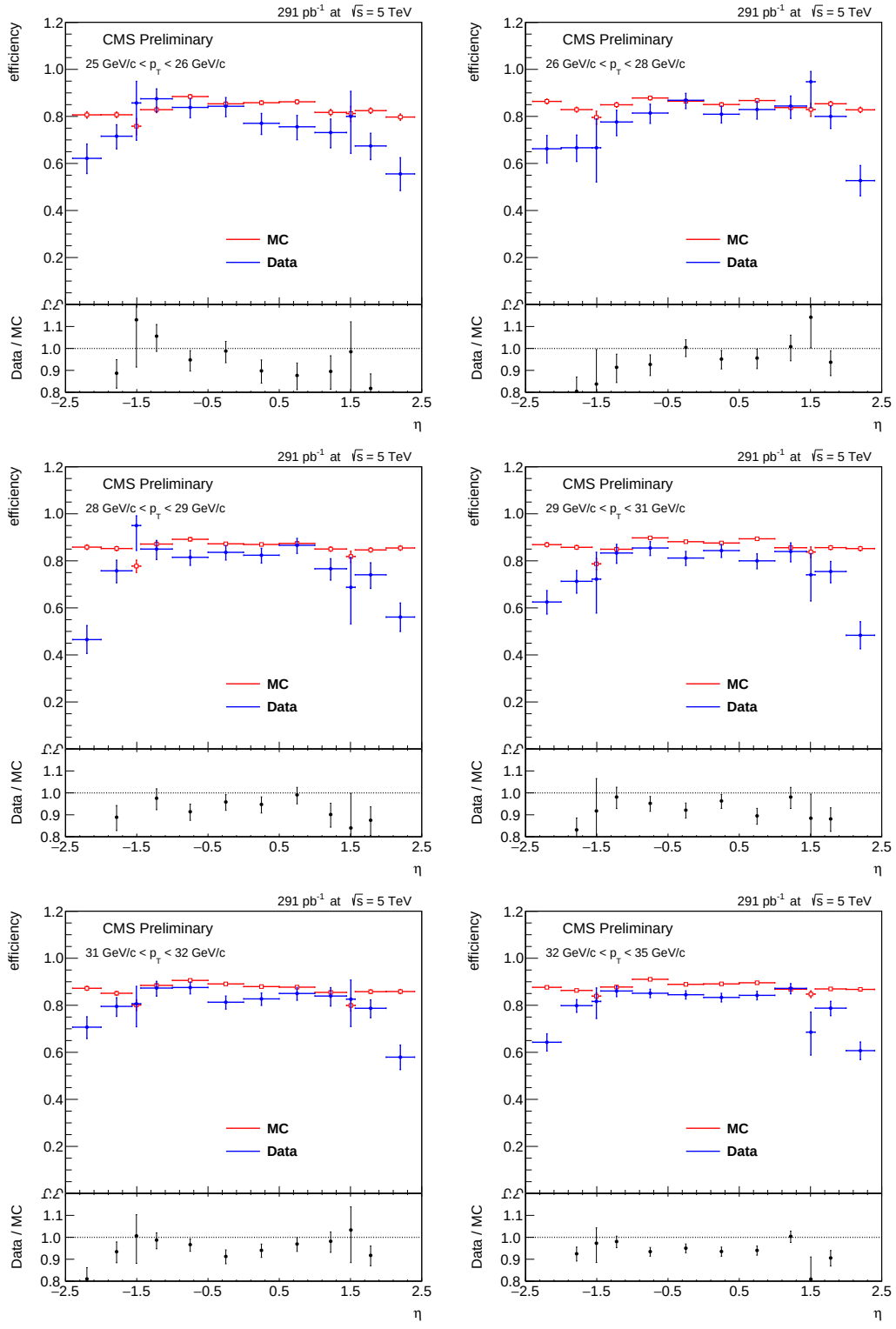

Figure A-10: η dependence of Single electron trigger efficiency scale factors, separated by p_T bins, for negatively charged electrons in the 5 TeV samples.

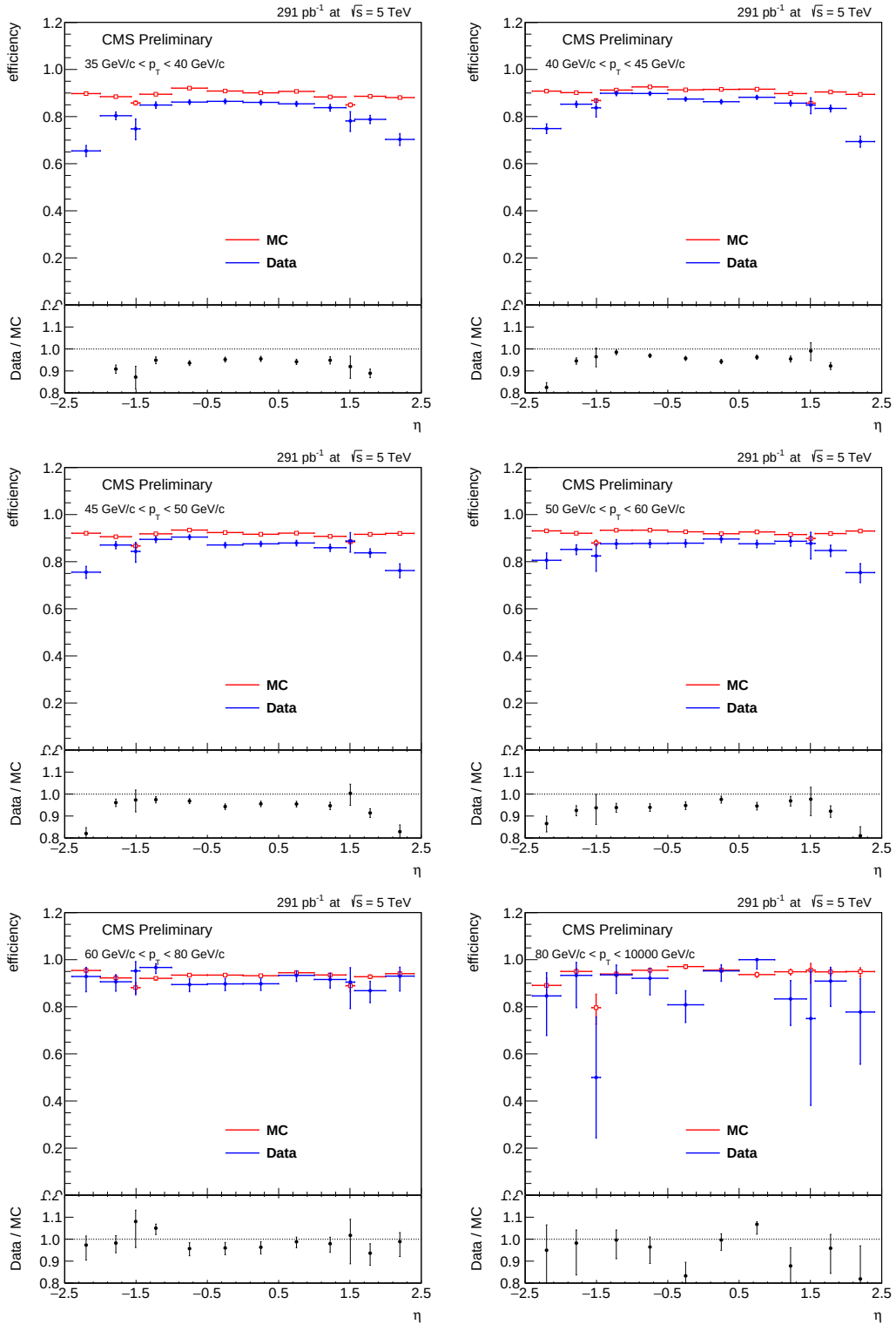

Figure A-10: η dependence of Single electron trigger efficiency scale factors, separated by p_T bins, for negatively charged electrons in the 5 TeV samples.

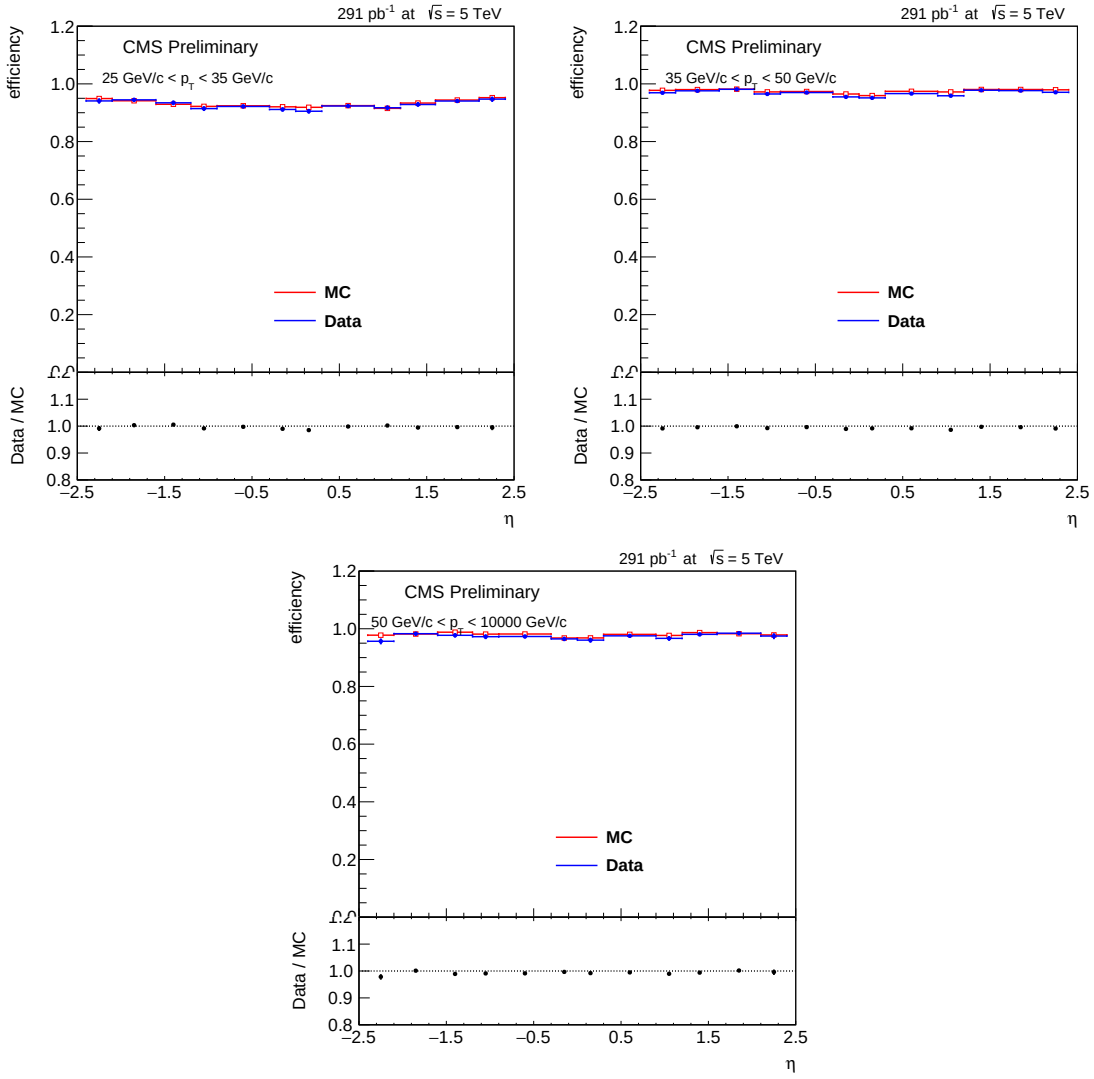

Figure A-11: η dependence of Muon selection efficiency scale factors, separated by p_T bins, for combined charged muons in the 5 TeV samples.

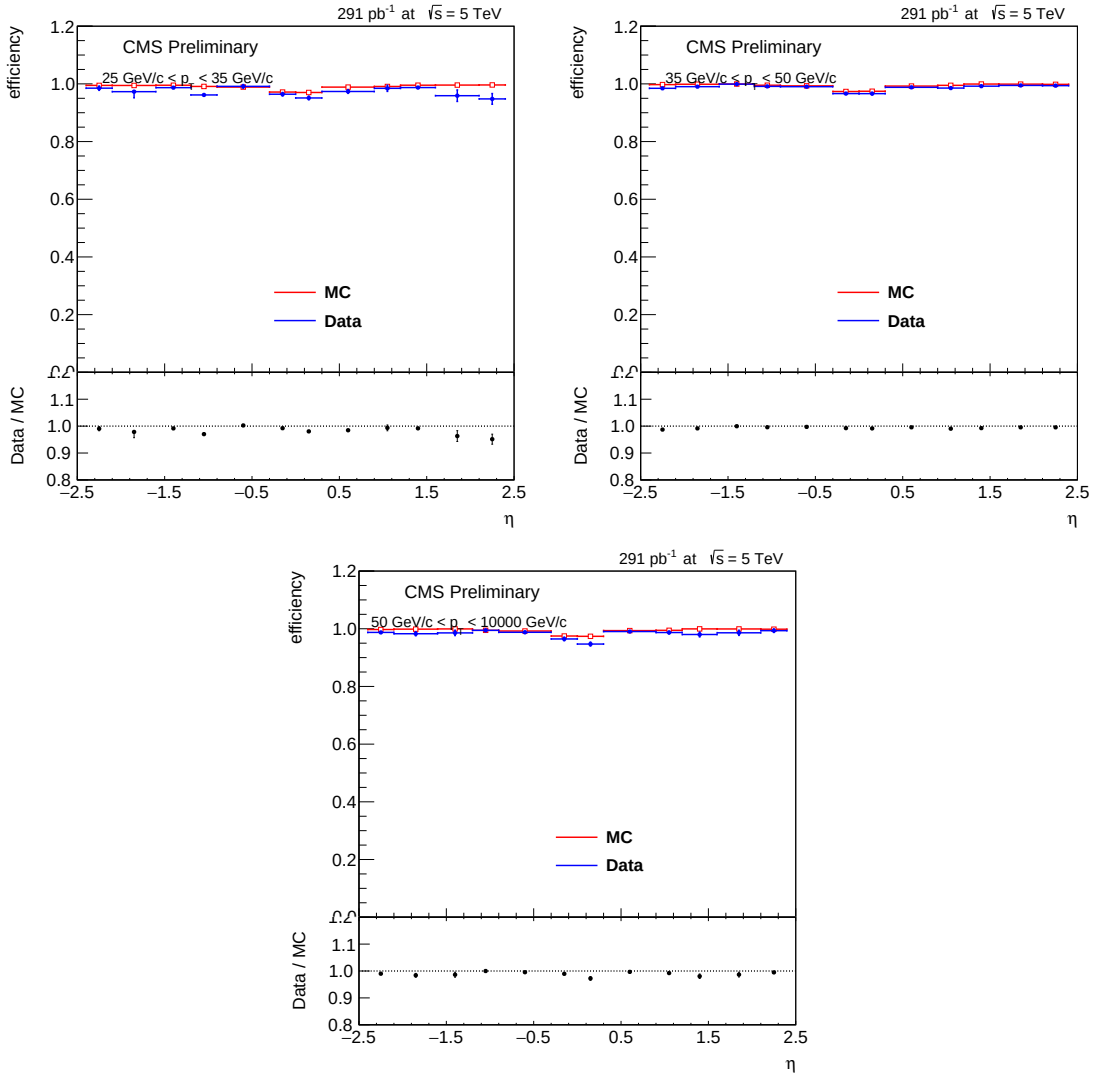

Figure A-12: η dependence of Standalone muon identification efficiency scale factors, separated by p_T bins, for combined charged muons in the 5 TeV samples.

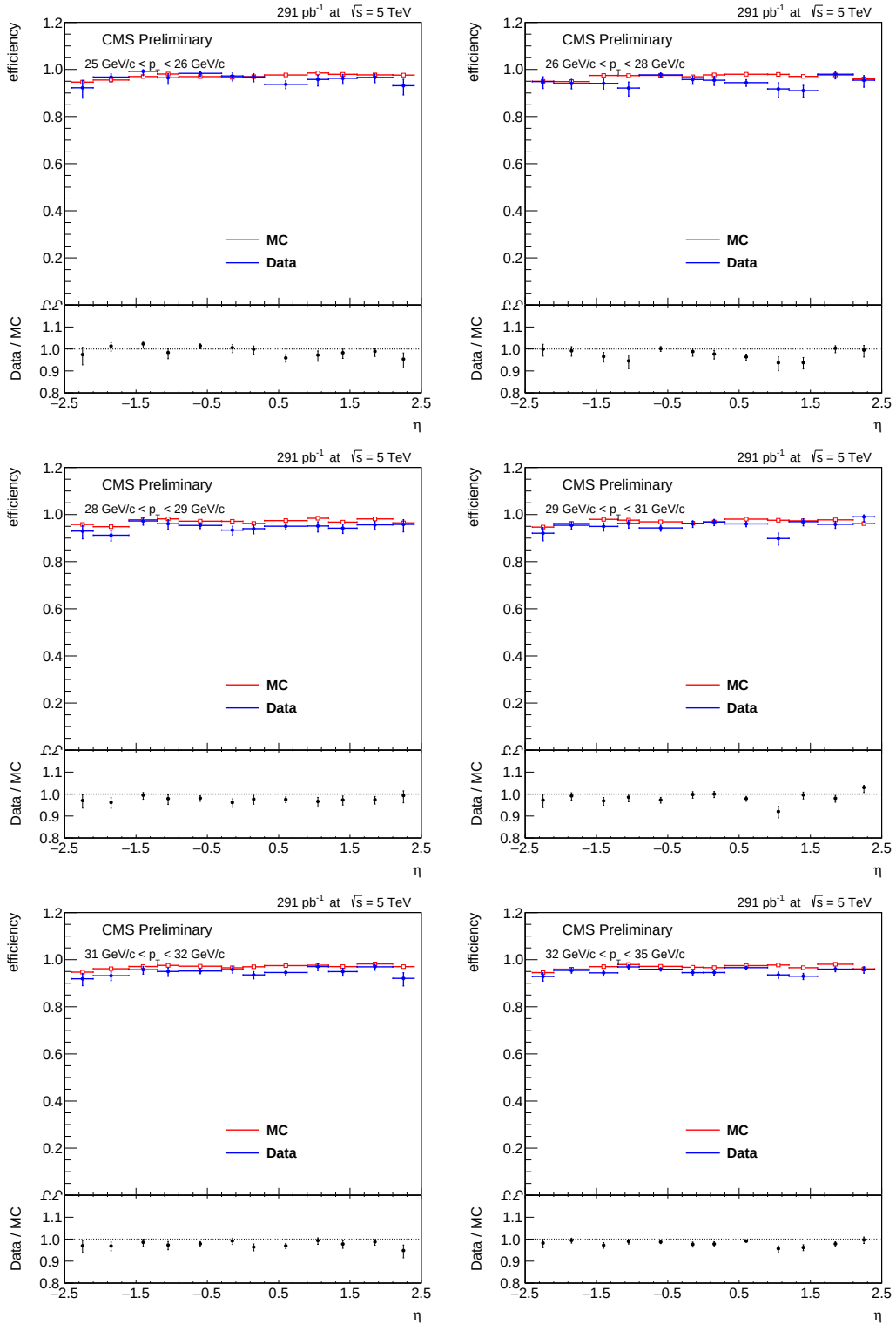

Figure A-13: η dependence of Single muon trigger efficiency scale factors, separated by p_T bins, for positively charged muons in the 5 TeV samples.

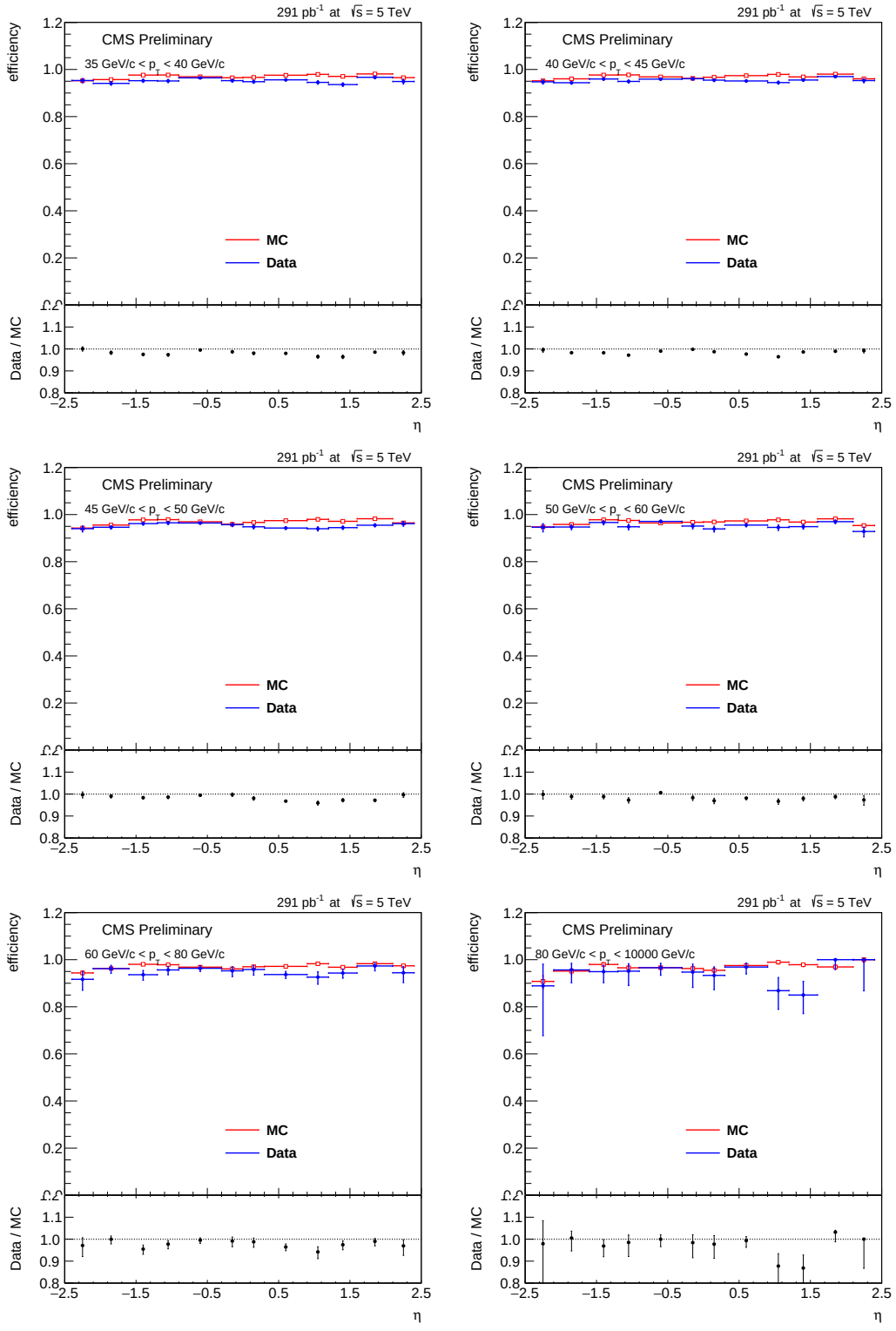

Figure A-13: η dependence of Single muon trigger efficiency scale factors, separated by p_T bins, for positively charged muons in the 5 TeV samples.

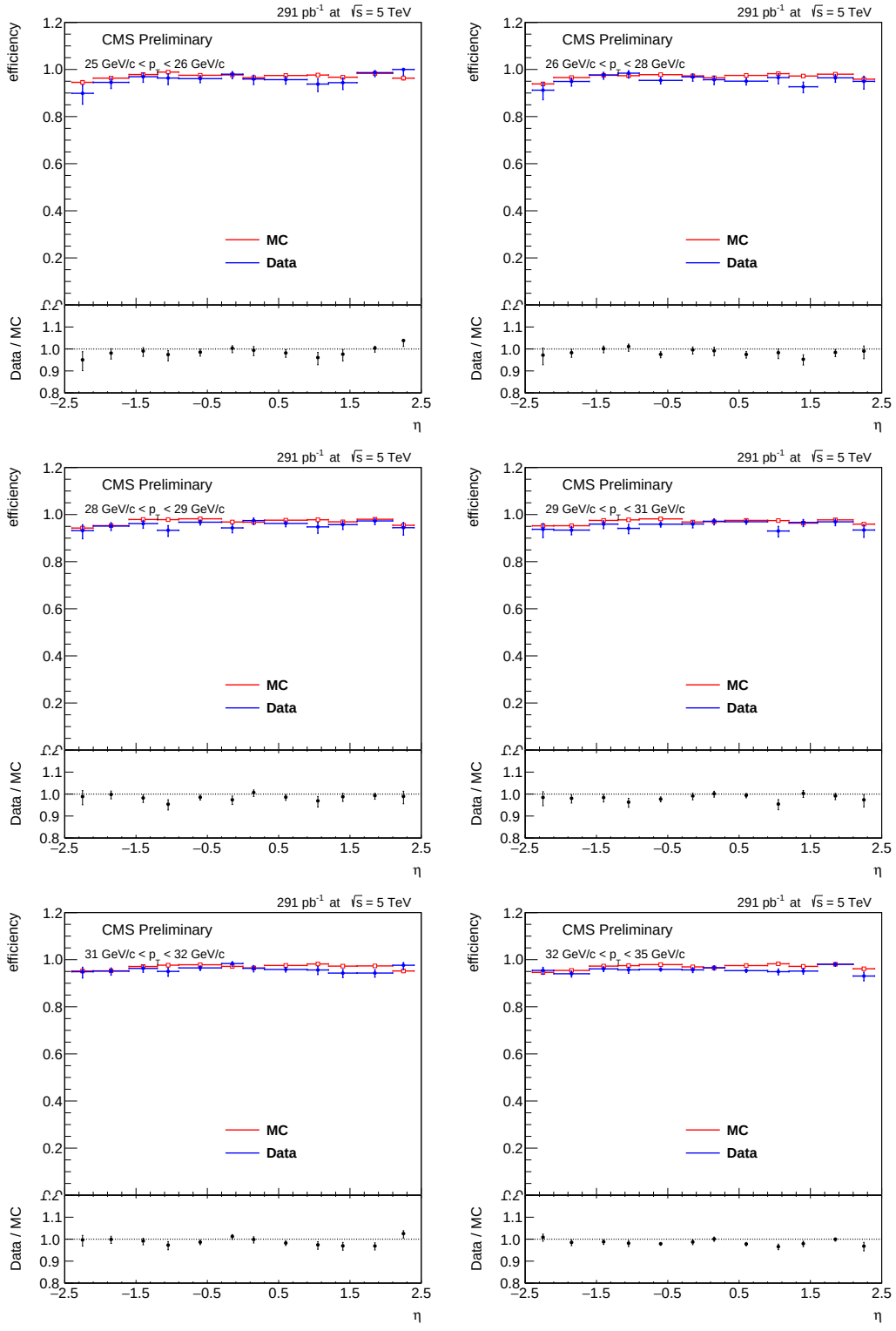

Figure A-14: η dependence of Single muon trigger efficiency scale factors, separated by p_{T} bins, for negatively charged muons in the 5 TeV samples.

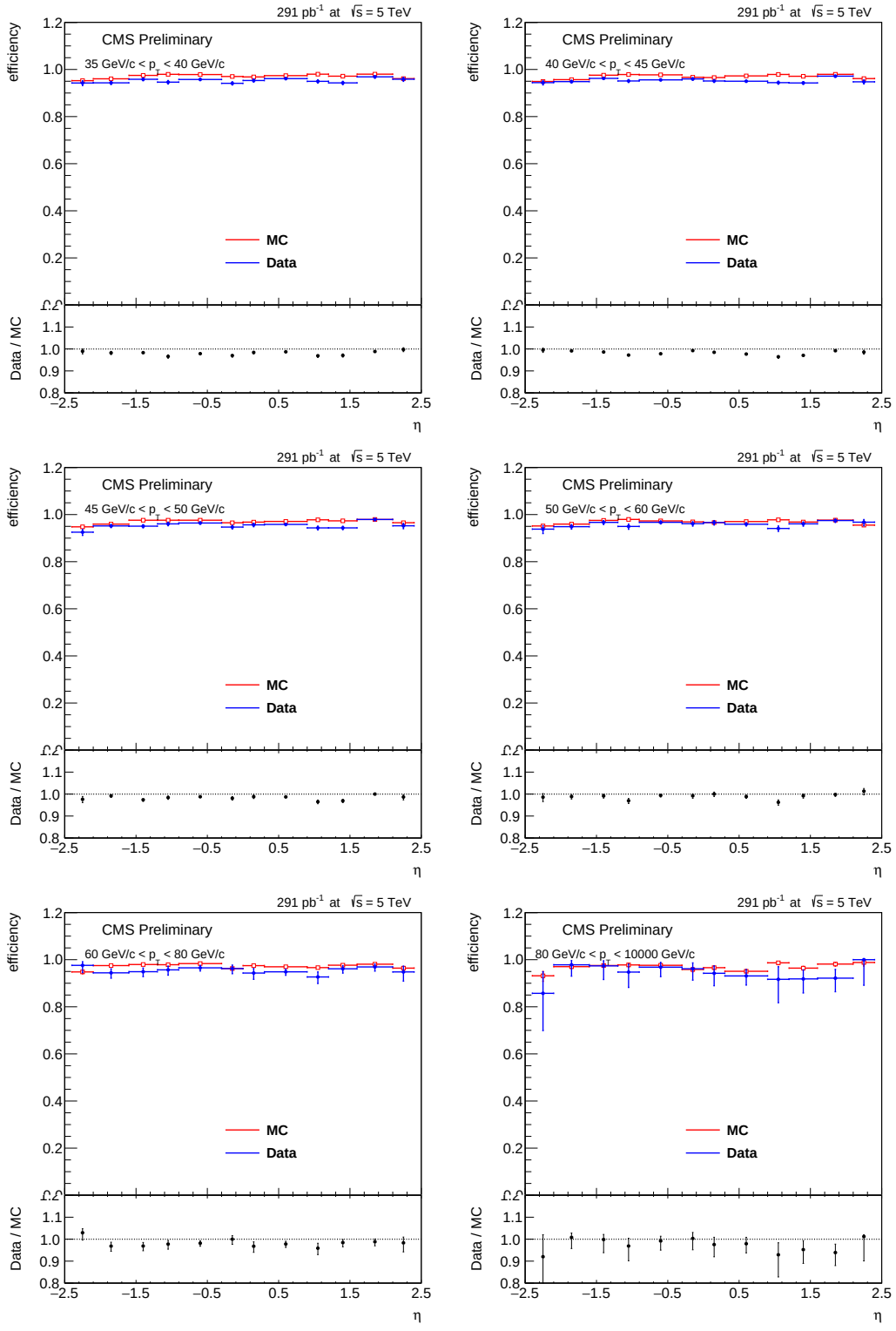

Figure A-14: η dependence of Single muon trigger efficiency scale factors, separated by p_T bins, for negatively charged muons in the 5 TeV samples.

	$-2.4 < \eta < -2$	$-2 < \eta < -1.566$	$-1.566 < \eta < -1.4442$	$-1.4442 < \eta < -1$	$-1 < \eta < -0.5$	$-0.5 < \eta < 0$
$25 < p_T < 26.5$	0.664 ± 0.058	0.921 ± 0.054	0.959 ± 0.112	1.053 ± 0.046	0.964 ± 0.036	1.031 ± 0.030
$26.5 < p_T < 28$	0.646 ± 0.056	0.928 ± 0.043	1.033 ± 0.103	0.976 ± 0.041	0.962 ± 0.031	0.933 ± 0.032
$28 < p_T < 29.5$	0.754 ± 0.055	0.986 ± 0.037	1.004 ± 0.101	1.016 ± 0.037	0.948 ± 0.030	0.977 ± 0.025
$29.5 < p_T < 31$	0.624 ± 0.048	0.959 ± 0.034	0.981 ± 0.093	0.990 ± 0.034	0.961 ± 0.027	0.987 ± 0.022
$31 < p_T < 32.5$	0.725 ± 0.042	0.907 ± 0.036	0.942 ± 0.078	1.037 ± 0.028	0.996 ± 0.020	0.991 ± 0.020
$32.5 < p_T < 35$	0.747 ± 0.032	0.959 ± 0.023	0.972 ± 0.065	0.976 ± 0.022	0.979 ± 0.014	0.971 ± 0.014
$35 < p_T < 40$	0.811 ± 0.020	0.957 ± 0.014	0.987 ± 0.038	0.995 ± 0.011	0.982 ± 0.008	0.991 ± 0.008
$40 < p_T < 45$	0.831 ± 0.018	0.986 ± 0.011	0.976 ± 0.029	0.996 ± 0.009	0.999 ± 0.006	0.978 ± 0.007
$45 < p_T < 50$	0.875 ± 0.020	0.966 ± 0.013	1.030 ± 0.033	0.985 ± 0.011	0.984 ± 0.008	0.980 ± 0.008
$50 < p_T < 60$	0.857 ± 0.026	0.986 ± 0.015	0.988 ± 0.048	1.008 ± 0.012	0.989 ± 0.009	0.988 ± 0.010
$60 < p_T < 80$	0.889 ± 0.035	0.998 ± 0.024	1.051 ± 0.056	0.993 ± 0.018	0.992 ± 0.014	0.974 ± 0.016
$80 < p_T < 1e+04$	1.033 ± 0.039	0.978 ± 0.036	1.009 ± 0.105	0.996 ± 0.027	0.976 ± 0.025	0.980 ± 0.026
	$0 < \eta < 0.5$	$0.5 < \eta < 1$	$1 < \eta < 1.44$	$1.44 < \eta < 1.57$	$1.57 < \eta < 2$	$2 < \eta < 2.4$
$25 < p_T < 26.5$	0.952 ± 0.035	0.940 ± 0.036	1.088 ± 0.039	1.052 ± 0.134	0.871 ± 0.048	0.658 ± 0.067
$26.5 < p_T < 28$	1.005 ± 0.030	0.958 ± 0.033	0.989 ± 0.043	1.082 ± 0.131	0.898 ± 0.044	0.800 ± 0.059
$28 < p_T < 29.5$	0.980 ± 0.026	0.995 ± 0.026	0.964 ± 0.046	0.872 ± 0.126	0.968 ± 0.039	0.622 ± 0.056
$29.5 < p_T < 31$	0.992 ± 0.021	0.964 ± 0.025	0.939 ± 0.040	1.000 ± 0.105	0.935 ± 0.036	0.751 ± 0.049
$31 < p_T < 32.5$	0.980 ± 0.020	0.976 ± 0.021	1.025 ± 0.029	1.010 ± 0.085	0.923 ± 0.035	0.666 ± 0.053
$32.5 < p_T < 35$	0.976 ± 0.014	0.970 ± 0.014	1.016 ± 0.021	0.807 ± 0.083	0.946 ± 0.023	0.805 ± 0.032
$35 < p_T < 40$	0.972 ± 0.008	0.976 ± 0.008	0.993 ± 0.011	0.975 ± 0.037	0.963 ± 0.014	0.814 ± 0.021
$40 < p_T < 45$	0.978 ± 0.007	0.987 ± 0.007	0.991 ± 0.009	1.022 ± 0.031	0.974 ± 0.011	0.846 ± 0.019
$45 < p_T < 50$	0.973 ± 0.008	0.986 ± 0.008	0.997 ± 0.011	0.963 ± 0.040	0.952 ± 0.013	0.866 ± 0.022
$50 < p_T < 60$	0.998 ± 0.009	0.980 ± 0.010	1.019 ± 0.012	0.995 ± 0.043	0.968 ± 0.016	0.907 ± 0.026
$60 < p_T < 80$	0.970 ± 0.017	0.987 ± 0.014	1.016 ± 0.017	0.937 ± 0.074	0.989 ± 0.023	0.956 ± 0.035
$80 < p_T < 1e+04$	0.982 ± 0.022	0.978 ± 0.027	1.048 ± 0.017	1.096 ± 0.082	0.950 ± 0.043	0.967 ± 0.055

Table A.3: Single electron trigger efficiency scale factors in (p_T, η) bins for positively charged electrons in the 13 TeV samples.

	$-2.4 < \eta < -2$	$-2 < \eta < -1.566$	$-1.566 < \eta < -1.4442$	$-1.4442 < \eta < -1$	$-1 < \eta < -0.5$	$-0.5 < \eta < 0$
$25 < p_T < 26.5$	0.722 ± 0.059	0.895 ± 0.053	0.909 ± 0.133	0.992 ± 0.050	0.965 ± 0.034	0.996 ± 0.032
$26.5 < p_T < 28$	0.736 ± 0.060	0.922 ± 0.047	0.920 ± 0.141	1.002 ± 0.040	1.005 ± 0.029	0.963 ± 0.028
$28 < p_T < 29.5$	0.746 ± 0.052	0.897 ± 0.043	0.965 ± 0.117	1.034 ± 0.031	0.971 ± 0.027	0.972 ± 0.025
$29.5 < p_T < 31$	0.716 ± 0.049	0.953 ± 0.033	0.890 ± 0.095	0.994 ± 0.030	0.970 ± 0.024	0.971 ± 0.022
$31 < p_T < 32.5$	0.745 ± 0.044	0.921 ± 0.034	1.023 ± 0.107	1.060 ± 0.026	1.006 ± 0.020	0.980 ± 0.021
$32.5 < p_T < 35$	0.814 ± 0.033	0.977 ± 0.024	0.989 ± 0.062	1.001 ± 0.018	0.984 ± 0.014	0.972 ± 0.015
$35 < p_T < 40$	0.768 ± 0.020	0.955 ± 0.014	0.989 ± 0.039	0.978 ± 0.012	0.985 ± 0.007	0.968 ± 0.008
$40 < p_T < 45$	0.826 ± 0.018	0.977 ± 0.011	0.940 ± 0.038	1.003 ± 0.009	0.986 ± 0.007	0.984 ± 0.007
$45 < p_T < 50$	0.879 ± 0.021	0.974 ± 0.012	1.012 ± 0.037	0.988 ± 0.011	0.991 ± 0.008	0.997 ± 0.008
$50 < p_T < 60$	0.900 ± 0.025	1.005 ± 0.014	1.038 ± 0.037	1.014 ± 0.011	0.996 ± 0.009	0.982 ± 0.010
$60 < p_T < 80$	0.869 ± 0.038	0.954 ± 0.025	0.846 ± 0.089	1.022 ± 0.017	0.995 ± 0.014	0.982 ± 0.015
$80 < p_T < 1e+04$	0.983 ± 0.055	1.005 ± 0.026	0.941 ± 0.134	0.945 ± 0.038	0.982 ± 0.025	0.996 ± 0.022
	$0 < \eta < 0.5$	$0.5 < \eta < 1$	$1 < \eta < 1.44$	$1.44 < \eta < 1.57$	$1.57 < \eta < 2$	$2 < \eta < 2.4$
$25 < p_T < 26.5$	0.955 ± 0.037	0.969 ± 0.035	0.967 ± 0.050	0.999 ± 0.136	0.911 ± 0.050	0.703 ± 0.068
$26.5 < p_T < 28$	0.971 ± 0.031	1.033 ± 0.033	1.010 ± 0.043	0.958 ± 0.118	0.902 ± 0.044	0.673 ± 0.059
$28 < p_T < 29.5$	0.973 ± 0.026	0.987 ± 0.025	1.020 ± 0.038	0.994 ± 0.102	0.978 ± 0.038	0.815 ± 0.053
$29.5 < p_T < 31$	0.945 ± 0.025	0.946 ± 0.027	1.020 ± 0.034	0.978 ± 0.121	0.886 ± 0.037	0.701 ± 0.055
$31 < p_T < 32.5$	0.999 ± 0.021	0.979 ± 0.021	1.015 ± 0.033	0.927 ± 0.110	0.982 ± 0.032	0.781 ± 0.048
$32.5 < p_T < 35$	0.963 ± 0.015	0.992 ± 0.015	1.014 ± 0.020	1.008 ± 0.061	0.973 ± 0.021	0.764 ± 0.033
$35 < p_T < 40$	0.975 ± 0.008	0.975 ± 0.008	1.002 ± 0.011	0.963 ± 0.039	0.957 ± 0.013	0.824 ± 0.021
$40 < p_T < 45$	0.983 ± 0.007	0.979 ± 0.007	0.989 ± 0.009	1.019 ± 0.029	0.964 ± 0.011	0.864 ± 0.018
$45 < p_T < 50$	0.978 ± 0.008	0.980 ± 0.008	0.984 ± 0.012	1.035 ± 0.036	0.969 ± 0.013	0.829 ± 0.023
$50 < p_T < 60$	0.986 ± 0.010	0.999 ± 0.010	1.008 ± 0.012	1.015 ± 0.042	0.962 ± 0.016	0.913 ± 0.024
$60 < p_T < 80$	0.984 ± 0.014	1.015 ± 0.014	1.017 ± 0.017	1.056 ± 0.059	0.949 ± 0.022	0.905 ± 0.038
$80 < p_T < 1e+04$	0.962 ± 0.028	1.005 ± 0.021	1.032 ± 0.026	1.204 ± 0.154	1.008 ± 0.033	0.867 ± 0.092

Table A.4: Single electron trigger efficiency scale factors in (p_T, η) bins for negatively charged electrons in the 13 TeV samples.

	$-2.4 < \eta < -2.1$	$-2.1 < \eta < -1.6$	$-1.6 < \eta < -1.2$	$-1.2 < \eta < -0.9$	$-0.9 < \eta < -0.3$	$-0.3 < \eta < 0$
$25 < p_T < 35$	0.993 ± 0.006	1.009 ± 0.005	0.998 ± 0.006	1.002 ± 0.007	0.993 ± 0.004	0.985 ± 0.005
$35 < p_T < 50$	0.987 ± 0.003	0.996 ± 0.002	0.998 ± 0.002	0.990 ± 0.002	0.993 ± 0.002	0.988 ± 0.002
$50 < p_T < 1e+04$	0.975 ± 0.007	0.992 ± 0.007	0.997 ± 0.003	0.992 ± 0.005	0.993 ± 0.003	0.992 ± 0.005
	$0 < \eta < 0.3$	$0.3 < \eta < 0.9$	$0.9 < \eta < 1.2$	$1.2 < \eta < 1.6$	$1.6 < \eta < 2.1$	$2.1 < \eta < 2.4$
$25 < p_T < 35$	0.989 ± 0.006	0.992 ± 0.004	0.984 ± 0.007	0.999 ± 0.006	1.005 ± 0.005	1.003 ± 0.006
$35 < p_T < 50$	0.995 ± 0.003	0.992 ± 0.002	0.988 ± 0.002	0.997 ± 0.002	1.002 ± 0.001	0.994 ± 0.002
$50 < p_T < 1e+04$	0.979 ± 0.005	0.992 ± 0.003	0.994 ± 0.005	0.987 ± 0.003	0.997 ± 0.003	0.989 ± 0.006

Table A.5: Muon selection efficiency scale factors in (p_T, η) bins for combined charged muons in the 13 TeV samples.

	$-2.4 < \eta < -2.1$	$-2.1 < \eta < -1.6$	$-1.6 < \eta < -1.2$	$-1.2 < \eta < -0.9$	$-0.9 < \eta < -0.3$	$-0.3 < \eta < 0$
$25 < p_T < 35$	0.990 ± 0.007	0.991 ± 0.004	0.986 ± 0.006	0.997 ± 0.034	0.992 ± 0.009	0.991 ± 0.014
$35 < p_T < 50$	0.994 ± 0.002	0.996 ± 0.002	0.998 ± 0.002	0.997 ± 0.002	0.998 ± 0.001	0.986 ± 0.002
$50 < p_T < 1e+04$	0.996 ± 0.013	0.995 ± 0.004	0.995 ± 0.004	0.995 ± 0.005	0.997 ± 0.003	0.989 ± 0.005
	$0 < \eta < 0.3$	$0.3 < \eta < 0.9$	$0.9 < \eta < 1.2$	$1.2 < \eta < 1.6$	$1.6 < \eta < 2.1$	$2.1 < \eta < 2.4$
$25 < p_T < 35$	0.983 ± 0.006	0.988 ± 0.014	1.008 ± 0.017	1.009 ± 0.005	1.004 ± 0.008	0.994 ± 0.001
$35 < p_T < 50$	0.988 ± 0.002	0.991 ± 0.002	0.995 ± 0.000	0.998 ± 0.002	0.998 ± 0.002	0.996 ± 0.001
$50 < p_T < 1e+04$	0.981 ± 0.005	0.988 ± 0.003	0.995 ± 0.004	0.995 ± 0.004	0.997 ± 0.003	0.992 ± 0.005

Table A.6: Standalone muon identification efficiency scale factors in (p_T, η) bins for combined charged muons in the 13 TeV samples.

	$-2.4 < \eta < -2.1$	$-2.1 < \eta < -1.6$	$-1.6 < \eta < -1.2$	$-1.2 < \eta < -0.9$	$-0.9 < \eta < -0.3$	$-0.3 < \eta < 0$
$25 < p_T < 26.5$	0.960 ± 0.030	0.999 ± 0.017	0.928 ± 0.023	0.984 ± 0.021	0.981 ± 0.012	0.981 ± 0.017
$26.5 < p_T < 28$	0.984 ± 0.023	0.984 ± 0.016	0.967 ± 0.016	0.978 ± 0.019	0.988 ± 0.011	0.976 ± 0.016
$28 < p_T < 29.5$	0.974 ± 0.023	0.965 ± 0.017	0.987 ± 0.014	0.987 ± 0.015	0.987 ± 0.010	0.985 ± 0.013
$29.5 < p_T < 31$	0.946 ± 0.025	0.971 ± 0.015	0.975 ± 0.015	0.973 ± 0.016	0.977 ± 0.010	1.013 ± 0.010
$31 < p_T < 32.5$	0.974 ± 0.020	0.993 ± 0.013	0.964 ± 0.014	0.979 ± 0.015	0.986 ± 0.008	0.980 ± 0.013
$32.5 < p_T < 35$	0.979 ± 0.014	0.969 ± 0.011	0.967 ± 0.011	0.984 ± 0.009	0.993 ± 0.006	0.982 ± 0.009
$35 < p_T < 40$	0.988 ± 0.009	0.978 ± 0.006	0.963 ± 0.006	0.973 ± 0.006	0.986 ± 0.004	0.991 ± 0.005
$40 < p_T < 45$	0.970 ± 0.009	0.972 ± 0.006	0.963 ± 0.005	0.972 ± 0.005	0.986 ± 0.003	0.990 ± 0.005
$45 < p_T < 50$	0.947 ± 0.012	0.980 ± 0.006	0.968 ± 0.006	0.967 ± 0.007	0.986 ± 0.004	0.989 ± 0.007
$50 < p_T < 60$	0.971 ± 0.014	0.984 ± 0.009	0.976 ± 0.007	0.971 ± 0.008	0.972 ± 0.006	0.992 ± 0.009
$60 < p_T < 80$	1.004 ± 0.023	0.979 ± 0.014	0.962 ± 0.013	0.973 ± 0.014	0.988 ± 0.009	0.983 ± 0.013
$80 < p_T < 1e+04$	0.951 ± 0.082	1.010 ± 0.026	0.949 ± 0.026	0.901 ± 0.034	0.953 ± 0.020	0.966 ± 0.025
	$0 < \eta < 0.3$	$0.3 < \eta < 0.9$	$0.9 < \eta < 1.2$	$1.2 < \eta < 1.6$	$1.6 < \eta < 2.1$	$2.1 < \eta < 2.4$
$25 < p_T < 26.5$	0.955 ± 0.020	0.981 ± 0.012	0.979 ± 0.020	0.960 ± 0.020	1.007 ± 0.011	0.993 ± 0.023
$26.5 < p_T < 28$	1.004 ± 0.014	0.963 ± 0.012	0.958 ± 0.021	0.944 ± 0.021	1.001 ± 0.012	0.988 ± 0.023
$28 < p_T < 29.5$	0.997 ± 0.013	0.966 ± 0.011	0.984 ± 0.014	0.987 ± 0.015	0.985 ± 0.012	0.972 ± 0.021
$29.5 < p_T < 31$	0.979 ± 0.013	0.964 ± 0.010	0.939 ± 0.019	0.972 ± 0.016	0.984 ± 0.011	0.992 ± 0.017
$31 < p_T < 32.5$	0.969 ± 0.013	0.969 ± 0.009	0.959 ± 0.016	0.961 ± 0.015	0.990 ± 0.010	1.001 ± 0.017
$32.5 < p_T < 35$	0.987 ± 0.009	0.970 ± 0.006	0.957 ± 0.012	0.988 ± 0.009	0.983 ± 0.008	0.987 ± 0.013
$35 < p_T < 40$	0.982 ± 0.006	0.967 ± 0.004	0.961 ± 0.006	0.968 ± 0.006	0.982 ± 0.005	0.998 ± 0.007
$40 < p_T < 45$	0.979 ± 0.005	0.976 ± 0.003	0.972 ± 0.005	0.972 ± 0.005	0.985 ± 0.004	0.985 ± 0.007
$45 < p_T < 50$	0.971 ± 0.007	0.968 ± 0.005	0.957 ± 0.007	0.976 ± 0.006	0.986 ± 0.005	0.981 ± 0.010
$50 < p_T < 60$	0.979 ± 0.009	0.955 ± 0.006	0.969 ± 0.009	0.968 ± 0.008	0.996 ± 0.005	0.968 ± 0.012
$60 < p_T < 80$	0.957 ± 0.015	0.978 ± 0.008	0.940 ± 0.016	0.998 ± 0.010	0.993 ± 0.009	0.969 ± 0.023
$80 < p_T < 1e+04$	0.990 ± 0.024	0.974 ± 0.017	0.924 ± 0.032	0.948 ± 0.027	0.996 ± 0.020	0.960 ± 0.048

Table A.7: Single muon trigger efficiency scale factors in (p_T, η) bins for positively charged muons in the 13 TeV samples.

	$-2.4 < \eta < -2.1$	$-2.1 < \eta < -1.6$	$-1.6 < \eta < -1.2$	$-1.2 < \eta < -0.9$	$-0.9 < \eta < -0.3$	$-0.3 < \eta < 0$
$25 < p_T < 26.5$	0.990 ± 0.024	0.975 ± 0.019	0.968 ± 0.020	0.975 ± 0.022	0.997 ± 0.010	1.002 ± 0.016
$26.5 < p_T < 28$	0.983 ± 0.023	0.962 ± 0.019	0.944 ± 0.020	0.981 ± 0.018	0.969 ± 0.011	0.968 ± 0.017
$28 < p_T < 29.5$	1.016 ± 0.021	0.968 ± 0.017	0.957 ± 0.018	0.966 ± 0.017	0.963 ± 0.010	1.004 ± 0.011
$29.5 < p_T < 31$	0.968 ± 0.022	0.980 ± 0.015	0.966 ± 0.015	0.979 ± 0.016	0.980 ± 0.008	0.989 ± 0.012
$31 < p_T < 32.5$	0.981 ± 0.021	0.994 ± 0.013	0.958 ± 0.014	0.980 ± 0.013	0.976 ± 0.008	0.994 ± 0.011
$32.5 < p_T < 35$	0.947 ± 0.016	0.968 ± 0.011	0.965 ± 0.011	0.972 ± 0.010	0.988 ± 0.005	0.993 ± 0.008
$35 < p_T < 40$	0.969 ± 0.010	0.973 ± 0.006	0.968 ± 0.006	0.975 ± 0.006	0.987 ± 0.003	0.989 ± 0.005
$40 < p_T < 45$	0.971 ± 0.009	0.976 ± 0.006	0.970 ± 0.005	0.976 ± 0.005	0.981 ± 0.003	0.987 ± 0.005
$45 < p_T < 50$	0.962 ± 0.012	0.977 ± 0.007	0.972 ± 0.006	0.978 ± 0.006	0.986 ± 0.004	0.991 ± 0.006
$50 < p_T < 60$	0.957 ± 0.015	0.965 ± 0.009	0.972 ± 0.008	0.980 ± 0.008	0.975 ± 0.006	0.971 ± 0.009
$60 < p_T < 80$	0.941 ± 0.025	0.956 ± 0.015	0.982 ± 0.011	0.969 ± 0.014	1.000 ± 0.007	1.006 ± 0.011
$80 < p_T < 1e+04$	0.940 ± 0.057	0.965 ± 0.028	0.917 ± 0.031	0.957 ± 0.028	0.965 ± 0.016	0.986 ± 0.026
	$0 < \eta < 0.3$	$0.3 < \eta < 0.9$	$0.9 < \eta < 1.2$	$1.2 < \eta < 1.6$	$1.6 < \eta < 2.1$	$2.1 < \eta < 2.4$
$25 < p_T < 26.5$	0.986 ± 0.015	0.994 ± 0.009	0.991 ± 0.020	0.966 ± 0.020	0.997 ± 0.012	1.002 ± 0.017
$26.5 < p_T < 28$	0.986 ± 0.014	0.986 ± 0.010	0.967 ± 0.020	0.951 ± 0.021	0.987 ± 0.013	0.994 ± 0.023
$28 < p_T < 29.5$	0.966 ± 0.015	0.993 ± 0.010	0.993 ± 0.014	0.938 ± 0.020	0.997 ± 0.010	0.996 ± 0.020
$29.5 < p_T < 31$	0.967 ± 0.015	0.986 ± 0.009	0.989 ± 0.014	0.961 ± 0.017	0.995 ± 0.010	0.993 ± 0.017
$31 < p_T < 32.5$	0.992 ± 0.012	0.982 ± 0.008	0.972 ± 0.014	0.927 ± 0.018	0.990 ± 0.010	1.004 ± 0.016
$32.5 < p_T < 35$	0.985 ± 0.008	0.993 ± 0.005	0.969 ± 0.010	0.964 ± 0.010	0.991 ± 0.007	0.992 ± 0.012
$35 < p_T < 40$	0.978 ± 0.006	0.973 ± 0.004	0.969 ± 0.006	0.965 ± 0.006	0.994 ± 0.004	0.995 ± 0.007
$40 < p_T < 45$	0.983 ± 0.005	0.981 ± 0.003	0.965 ± 0.006	0.974 ± 0.005	0.991 ± 0.004	0.985 ± 0.007
$45 < p_T < 50$	0.981 ± 0.007	0.975 ± 0.005	0.957 ± 0.008	0.971 ± 0.006	0.988 ± 0.005	0.977 ± 0.009
$50 < p_T < 60$	0.983 ± 0.009	0.974 ± 0.006	0.971 ± 0.009	0.975 ± 0.008	0.994 ± 0.006	0.990 ± 0.012
$60 < p_T < 80$	1.003 ± 0.013	0.980 ± 0.009	0.942 ± 0.016	0.984 ± 0.011	0.995 ± 0.009	0.954 ± 0.023
$80 < p_T < 1e+04$	0.944 ± 0.031	0.962 ± 0.018	0.981 ± 0.023	0.993 ± 0.021	1.001 ± 0.019	1.024 ± 0.038

Table A.8: Single muon trigger efficiency scale factors in (p_T, η) bins for negatively charged muons in the 13 TeV samples.

	$-2.4 < \eta < -2$	$-2 < \eta < -1.566$	$-1.566 < \eta < -1.4442$	$-1.4442 < \eta < -1$	$-1 < \eta < -0.5$	$-0.5 < \eta < 0$
$25 < p_T < 35$	0.982 ± 0.021	0.911 ± 0.012	1.022 ± 0.093	0.905 ± 0.023	0.936 ± 0.016	0.947 ± 0.011
$35 < p_T < 50$	0.974 ± 0.010	0.948 ± 0.006	0.939 ± 0.020	0.939 ± 0.005	0.947 ± 0.005	0.934 ± 0.005
$50 < p_T < 1e+04$	0.981 ± 0.021	0.971 ± 0.019	0.991 ± 0.043	0.944 ± 0.010	0.958 ± 0.011	0.971 ± 0.013
	$0 < \eta < 0.5$	$0.5 < \eta < 1$	$1 < \eta < 1.44$	$1.44 < \eta < 1.57$	$1.57 < \eta < 2$	$2 < \eta < 2.4$
$25 < p_T < 35$	0.910 ± 0.014	0.925 ± 0.017	0.886 ± 0.019	0.873 ± 0.043	0.867 ± 0.003	0.966 ± 0.023
$35 < p_T < 50$	0.934 ± 0.004	0.938 ± 0.005	0.925 ± 0.008	0.992 ± 0.029	0.945 ± 0.006	0.932 ± 0.010
$50 < p_T < 1e+04$	0.932 ± 0.008	0.964 ± 0.012	0.955 ± 0.010	1.015 ± 0.061	0.953 ± 0.017	0.979 ± 0.022

Table A.9: GSF electron identification and isolation efficiency scale factors in (p_T, η) bins for combined charged electrons in the 5 TeV samples.

	$-2.4 < \eta < -2$	$-2 < \eta < -1.566$	$-1.566 < \eta < -1.4442$	$-1.4442 < \eta < -1$	$-1 < \eta < -0.5$	$-0.5 < \eta < 0$
$25 < p_T < 26.5$	0.530 ± 0.086	0.851 ± 0.064	0.713 ± 0.266	1.038 ± 0.063	0.969 ± 0.050	0.930 ± 0.049
$26.5 < p_T < 28$	0.629 ± 0.077	0.903 ± 0.059	0.721 ± 0.184	1.051 ± 0.053	0.955 ± 0.044	0.959 ± 0.042
$28 < p_T < 29.5$	0.641 ± 0.067	0.915 ± 0.055	1.103 ± 0.127	1.018 ± 0.048	0.926 ± 0.041	0.971 ± 0.033
$29.5 < p_T < 31$	0.603 ± 0.066	0.917 ± 0.047	0.893 ± 0.143	0.980 ± 0.041	0.948 ± 0.032	0.946 ± 0.032
$31 < p_T < 32.5$	0.700 ± 0.063	0.927 ± 0.047	0.886 ± 0.129	0.949 ± 0.045	0.956 ± 0.027	0.969 ± 0.028
$32.5 < p_T < 35$	0.686 ± 0.044	0.913 ± 0.032	0.862 ± 0.102	0.951 ± 0.029	0.927 ± 0.021	0.962 ± 0.019
$35 < p_T < 40$	0.817 ± 0.025	0.934 ± 0.018	0.931 ± 0.051	0.960 ± 0.015	0.935 ± 0.012	0.965 ± 0.011
$40 < p_T < 45$	0.818 ± 0.023	0.933 ± 0.015	0.968 ± 0.037	0.970 ± 0.012	0.955 ± 0.010	0.964 ± 0.009
$45 < p_T < 50$	0.827 ± 0.029	0.942 ± 0.018	0.984 ± 0.049	0.988 ± 0.013	0.964 ± 0.012	0.953 ± 0.012
$50 < p_T < 60$	0.868 ± 0.036	0.895 ± 0.027	0.999 ± 0.066	1.005 ± 0.018	0.941 ± 0.017	0.969 ± 0.015
$60 < p_T < 80$	0.890 ± 0.082	0.955 ± 0.040	0.931 ± 0.143	0.993 ± 0.027	0.972 ± 0.026	0.967 ± 0.028
$80 < p_T < 1e+04$	0.952 ± 0.225	0.987 ± 0.066	0.833 ± 0.449	1.030 ± 0.055	0.983 ± 0.041	0.924 ± 0.070
	$0 < \eta < 0.5$	$0.5 < \eta < 1$	$1 < \eta < 1.44$	$1.44 < \eta < 1.57$	$1.57 < \eta < 2$	$2 < \eta < 2.4$
$25 < p_T < 26.5$	0.885 ± 0.051	0.901 ± 0.054	1.099 ± 0.056	0.890 ± 0.192	0.814 ± 0.074	0.641 ± 0.087
$26.5 < p_T < 28$	0.938 ± 0.047	0.951 ± 0.044	1.008 ± 0.059	0.872 ± 0.165	0.808 ± 0.068	0.666 ± 0.080
$28 < p_T < 29.5$	0.984 ± 0.032	0.962 ± 0.042	0.961 ± 0.057	0.860 ± 0.168	0.846 ± 0.057	0.692 ± 0.090
$29.5 < p_T < 31$	0.964 ± 0.034	0.977 ± 0.033	0.976 ± 0.046	1.220 ± 0.320	0.906 ± 0.052	0.724 ± 0.074
$31 < p_T < 32.5$	0.955 ± 0.028	0.947 ± 0.033	0.952 ± 0.045	0.801 ± 0.118	0.897 ± 0.049	0.743 ± 0.077
$32.5 < p_T < 35$	0.929 ± 0.020	0.934 ± 0.021	0.916 ± 0.034	0.954 ± 0.096	0.853 ± 0.037	0.699 ± 0.048
$35 < p_T < 40$	0.969 ± 0.011	0.955 ± 0.011	0.958 ± 0.016	0.937 ± 0.050	0.916 ± 0.019	0.764 ± 0.029
$40 < p_T < 45$	0.954 ± 0.010	0.951 ± 0.010	0.945 ± 0.014	0.946 ± 0.045	0.937 ± 0.016	0.796 ± 0.026
$45 < p_T < 50$	0.954 ± 0.012	0.954 ± 0.013	0.990 ± 0.015	0.948 ± 0.051	0.893 ± 0.021	0.829 ± 0.031
$50 < p_T < 60$	0.948 ± 0.018	0.956 ± 0.017	0.932 ± 0.023	0.996 ± 0.066	0.984 ± 0.023	0.947 ± 0.037
$60 < p_T < 80$	0.943 ± 0.029	0.942 ± 0.032	1.013 ± 0.027	1.016 ± 0.143	1.021 ± 0.037	1.020 ± 0.062
$80 < p_T < 1e+04$	0.888 ± 0.063	0.960 ± 0.057	1.055 ± 0.061	0.576 ± 0.365	0.979 ± 0.078	0.882 ± 0.240

Table A.10: Single electron trigger efficiency scale factors in (p_T, η) bins for positively charged electrons in the 5 TeV samples.

	$-2.4 < \eta < -2$	$-2 < \eta < -1.566$	$-1.566 < \eta < -1.4442$	$-1.4442 < \eta < -1$	$-1 < \eta < -0.5$	$-0.5 < \eta < 0$
$25 < p_T < 26.5$	0.771 ± 0.079	0.887 ± 0.065	1.130 ± 0.178	1.056 ± 0.062	0.948 ± 0.047	0.988 ± 0.049
$26.5 < p_T < 28$	0.767 ± 0.069	0.804 ± 0.068	0.838 ± 0.172	0.914 ± 0.065	0.927 ± 0.047	1.005 ± 0.039
$28 < p_T < 29.5$	0.542 ± 0.069	0.889 ± 0.057	1.221 ± 0.111	0.975 ± 0.048	0.914 ± 0.037	0.958 ± 0.036
$29.5 < p_T < 31$	0.719 ± 0.058	0.831 ± 0.057	0.918 ± 0.168	0.981 ± 0.049	0.952 ± 0.034	0.921 ± 0.034
$31 < p_T < 32.5$	0.810 ± 0.054	0.934 ± 0.047	1.007 ± 0.112	0.987 ± 0.037	0.967 ± 0.028	0.913 ± 0.032
$32.5 < p_T < 35$	0.734 ± 0.042	0.925 ± 0.032	0.973 ± 0.080	0.981 ± 0.026	0.935 ± 0.020	0.950 ± 0.020
$35 < p_T < 40$	0.729 ± 0.026	0.909 ± 0.019	0.872 ± 0.052	0.949 ± 0.015	0.936 ± 0.011	0.952 ± 0.011
$40 < p_T < 45$	0.825 ± 0.023	0.946 ± 0.014	0.964 ± 0.043	0.985 ± 0.011	0.970 ± 0.009	0.957 ± 0.010
$45 < p_T < 50$	0.820 ± 0.028	0.961 ± 0.017	0.973 ± 0.050	0.975 ± 0.014	0.968 ± 0.011	0.943 ± 0.013
$50 < p_T < 60$	0.866 ± 0.036	0.925 ± 0.023	0.938 ± 0.069	0.938 ± 0.021	0.940 ± 0.018	0.948 ± 0.017
$60 < p_T < 80$	0.973 ± 0.056	0.982 ± 0.039	1.081 ± 0.091	1.050 ± 0.024	0.957 ± 0.030	0.960 ± 0.028
$80 < p_T < 1e+04$	0.950 ± 0.159	0.982 ± 0.111	0.628 ± 0.327	0.996 ± 0.068	0.964 ± 0.062	0.833 ± 0.070
	$0 < \eta < 0.5$	$0.5 < \eta < 1$	$1 < \eta < 1.44$	$1.44 < \eta < 1.57$	$1.57 < \eta < 2$	$2 < \eta < 2.4$
$25 < p_T < 26.5$	0.898 ± 0.053	0.877 ± 0.061	0.895 ± 0.076	0.985 ± 0.170	0.818 ± 0.069	0.697 ± 0.089
$26.5 < p_T < 28$	0.951 ± 0.042	0.956 ± 0.045	1.008 ± 0.059	1.142 ± 0.109	0.937 ± 0.057	0.636 ± 0.078
$28 < p_T < 29.5$	0.947 ± 0.037	0.991 ± 0.038	0.901 ± 0.054	0.840 ± 0.176	0.875 ± 0.065	0.656 ± 0.071
$29.5 < p_T < 31$	0.963 ± 0.032	0.895 ± 0.036	0.981 ± 0.048	0.884 ± 0.123	0.881 ± 0.054	0.567 ± 0.068
$31 < p_T < 32.5$	0.940 ± 0.030	0.970 ± 0.032	0.982 ± 0.047	1.033 ± 0.129	0.918 ± 0.045	0.675 ± 0.061
$32.5 < p_T < 35$	0.935 ± 0.021	0.940 ± 0.021	1.004 ± 0.026	0.809 ± 0.109	0.906 ± 0.035	0.700 ± 0.043
$35 < p_T < 40$	0.955 ± 0.012	0.942 ± 0.012	0.949 ± 0.016	0.920 ± 0.050	0.889 ± 0.020	0.798 ± 0.029
$40 < p_T < 45$	0.943 ± 0.010	0.963 ± 0.010	0.955 ± 0.014	0.991 ± 0.041	0.923 ± 0.016	0.776 ± 0.026
$45 < p_T < 50$	0.956 ± 0.012	0.955 ± 0.013	0.947 ± 0.017	1.003 ± 0.048	0.914 ± 0.020	0.829 ± 0.032
$50 < p_T < 60$	0.976 ± 0.016	0.946 ± 0.017	0.969 ± 0.022	0.977 ± 0.065	0.922 ± 0.026	0.810 ± 0.043
$60 < p_T < 80$	0.963 ± 0.028	0.988 ± 0.025	0.979 ± 0.035	1.017 ± 0.105	0.936 ± 0.050	0.989 ± 0.056
$80 < p_T < 1e+04$	0.996 ± 0.039	1.068 ± 0.033	0.878 ± 0.103	0.785 ± 0.315	0.959 ± 0.092	0.819 ± 0.197

Table A.11: Single electron trigger efficiency scale factors in (p_T, η) bins for negatively charged electrons in the 5 TeV samples.

	$-2.4 < \eta < -2.1$	$-2.1 < \eta < -1.6$	$-1.6 < \eta < -1.2$	$-1.2 < \eta < -0.9$	$-0.9 < \eta < -0.3$	$-0.3 < \eta < 0$
$25 < p_T < 35$	0.991 ± 0.007	1.003 ± 0.005	1.005 ± 0.006	0.992 ± 0.007	0.997 ± 0.004	0.990 ± 0.006
$35 < p_T < 50$	0.991 ± 0.003	0.996 ± 0.002	0.999 ± 0.002	0.993 ± 0.003	0.996 ± 0.002	0.990 ± 0.003
$50 < p_T < 1e+04$	0.978 ± 0.008	1.001 ± 0.004	0.989 ± 0.005	0.991 ± 0.006	0.991 ± 0.004	0.997 ± 0.005
	$0 < \eta < 0.3$	$0.3 < \eta < 0.9$	$0.9 < \eta < 1.2$	$1.2 < \eta < 1.6$	$1.6 < \eta < 2.1$	$2.1 < \eta < 2.4$
$25 < p_T < 35$	0.985 ± 0.006	0.999 ± 0.005	1.002 ± 0.007	0.995 ± 0.006	0.996 ± 0.005	0.995 ± 0.007
$35 < p_T < 50$	0.992 ± 0.003	0.992 ± 0.002	0.986 ± 0.002	0.997 ± 0.002	0.996 ± 0.002	0.991 ± 0.003
$50 < p_T < 1e+04$	0.992 ± 0.007	0.995 ± 0.004	0.990 ± 0.006	0.994 ± 0.004	1.002 ± 0.004	0.996 ± 0.008

Table A.12: Muon selection efficiency scale factors in (p_T, η) bins for combined charged muons in the 5 TeV samples.

	$-2.4 < \eta < -2.1$	$-2.1 < \eta < -1.6$	$-1.6 < \eta < -1.2$	$-1.2 < \eta < -0.9$	$-0.9 < \eta < -0.3$	$-0.3 < \eta < 0$
$25 < p_T < 35$	0.990 ± 0.008	0.978 ± 0.015	0.992 ± 0.000	0.970 ± 0.001	1.003 ± 0.006	0.992 ± 0.006
$35 < p_T < 50$	0.987 ± 0.002	0.992 ± 0.000	1.000 ± 0.001	0.996 ± 0.001	0.997 ± 0.001	0.993 ± 0.001
$50 < p_T < 1e+04$	0.990 ± 0.001	0.984 ± 0.007	0.986 ± 0.009	1.000 ± 0.003	0.996 ± 0.003	0.990 ± 0.006
	$0 < \eta < 0.3$	$0.3 < \eta < 0.9$	$0.9 < \eta < 1.2$	$1.2 < \eta < 1.6$	$1.6 < \eta < 2.1$	$2.1 < \eta < 2.4$
$25 < p_T < 35$	0.980 ± 0.007	0.985 ± 0.007	0.994 ± 0.011	0.992 ± 0.000	0.963 ± 0.020	0.951 ± 0.019
$35 < p_T < 50$	0.992 ± 0.004	0.996 ± 0.000	0.990 ± 0.002	0.993 ± 0.000	0.995 ± 0.000	0.995 ± 0.001
$50 < p_T < 1e+04$	0.972 ± 0.007	0.997 ± 0.002	0.992 ± 0.005	0.981 ± 0.008	0.987 ± 0.009	0.995 ± 0.006

Table A.13: Standalone muon identification efficiency scale factors in (p_T, η) bins for combined charged muons in the 5 TeV samples.

	$-2.4 < \eta < -2.1$	$-2.1 < \eta < -1.6$	$-1.6 < \eta < -1.2$	$-1.2 < \eta < -0.9$	$-0.9 < \eta < -0.3$	$-0.3 < \eta < 0$
$25 < p_T < 26.5$	0.974 ± 0.041	1.013 ± 0.020	1.023 ± 0.015	0.984 ± 0.023	1.014 ± 0.011	1.006 ± 0.019
$26.5 < p_T < 28$	0.999 ± 0.027	0.992 ± 0.022	0.965 ± 0.022	0.946 ± 0.031	1.002 ± 0.011	0.988 ± 0.019
$28 < p_T < 29.5$	0.971 ± 0.030	0.962 ± 0.024	0.995 ± 0.016	0.979 ± 0.022	0.981 ± 0.013	0.961 ± 0.020
$29.5 < p_T < 31$	0.972 ± 0.031	0.992 ± 0.017	0.969 ± 0.018	0.986 ± 0.018	0.973 ± 0.013	0.998 ± 0.015
$31 < p_T < 32.5$	0.970 ± 0.028	0.969 ± 0.020	0.986 ± 0.017	0.973 ± 0.019	0.979 ± 0.011	0.992 ± 0.015
$32.5 < p_T < 35$	0.982 ± 0.019	0.995 ± 0.011	0.973 ± 0.013	0.990 ± 0.011	0.987 ± 0.007	0.976 ± 0.011
$35 < p_T < 40$	1.001 ± 0.010	0.983 ± 0.008	0.976 ± 0.007	0.974 ± 0.007	0.995 ± 0.004	0.987 ± 0.007
$40 < p_T < 45$	0.996 ± 0.010	0.983 ± 0.006	0.983 ± 0.005	0.972 ± 0.006	0.990 ± 0.004	0.998 ± 0.006
$45 < p_T < 50$	0.997 ± 0.014	0.990 ± 0.008	0.984 ± 0.006	0.986 ± 0.007	0.995 ± 0.005	0.998 ± 0.008
$50 < p_T < 60$	0.999 ± 0.019	0.989 ± 0.011	0.988 ± 0.009	0.972 ± 0.012	1.007 ± 0.007	0.983 ± 0.012
$60 < p_T < 80$	0.971 ± 0.043	0.999 ± 0.018	0.955 ± 0.021	0.978 ± 0.019	0.995 ± 0.013	0.991 ± 0.023
$80 < p_T < 1e+04$	0.979 ± 0.182	1.005 ± 0.047	0.969 ± 0.040	0.985 ± 0.051	1.000 ± 0.028	0.984 ± 0.055
	$0 < \eta < 0.3$	$0.3 < \eta < 0.9$	$0.9 < \eta < 1.2$	$1.2 < \eta < 1.6$	$1.6 < \eta < 2.1$	$2.1 < \eta < 2.4$
$25 < p_T < 26.5$	0.999 ± 0.019	0.959 ± 0.017	0.972 ± 0.024	0.983 ± 0.022	0.989 ± 0.020	0.954 ± 0.035
$26.5 < p_T < 28$	0.977 ± 0.020	0.964 ± 0.015	0.937 ± 0.032	0.938 ± 0.026	1.003 ± 0.016	0.995 ± 0.027
$28 < p_T < 29.5$	0.977 ± 0.021	0.975 ± 0.013	0.967 ± 0.022	0.973 ± 0.021	0.974 ± 0.017	0.993 ± 0.028
$29.5 < p_T < 31$	1.000 ± 0.014	0.979 ± 0.011	0.920 ± 0.027	0.996 ± 0.016	0.981 ± 0.016	1.030 ± 0.018
$31 < p_T < 32.5$	0.964 ± 0.016	0.970 ± 0.012	0.994 ± 0.015	0.978 ± 0.017	0.988 ± 0.013	0.948 ± 0.029
$32.5 < p_T < 35$	0.978 ± 0.011	0.991 ± 0.006	0.957 ± 0.014	0.962 ± 0.014	0.979 ± 0.010	0.997 ± 0.015
$35 < p_T < 40$	0.981 ± 0.007	0.980 ± 0.004	0.965 ± 0.007	0.964 ± 0.008	0.985 ± 0.006	0.983 ± 0.010
$40 < p_T < 45$	0.987 ± 0.006	0.977 ± 0.004	0.965 ± 0.006	0.986 ± 0.005	0.989 ± 0.005	0.992 ± 0.009
$45 < p_T < 50$	0.981 ± 0.009	0.968 ± 0.006	0.959 ± 0.009	0.972 ± 0.008	0.972 ± 0.007	0.997 ± 0.011
$50 < p_T < 60$	0.970 ± 0.013	0.982 ± 0.007	0.967 ± 0.012	0.980 ± 0.010	0.988 ± 0.008	0.973 ± 0.022
$60 < p_T < 80$	0.988 ± 0.022	0.964 ± 0.016	0.942 ± 0.027	0.975 ± 0.020	0.990 ± 0.018	0.970 ± 0.036
$80 < p_T < 1e+04$	0.978 ± 0.053	0.993 ± 0.025	0.878 ± 0.069	0.869 ± 0.071	1.032 ± 0.032	1.000 ± 0.094

Table A.14: Single muon trigger efficiency scale factors in (p_T, η) bins for positively charged muons in the 5 TeV samples.

	$-2.4 < \eta < -2.1$	$-2.1 < \eta < -1.6$	$-1.6 < \eta < -1.2$	$-1.2 < \eta < -0.9$	$-0.9 < \eta < -0.3$	$-0.3 < \eta < 0$
$25 < p_T < 26.5$	0.951 ± 0.044	0.981 ± 0.024	0.991 ± 0.021	0.974 ± 0.024	0.985 ± 0.016	1.003 ± 0.016
$26.5 < p_T < 28$	0.972 ± 0.039	0.983 ± 0.019	1.002 ± 0.016	1.011 ± 0.017	0.975 ± 0.014	0.996 ± 0.016
$28 < p_T < 29.5$	0.989 ± 0.033	0.998 ± 0.018	0.982 ± 0.018	0.954 ± 0.023	0.985 ± 0.011	0.974 ± 0.019
$29.5 < p_T < 31$	0.985 ± 0.033	0.981 ± 0.019	0.984 ± 0.018	0.963 ± 0.021	0.977 ± 0.011	0.991 ± 0.015
$31 < p_T < 32.5$	0.997 ± 0.025	0.999 ± 0.016	0.992 ± 0.015	0.973 ± 0.019	0.986 ± 0.010	1.012 ± 0.011
$32.5 < p_T < 35$	1.009 ± 0.016	0.985 ± 0.013	0.988 ± 0.011	0.982 ± 0.014	0.979 ± 0.007	0.987 ± 0.011
$35 < p_T < 40$	0.990 ± 0.011	0.982 ± 0.007	0.983 ± 0.006	0.966 ± 0.008	0.979 ± 0.004	0.970 ± 0.007
$40 < p_T < 45$	0.995 ± 0.010	0.991 ± 0.006	0.986 ± 0.005	0.972 ± 0.006	0.978 ± 0.004	0.993 ± 0.006
$45 < p_T < 50$	0.976 ± 0.014	0.992 ± 0.007	0.974 ± 0.007	0.984 ± 0.008	0.988 ± 0.005	0.981 ± 0.008
$50 < p_T < 60$	0.986 ± 0.018	0.989 ± 0.010	0.991 ± 0.009	0.970 ± 0.012	0.994 ± 0.007	0.992 ± 0.010
$60 < p_T < 80$	1.029 ± 0.027	0.968 ± 0.021	0.969 ± 0.019	0.978 ± 0.020	0.982 ± 0.012	1.000 ± 0.020
$80 < p_T < 1e+04$	0.920 ± 0.140	1.008 ± 0.038	0.998 ± 0.045	0.969 ± 0.054	0.992 ± 0.033	1.003 ± 0.041
	$0 < \eta < 0.3$	$0.3 < \eta < 0.9$	$0.9 < \eta < 1.2$	$1.2 < \eta < 1.6$	$1.6 < \eta < 2.1$	$2.1 < \eta < 2.4$
$25 < p_T < 26.5$	0.994 ± 0.021	0.982 ± 0.017	0.961 ± 0.029	0.976 ± 0.026	1.003 ± 0.014	1.038 ± 0.020
$26.5 < p_T < 28$	0.992 ± 0.019	0.975 ± 0.015	0.983 ± 0.023	0.953 ± 0.024	0.984 ± 0.017	0.990 ± 0.030
$28 < p_T < 29.5$	1.007 ± 0.015	0.986 ± 0.013	0.969 ± 0.024	0.988 ± 0.019	0.993 ± 0.014	0.989 ± 0.029
$29.5 < p_T < 31$	1.002 ± 0.014	0.994 ± 0.010	0.955 ± 0.023	1.003 ± 0.016	0.991 ± 0.015	0.974 ± 0.028
$31 < p_T < 32.5$	0.999 ± 0.014	0.983 ± 0.010	0.974 ± 0.017	0.970 ± 0.018	0.969 ± 0.016	1.025 ± 0.017
$32.5 < p_T < 35$	1.001 ± 0.010	0.978 ± 0.008	0.966 ± 0.013	0.979 ± 0.012	1.000 ± 0.008	0.968 ± 0.019
$35 < p_T < 40$	0.984 ± 0.007	0.987 ± 0.004	0.969 ± 0.007	0.971 ± 0.007	0.988 ± 0.006	0.997 ± 0.009
$40 < p_T < 45$	0.985 ± 0.006	0.977 ± 0.004	0.965 ± 0.007	0.971 ± 0.006	0.992 ± 0.005	0.986 ± 0.009
$45 < p_T < 50$	0.988 ± 0.008	0.987 ± 0.005	0.965 ± 0.009	0.969 ± 0.008	1.000 ± 0.005	0.987 ± 0.012
$50 < p_T < 60$	1.000 ± 0.010	0.988 ± 0.008	0.963 ± 0.012	0.992 ± 0.010	0.998 ± 0.008	1.013 ± 0.015
$60 < p_T < 80$	0.968 ± 0.024	0.978 ± 0.014	0.959 ± 0.026	0.984 ± 0.017	0.988 ± 0.016	0.983 ± 0.035
$80 < p_T < 1e+04$	0.975 ± 0.046	0.979 ± 0.036	0.929 ± 0.081	0.952 ± 0.053	0.939 ± 0.050	1.012 ± 0.079

Table A.15: Single muon trigger efficiency scale factors in (p_T, η) bins for negatively charged muons in the 5 TeV samples.

Bibliography

[1] G. Arnison et al. Experimental Observation of Lepton Pairs of Invariant Mass Around 95-GeV/c**2 at the CERN SPS Collider. *Phys. Lett.*, B126:398–410, 1983. [,7.55(1983)].

[2] P. Bagnaia et al. Evidence for Z0 —> e+ e- at the CERN anti-p p Collider. *Phys. Lett.*, B129:130–140, 1983. [,7.69(1983)].

[3] M. Banner et. al. Observation of single isolated electrons of high transverse momentum in events with missing transverse energy at the cern pp collider. *Physics Letters B*, 122(5):476 – 485, 1983.

[4] G. Arnison et. al. Experimental observation of isolated large transverse energy electrons with associated missing energy at s=540 gev. *Physics Letters B*, 122(1):103 – 116, 1983.

[5] M. Tanabashi et al. Review of particle physics. *Phys. Rev. D*, 98:030001, Aug 2018.

[6] S. Schael et al. Precision electroweak measurements on the Z resonance. *Phys. Rept.*, 427:257–454, 2006.

[7] Georges Aad et al. Measurement of $W^{\pm}$-boson and Z-boson production cross-sections in pp collisions at $\sqrt{s} = 2.76\,\text{TeV}$ with the ATLAS detector. *Eur. Phys. J. C*, 79(11):901, 2019.

[8] Morad Aaboud et al. Measurements of W and Z boson production in pp collisions at $\sqrt{s} = 5.02\,\text{TeV}$ with the ATLAS detector. *Eur. Phys. J. C*, 79(2):128, 2019. [Erratum: Eur. Phys. J.C79,no.5,374(2019)].

[9] Morad Aaboud et al. Precision measurement and interpretation of inclusive W^+ , W^- and Z/γ^* production cross sections with the ATLAS detector. *Eur. Phys. J. C*, 77(6):367, 2017.

[10] Serguei Chatrchyan et al. Measurement of the inclusive W and Z production cross sections in pp Collisions at $\sqrt{s} = 7\,\text{TeV}$. *JHEP*, 10:132, 2011.

[11] Roel Aaij et al. Measurement of the forward W boson cross-section in pp collisions at $\sqrt{s} = 7\,\text{TeV}$. *JHEP*, 12:079, 2014.

[12] R Aaij et al. Measurement of the cross-section for $Z \to e^+e^-$ production in pp collisions at $\sqrt{s} = 7\,\text{TeV}$. *JHEP*, 02:106, 2013.

[13] Roel Aaij et al. Measurement of the forward Z boson production cross-section in pp collisions at $\sqrt{s} = 7\,\text{TeV}$. *JHEP*, 08:039, 2015.

[14] Roel Aaij et al. Measurement of forward $W \to e\nu$ production in pp collisions at $\sqrt{s} = 8\,\text{TeV}$. *JHEP*, 10:030, 2016.

[15] Roel Aaij et al. Measurement of the forward Z boson production cross-section in pp collisions at $\sqrt{s} = 13\,\text{TeV}$. *JHEP*, 09:136, 2016.

[16] Roel Aaij et al. Measurement of forward W and Z boson production in pp collisions at $\sqrt{s} = 8\,\text{TeV}$. *JHEP*, 01:155, 2016.

[17] Serguei Chatrchyan et al. Measurement of inclusive W and Z boson production cross sections in pp collisions at $\sqrt{s} = 8$ TeV. *Phys. Rev. Lett.*, 112:191802, 2014.

[18] Georges Aad et al. Measurement of $W^{\pm}$ and Z-boson production cross sections in pp collisions at $\sqrt{s} = 13\,\text{TeV}$ with the ATLAS detector. *Phys. Lett. B*, 759:601, 2016.

[19] A. Ocampo, Abdulla Abdulsalam, A. Adair, A. Adiguzel, A. Anastassov, A. Apresyan, A. Apyan, A. Askew, A. Attikis, A. Avetisyan, A. Meyer, A. Baden, Anthony Barker, A. Bean, Alexander Belyaev, Andrea Benaglia, A. De, A. Beretvas, A. Bethani, and Zonghao Zhang. Measurement of inclusive w and z boson production cross sections in p p collisions at s = 8 tev. *Physical review letters*, 112, 02 2014.

[20] Xinmei Niu. *Z boson cross section measurements and neutral Higgs boson search in the di-muon channel with the CMS detector*. PhD thesis, Massachusetts Institute of Technology, 2019.

[21] Cush. Standard Model of Elementary Particles, Sept 2019. Custom image created for Wikipedia.

[22] S. L. Glashow. Partial Symmetries of Weak Interactions. *Nucl. Phys.*, 22:579–588, 1961.

[23] Steven Weinberg. A model of leptons. *Phys. Rev. Lett.*, 19:1264–1266, Nov 1967.

[24] S. L. Glashow, J. Iliopoulos, and L. Maiani. Weak interactions with lepton-hadron symmetry. *Phys. Rev. D*, 2:1285–1292, Oct 1970.

[25] Nicola Cabibbo. Unitary symmetry and leptonic decays. *Phys. Rev. Lett.*, 10:531–533, Jun 1963.

[26] Makoto Kobayashi and Toshihide Maskawa. CP-Violation in the Renormalizable Theory of Weak Interaction. *Progress of Theoretical Physics*, 49(2):652–657, 02 1973.

[27] F. Englert and R. Brout. Broken symmetry and the mass of gauge vector mesons. *Phys. Rev. Lett.*, 13:321–323, Aug 1964.

[28] Peter W. Higgs. Broken symmetries and the masses of gauge bosons. *Phys. Rev. Lett.*, 13:508–509, Oct 1964.

[29] G. S. Guralnik, C. R. Hagen, and T. W. B. Kibble. Global conservation laws and massless particles. *Phys. Rev. Lett.*, 13:585–587, Nov 1964.

[30] C. A. Baker, D. D. Doyle, P. Geltenbort, K. Green, M. G. D. van der Grinten, P. G. Harris, P. Iaydjiev, S. N. Ivanov, D. J. R. May, J. M. Pendlebury, J. D. Richardson, D. Shiers, and K. F. Smith. Improved experimental limit on the electric dipole moment of the neutron. *Phys. Rev. Lett.*, 97:131801, Sep 2006.

[31] R. Keith Ellis, W. James Stirling, and B. R. Webber. QCD and collider physics. *Camb. Monogr. Part. Phys. Nucl. Phys. Cosmol.*, 8:1–435, 1996.

[32] H. David Politzer. Reliable perturbative results for strong interactions? *Phys. Rev. Lett.*, 30:1346–1349, Jun 1973.

[33] David J. Gross and Frank Wilczek. Ultraviolet behavior of non-abelian gauge theories. *Phys. Rev. Lett.*, 30:1343–1346, Jun 1973.

[34] E. D. Bloom, D. H. Coward, H. DeStaebler, J. Drees, G. Miller, L. W. Mo, R. E. Taylor, M. Breidenbach, J. I. Friedman, G. C. Hartmann, and H. W. Kendall. High-energy inelastic $e - p$ scattering at 6° and 10°. *Phys. Rev. Lett.*, 23:930–934, Oct 1969.

[35] M. Breidenbach, J. I. Friedman, H. W. Kendall, E. D. Bloom, D. H. Coward, H. DeStaebler, J. Drees, L. W. Mo, and R. E. Taylor. Observed behavior of highly inelastic electron-proton scattering. *Phys. Rev. Lett.*, 23:935–939, Oct 1969.

[36] E Perez and E Rizvi. The quark and gluon structure of the proton. *Reports on Progress in Physics*, 76(4):046201, Mar 2013.

[37] Charalampos Anastasiou, Lance J. Dixon, Kirill Melnikov, and Frank Petriello. High precision QCD at hadron colliders: Electroweak gauge boson rapidity distributions at NNLO. *Phys. Rev. D*, 69:094008, 2004.

[38] John C. Collins, Davison E. Soper, and George F. Sterman. Factorization of Hard Processes in QCD. *Adv. Ser. Direct. High Energy Phys.*, 5:1–91, 1989.

[39] V. N. Gribov and L. N. Lipatov. Deep inelastic e p scattering in perturbation theory. *Sov. J. Nucl. Phys.*, 15:438–450, 1972. [Yad. Fiz.15,781(1972)].

[40] Yuri L. Dokshitzer. Calculation of the Structure Functions for Deep Inelastic Scattering and e+ e- Annihilation by Perturbation Theory in Quantum Chromodynamics. *Sov. Phys. JETP*, 46:641–653, 1977. [Zh. Eksp. Teor. Fiz.73,1216(1977)].

[41] Matt Dobbs and Jorgen Beck Hansen. The HepMC C++ Monte Carlo event record for High Energy Physics. *Comput. Phys. Commun.*, 134:41–46, 2001.

[42] Sidney D. Drell and Tung-Mow Yan. Massive lepton-pair production in hadron-hadron collisions at high energies. *Phys. Rev. Lett.*, 25:316–320, Aug 1970.

[43] Richard D. Ball et al. Parton distributions from high-precision collider data. *Eur. Phys. J. C*, 77(10):663, 2017.

[44] Jun Gao, Lucian Harland-Lang, and Juan Rojo. The Structure of the Proton in the LHC Precision Era. *Phys. Rept.*, 742:1–121, 2018.

[45] A. Accardi et al. A Critical Appraisal and Evaluation of Modern PDFs. *Eur. Phys. J. C*, 76(8):471, 2016.

[46] Jon Butterworth et al. PDF4LHC recommendations for LHC Run II. *J. Phys. G*, 43:023001, 2016.

[47] Juan Rojo et al. The PDF4LHC report on PDFs and LHC data: Results from Run I and preparation for Run II. *J. Phys. G*, 42:103103, 2015.

[48] Vincenzo Lombardo. W and Z cross sections at LHC, April 2013. slide from talk.

[49] Julie Haffner. The CERN accelerator complex. Complexe des accélérateurs du CERN, Oct 2013. General Photo.

[50] M. Benedikt, P. Collier, V. Mertens, J. Poole, and K. Schindl. *LHC Design Report. 3. The LHC injector chain*, 2004.

[51] Oliver S. Bruning, P. Collier, P. Lebrun, S. Myers, R. Ostojic, J. Poole, and P. Proudlock. *LHC Design Report Vol.1: The LHC Main Ring*, 2004.

[52] AC Team. Diagram of an LHC dipole magnet. Schéma d'un aimant dipôle du LHC, Jun 1999.

[53] G. L. Bayatian et al. CMS technical design report, volume II: Physics performance. *J. Phys.*, G34(6):995–1579, 2007.

[54] G. L. Bayatian et al. CMS Physics: Technical Design Report Volume 1: Detector Performance and Software. 2006. There is an error on cover due to a technical problem for some items.

[55] G. Acquistapace et al. CMS, the magnet project: Technical design report. 1997.

[56] S Chatrchyan et al. Precise Mapping of the Magnetic Field in the CMS Barrel Yoke using Cosmic Rays. *JINST*, 5:T03021, 2010.

[57] V Karimäki, M Mannelli, P Siegrist, H Breuker, A Caner, R Castaldi, K Freudenreich, G Hall, R Horisberger, M Huhtinen, and A Cattai. *The CMS tracker system project: Technical Design Report*. Technical Design Report CMS. CERN, Geneva, 1997.

[58] The CMS Collaboration. Cms tracking performance results from early lhc operation. *European Physical Journal C*, 70:1165–1192, 04 2010.

[59] CMS Collaboration. *The CMS electromagnetic calorimeter project: Technical Design Report*. Technical Design Report CMS. CERN, Geneva, 1997.

[60] A Benaglia. The CMS ECAL performance with examples. *Journal of Instrumentation*, 9(02):C02008–C02008, feb 2014.

[61] Marco Cipriani. Performance of the CMS electromagnetic calorimeter during the LHC Run II and its role in precision physics measurements. *PoS*, LHCP2018:084, 2018.

[62] P. Adzic et al. Energy resolution of the barrel of the CMS electromagnetic calorimeter. *JINST*, 2:P04004, 2007.

[63] CMS Collaboration. *The CMS hadron calorimeter project: Technical Design Report*. Technical Design Report CMS. CERN, Geneva, 1997.

[64] S et.al. Chatrchyan. Performance of CMS Hadron Calorimeter Timing and Synchronization using Cosmic Ray and LHC Beam Data. *JINST*, 5(arXiv:0911.4877. CMS-CFT-09-018):T03013. 31 p, Nov 2009.

[65] Francesca Cavallari. Performance of calorimeters at the LHC. *Journal of Physics: Conference Series*, 293:012001, apr 2011.

[66] CERN. Geneva. LHC Experiments Committee. *The CMS muon project*, 1997.

[67] Serguei Chatrchyan et al. The Performance of the CMS Muon Detector in Proton-Proton Collisions at $\sqrt{s} = 7$ TeV at the LHC. *JINST*, 8:P11002, 2013.

[68] Vardan Khachatryan et al. The CMS trigger system. *JINST*, 12(01):P01020, 2017.

[69] L. Cadamuro. The CMS Level-1 trigger system for LHC Run II. *JINST*, 12(03):C03021, 2017.

[70] W. Adam et al. The CMS high level trigger. *Eur. Phys. J.*, C46:605–667, 2006.

[71] S. Agostinelli et. al. Geant4—a simulation toolkit. *Nuclear Instruments and Methods in Physics Research Section A: Accelerators, Spectrometers, Detectors and Associated Equipment*, 506(3):250 – 303, 2003.

[72] J. Allison et. al. Recent developments in geant4. *Nuclear Instruments and Methods in Physics Research Section A: Accelerators, Spectrometers, Detectors and Associated Equipment*, 835:186 – 225, 2016.

[73] Paul Joseph Lujan. Van der Meer calibration of the CMS luminosity detectors in 2017. Technical Report CMS-CR-2018-339, CERN, Geneva, Nov 2018.

[74] S. van der Meer. *Calibration of the Effective Beam Height in the ISR*, 1968.

[75] Vladislav Balagura. Notes on van der Meer Scan for Absolute Luminosity Measurement. *Nucl. Instrum. Meth.*, A654:634–638, 2011.

[76] CMS Collaboration. CMS luminosity measurement for the 2017 data-taking period at $\sqrt{s} = 13$ TeV, 2018.

[77] Serguei Chatrchyan et al. Description and performance of track and primary-vertex reconstruction with the CMS tracker. *JINST*, 9(10):P10009, 2014.

[78] W. Adam, B. Mangano, T. Speer, and T. Todorov. Track reconstruction in the CMS tracker. ., 2005.

[79] E. Chabanat and N. Estre. Deterministic annealing for vertex finding at CMS. In *Computing in high energy physics and nuclear physics. Proceedings, Conference, CHEP'04, Interlaken, Switzerland, September 27-October 1, 2004*, pages 287–290, 2005.

[80] A. M. Sirunyan et al. Performance of the CMS muon detector and muon reconstruction with proton-proton collisions at $\sqrt{s} = 13$ TeV. *JINST*, 13(06):P06015, 2018.

[81] CMS Luminosity POG. CMS Luminosity—Public Results. https://twiki.cern.ch/twiki/bin/view/CMSPublic/LumiPublicResults.

[82] J. Alwall, R. Frederix, S. Frixione, V. Hirschi, F. Maltoni, O. Mattelaer, H. S. Shao, T. Stelzer, P. Torrielli, and M. Zaro. The automated computation of tree-level and next-to-leading order differential cross sections, and their matching to parton shower simulations. *JHEP*, 07:079, 2014.

[83] Simone Alioli, Paolo Nason, Carlo Oleari, and Emanuele Re. NLO vector-boson production matched with shower in POWHEG. *JHEP*, 07:060, 2008.

[84] Stefano Frixione, Paolo Nason, and Carlo Oleari. Matching NLO QCD computations with parton shower simulations: the POWHEG method. *JHEP*, 11:070, 2007.

[85] S. Alioli, P. Nason, C. Oleari, and E. Re. A General Framework for Implementing NLO Calculations in Shower Monte Carlo Programs: the POWHEG BOX. *JHEP*, 06:043, 2010.

[86] Simone Alioli, Paolo Nason, Carlo Oleari, and Emanuele Re. A general framework for implementing NLO calculations in shower Monte Carlo programs: the POWHEG BOX. *JHEP*, 06:043, 2010.

[87] Keith Hamilton, Paolo Nason, Carlo Oleari, and Giulia Zanderighi. Merging H/W/Z + 0 and 1 jet at NLO with no merging scale: a path to parton shower + NNLO matching. *JHEP*, 05:082, 2013.

[88] Torbjörn Sjöstrand, Stefan Ask, Jesper R. Christiansen, Richard Corke, Nishita Desai, Philip Ilten, Stephen Mrenna, Stefan Prestel, Christine O. Rasmussen, and Peter Z. Skands. An Introduction to PYTHIA 8.2. *Comput. Phys. Commun.*, 191:159–177, 2015.

[89] Albert M Sirunyan et al. Extraction and validation of a new set of CMS PYTHIA 8 tunes from underlying-event measurements. *Eur. Phys. J. C*, 80(1):4, 2020.

[90] S. Agostinelli et al. GEANT4—a simulation toolkit. *Nucl. Instrum. Meth. A*, 506:250, 2003.

[91] John C. Collins, Davison E. Soper, and George F. Sterman. Transverse momentum distribution in Drell-Yan pair and W and Z boson production. *Nucl. Phys. B*, 250, 1985.

[92] T. Gleisberg, Stefan. Hoeche, F. Krauss, M. Schonherr, S. Schumann, F. Siegert, and J. Winter. Event generation with SHERPA 1.1. *JHEP*, 02:007, 2009.

[93] Manuel Bähr, Stefan Gieseke, Martyn A. Gigg, David Grellscheid, Keith Hamilton, Oluseyi Latunde-Dada, Simon Plätzer, Peter Richardson, Michael H. Seymour, Alexander Sherstnev, and Bryan R. Webber. Herwig++ physics and manual. *Eur. Phys. J. C*, 58:639, 2008.

[94] Paolo Nason. A new method for combining NLO QCD with shower Monte Carlo algorithms. *JHEP*, 11:040, 2004.

[95] Stefano Frixione and Bryan R. Webber. Matching NLO QCD computations and parton shower simulations. *JHEP*, 06:029, 2002.

[96] C. Balazs, J-W. Qiu, and C. P. Yuan. Effects of QCD resummation on distributions of leptons from the decay of electroweak vector bosons. *Phys. Lett. B*, 355:548, 1995.

[97] Stefano Catani, Daniel de Florian, Giancarlo Ferrera, and Massimiliano Grazzini. Vector boson production at hadron colliders: transverse-momentum resummation and leptonic decay. *JHEP*, 12:047, 2015.

[98] G. A. Ladinsky and C. P. Yuan. The nonperturbative regime in QCD resummation for gauge boson production at hadron colliders. *Phys. Rev. D*, 50:R4239, 1994.

[99] C. Balazs and C. P. Yuan. Soft gluon effects on lepton pairs at hadron colliders. *Phys. Rev. D*, 56:5558, 1997.

[100] F. Landry, R. Brock, Pavel M. Nadolsky, and C. P. Yuan. Tevatron Run-1 Z boson data and Collins-Soper-Sterman resummation formalism. *Phys. Rev. D*, 67:073016, 2003.

[101] Sayipjamal Dulat, Tie-Jiun Hou, Jun Gao, Marco Guzzi, Joey Huston, Pavel Nadolsky, Jon Pumplin, Carl Schmidt, Daniel Stump, and C. P. Yuan. New parton distribution functions from a global analysis of quantum chromodynamics. *Phys. Rev. D*, 93:033006, 2016.

[102] Kirill Melnikov and Frank Petriello. Electroweak gauge boson production at hadron colliders through $\mathcal{O}(\alpha_s^2)$. *Phys. Rev. D*, 74:114017, 2006.

[103] Stefano Catani, Leandro Cieri, Giancarlo Ferrera, Daniel de Florian, and Massimiliano Grazzini. Vector boson production at hadron colliders: a fully exclusive QCD calculation at NNLO. *Phys. Rev. Lett.*, 103:082001, 2009.

[104] Piotr Golonka and Zbigniew Was. PHOTOS Monte Carlo: A precision tool for QED corrections in Z and W decays. *Eur. Phys. J. C*, 45:97, 2006.

[105] Vardan Khachatryan et al. Measurements of Inclusive W and Z Cross Sections in pp Collisions at $\sqrt{s} = 7$ TeV. *JHEP*, 01:080, 2011.

[106] CMS Collaboration. Measurement of the W boson rapidity, helicity, and differential cross sections in pp collisions at $\sqrt{s} = 13$ TeV. 2020.

[107] Marc Paterno. Calculating efficiencies and their uncertainties. *FNAL/CD/CEPA/SLD*, 2004.

[108] G. Breit and E. Wigner. Capture of Slow Neutrons. *Phys. Rev.*, 49:519–531, 1936.

[109] M. Oreglia. *A Study of the Reactions* $\psi' \to \gamma\gamma\psi$. PhD thesis, SLAC, 1980.

[110] Tomasz Skwarnicki. *A study of the radiative CASCADE transitions between the Upsilon-Prime and Upsilon resonances*. PhD thesis, Cracow, INP, 1986.

[111] Vardan Khachatryan et al. Performance of Photon Reconstruction and Identification with the CMS Detector in Proton-Proton Collisions at sqrt(s) = 8 TeV. *JINST*, 10(08):P08010, 2015.

[112] A. Bodek, A. van Dyne, J. Y. Han, W. Sakumoto, and A. Strelnikov. Extracting Muon Momentum Scale Corrections for Hadron Collider Experiments. *Eur. Phys. J.*, C72:2194, 2012.